The Demographics of Protoplanetary Disks: from Lupus to Orion

Proefschrift

ter verkrijging van
de graad van Doctor aan de Universiteit Leiden,
op gezag van Rector Magnificus prof. mr. C.J.J.M. Stolker,
volgens besluit van het College voor Promoties
te verdedigen op Woensdag 11 December 2019
klokke 16:15 uur
door

Sierk Eyse van Terwisga

geboren te Rotterdam, Nederland
in 1992

Promotiecommissie

Promotores:	Prof. dr. E. F. van Dishoeck	UL
	Prof. dr. M.R. Hogerheijde	UL, UvA
Co-Promotor	Dr. N. van der Marel	University of Victoria
Overige leden:	Prof. dr. H. J. A. Röttgering	UL
	Prof. dr. S.F. Portegies Zwart	UL
	Dr. J. M. Carpenter	Joint Alma Observatory
	Prof. dr. T. Megeath	University of Toledo
	Prof. dr. M. R. Meyer	University of Michigan
	Prof. dr. A. Natta	Dublin Institute for Advanced Studies

ISBN: 978-94-028-1823-9

Front cover:
Two dust rings and the bright central region of V1094 Sco in ALMA data at 1.3 mm superimposed over the manuscript of *Tout par compas suy composé*, a canon by the French composer Baude Cordier (*fl.* early 15th century) from the Chantilly Codex (Musée Condé MS 564).

Science n'a nul annemi
Se non ceulz qui sont ignorant.
Envieuz sont, je le vous di,
Souvent sur ceulz qui sont sachant
Et vont melodie abatant
Tout voulentier per leur haut cry.

Matheus de Sancto Johanne, *Codex Chantilly, Musée Condé MS 564*

Contents

1 Introduction

> But indeed all the whole story of Comets and Planets, and the Production of the World, is founded upon such poor and trifling grounds, that I have often wonder'd how an ingenious man could spend all that pains in making such fancies hang together.
>
> Christiaan Huygens, *Cosmotheoros*, 1698

The central goal in the field of protoplanetary disk studies and planet formation is to understand how a planetary system's properties – the masses, orbits, and number of planets – are linked to the circumstellar environment in the earliest parts of a star's existence. In particular, we want to understand how the earliest formation of the solar system happened, and how rare systems like it are.

This is an ancient question, and creation myths that attempt to answer it have been told around the world and through the ages. As modern science began to take shape in Western Europe in the 1600s, it is therefore not surprising that the topic was taken up by the natural philosophers of the time.

Christiaan Huygens, who had been made a Fellow of the Royal Society in 1663 (only three years after its founding) was one of those natural philosophers, and, as the chapter quote shows, he did not mince words in his assessment of the hypotheses on the formation of the Earth and the Solar System that were in fashion at the time. In the context of the book this quote comes from, the posthumously published *Cosmotheoros*, it is a surprisingly strong statement. After all, only a few chapters earlier Huygens discussed how the rings of Saturn would appear to its inhabitants, and if an alien society would have astronomy (he concludes that it would). Certainly, many of the arguments Huygens presents are antiquated, or based on premises we now know to be incorrect. But the primary reason for his apparent disdain seems to be surprisingly modern: a lack of observational data. Huygens' universe was rather static, and its fundamental principles were not well-understood; Newton's *Principia* was published only in 1687. Even with the best telescopes of his day, astronomy was significantly limited by the human eye, both in terms of surface brightness and wavelength coverage. In that context it is perhaps not so surprising that the cautious observer Huygens would consider the origin of planets beyond the realm of scientific study.

Despite this criticism, other scientists would continue to consider the origin of the Solar System. In the 18th century, the idea that the planets had contracted from a disk orbiting

the young sun – the so-called Nebular hypothesis – was advanced by several scientists, most prominently Kant and Laplace, on the basis of the similar orbital planes and rotational axes of the solar system bodies. Laplace explicitly attempts to link his model to observations of variable stars. Apart from being remarkably prescient, this also shows an important shift in thinking of planet formation as an ongoing process, as opposed to something that happened in the distant past. However, a lack of observational support of this hypothesis meant that it remained controversial.

Ultimately, however, the modern understanding of planet formation and protoplanetary disk evolution, and of star formation in general, is very much the product of 20th- and 21st-century technological developments. Like the improved manufacture of lenses and the development of refracting telescopes in Huygens' time, CCDs and space-based observatories gave astronomers a new view of the universe starting from the mid-20th century. This led directly to a better understanding of star- and planet formation: protoplanetary disks and protostars are compact, faint, and emit a large fraction of their light at infrared wavelengths that are absorbed by the atmosphere. In more recent years, the enormous collecting power and resolution of telescopes like the Atacama Large Millimeter/sub-millimeter Array (ALMA) have continued this trend. Simultaneously, this wealth of observations has made it possible to develop and test much more sophisticated models of the complicated environments of young stars.

While Huygens' "poor and trifling" foundations for theories of star- and planet formation have these days been replaced by models based much more solidly on observations, it remains true that this is a large and complicated topic to discuss, and inherently difficult to study or model. In terms of timescales, the pre-main-sequence evolution of stars and the protoplanetary disks around them is an inconvenient process to observe: too slow to fit in a human lifetime (or the average PhD project), but very fast (by a factor of about 1000) compared to the total lifetime of a solar-mass star. By taking a demographic perspective, however, some of these difficulties can be overcome. Disks are ideally suited for this approach: they are long-lived enough that large samples exist in nearby star-forming regions. By observing distinct populations of protoplanetary disks, in different environments and at different ages, it is possible to gain insight into the long-term evolution of disks.

In this Introduction, some key aspects of the formation of stars and planets are discussed, focusing particularly on protoplanetary disks and their properties and evolution. In Section 1.1, the evolution of circumstellar material from the earliest embedded phase to a young planetary system is described, as well as the gas- and dust structure of a typical protoplanetary disk. Section 1.2 discusses the properties of several important nearby star-forming regions, focusing on the properties of their stellar populations. Results from surveys of these regions, both in near-infrared and submillimeter wavelengths, are shown in Section 1.3, while Section 1.4 deals with the increasingly strongly interrelated fields of exoplanetary and protoplanetary disk demographics.

1.1 Forming stars and planets

In this Section, the formation of stars and protoplanetary disks is briefly discussed, as well as the structure of disks. In the earliest phases of star formation, the star is deeply embedded. However, it is in this period that the initial conditions for the disk are set. Moreover, there is increasing evidence that significant evolution of the disk material can occur even at these early stages. As in the rest of this thesis, the focus here lies on low-mass stars. For massive stars, there is evidence that key parts of their formation proceed similarly. For instance, Ke-

plerian disks have been identified around massive Young Stellar Objects (YSOs) by Ginsburg et al. (2018). We also focus primarily on the case of single objects. An important to caveat to this discussion is also that the evolutionary stages we discuss here do not correspond one-to-one to the observationally defined classes based on the near- to far-IR emission of these objects, as defined in (Lada 1987; Andre et al. 1993). For instance, an edge-on Class II source may appear to be similar to a Class I YSO based on its infrared emission.

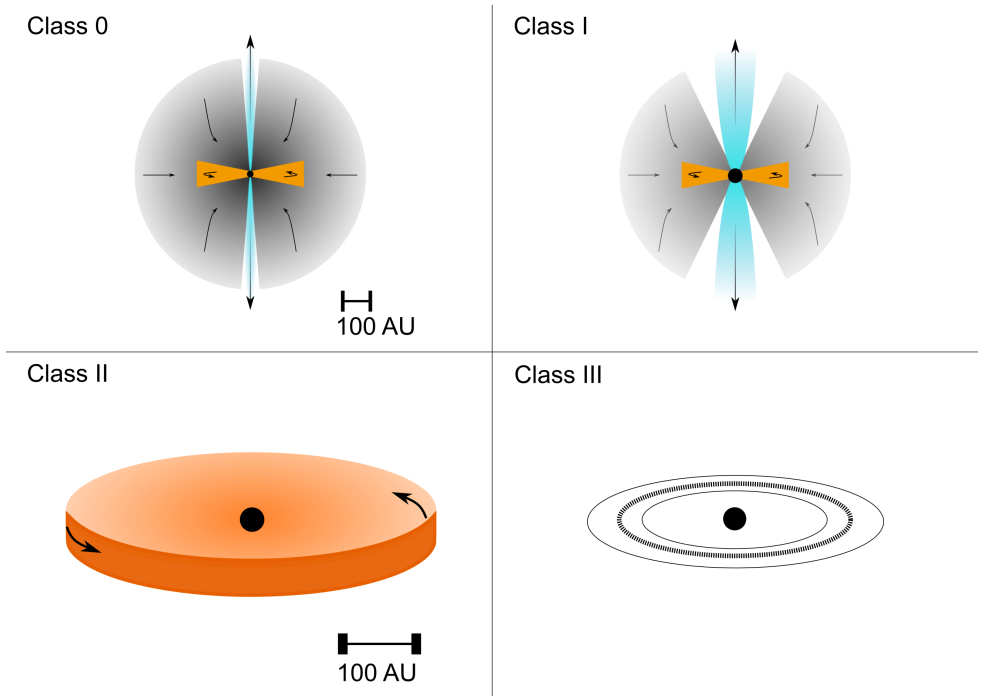

Figure 1.1: Schematic overview of the evolution of circumstellar material during the process of star- and planet formation.

1.1.1 The embedded phases of star formation

Class 0

The modern view of star formation starts from the collapse of gravitationally unstable pre-stellar cores into protostars. At the earliest stages, the protostar is therefore completely surrounded by a dense, rotating, and infalling envelope, which is massive compared to the star (Fig. 1.1, top left). These objects are still actively accreting a significant fraction of their final mass; the stellar mass is therefore very low compared to that of the envelope. Such Class 0 objects tend to be associated with outflows and have low bolometric temperatures ($T_{\rm bol} \leq 70$ K). The evolution of these deeply embedded objects is rapid, and therefore difficult to observe, with typical lifetimes of ~ 0.2 Myr (Dunham et al. 2015). Even in this deeply embedded stage, however, evidence of Keplerian accretion disks has now been found, indicating that these structures form at early ages (e.g., Tobin et al. 2012; Murillo et al. 2013; Codella

et al. 2014). There is also evidence that the largest of these disks may be gravitationally unstable (Tobin et al. 2016).

Class I to Class II

As the star gains mass, the outflow opening angle widens and the envelope is increasingly dispersed. Because of this the central star starts to become visible, although it is still surrounded by large amounts of circumstellar material, both in the disk and the envelope (Fig. 1.1, top right). As the Class I evolution proceeds, the envelope is progressively removed until only the disk remains, and we speak of a Class II YSO. Class I YSOs have longer lifetimes than Class 0 sources (~ 0.4 Myr versus ~ 0.2 Myr) (Dunham et al. 2015).

Like the Class 0 sources discussed above, the era of high-resolution ALMA imaging has now revealed unexpected features in Class I disks. Of particular importance is the finding of axisymmetric rings and gaps in the dust disks around some Class I YSOs. HL Tau is a class I disk, and shows multiple rings and gaps. Leaving aside, for the moment, the origin of these structures, their presence alone is a sign that substructures can form very early on in a disks' lifetime. Other evidence of significant evolution of the solid components of Class 0 and Class I disks comes from the VANDAM survey of protostars in Perseus, which found a significant decrease in the average continuum luminosity of disks going from Class 0 to Class I and Class II (Tychoniec et al. 2018). However, as with Class 0 sources, the short lifetimes of the embedded phases make it difficult to observe the evolution of disks in lower-mass regions, where only a handful of such objects may be found. In contrast, a Class II source – where the envelope is dispersed, and only the star and protoplanetary disk remain – is observable for a few million years, making it much more common and easily observable.

1.1.2 Protoplanetary disks

As we saw in the previous paragraphs, protoplanetary disks exist throughout the embedded phase, but are especially important during the Class II stage of pre-main sequence evolution. But what are the structures of these objects?

The idea that the infrared excess emission identified in the spectral energy distributions (SEDs) of certain protostars was due to the presence of a disk was first suggested in the late 1970s, in the seminal paper of Lynden-Bell & Pringle (1974), who posited that a viscous accretion disk would explain the observations of T Tauri stars. Thanks to the successful flight of the first IR satellites, it was discovered that flared disks reprocessing the stellar radiation (that is, not heated primarily by accretion) were most consistent with observations especially for Class II YSOs with low accretion rates (Hartmann & Kenyon 1985; Adams & Shu 1986; Adams et al. 1987; Kenyon & Hartmann 1987). The refurbished Hubble Space Telescope's first pictures of proplyds (ProtoPlanetarY Disks) in Orion, showing flared disks against the bright nebula's background, provided direct proof of this model (O'dell & Wong 1996). Although modern observations – particularly, the high-resolution view of dust and gas in disks that ALMA has given us – have now significantly complicated our understanding of disks, the original flared, viscous disk model remains a useful first-order approximation of disk structure.

Dust and gas

Disks, in general, are assumed to have a global gas-to-dust ratio of 100:1, the same as that measured in the interstellar medium (although this may not be true in all cases). However,

the distribution of gas and dust grains is not equal even with this assumption. While the gas is supported by pressure, and small dust grains are well-coupled to the gas and distributed similarly in the vertical direction, larger dust particles can settle to the disk midplane efficiently. The approximately millimeter-sized dust grains observed with ALMA are therefore typically considered to be confined to the midplane; but disks observed in scattered light are clearly flared, since those observations trace the scattering surface of smaller grains at larger scale heights. Besides settling to the midplane, midplane dust also grows, migrates inward, and evolves due to gas drag, introducing a difference in the radial extents of gas and dust particles of different sizes (Fig. 1.2).

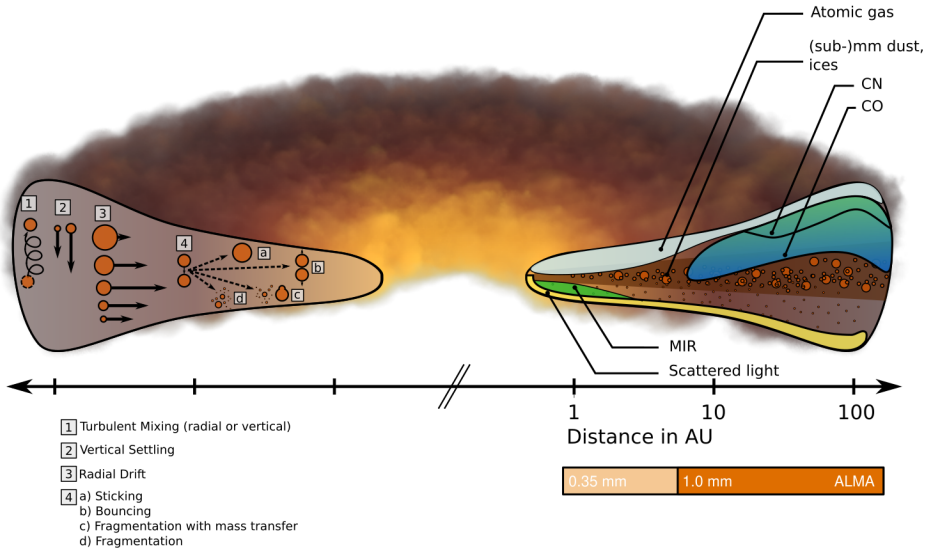

Figure 1.2: Schematic overview of the behaviour of dust *(left)* in a protoplanetary disk, and the regions probed by different tracers *(right)* relevant to this thesis. Figure adapted from Testi et al. (2014).

At the same time, the vertical temperature and density gradient in a disk leads to a rich chemical structure in the gas: in the midplane, depending on the distance from the star, various molecules can be frozen out onto the dust grains. This can affect the grains' collisional properties, especially in those areas where the temperature drops below the freezeout temperature of a gas species when moving radially outward, the so-called snow lines (e.g., Zhang et al. 2015; Okuzumi et al. 2016). Going up from the midplane, the molecular gas is increasingly warm and the reduced density of the disk leads to UV radiation impinging on the disk becoming more important to the disk chemistry, until eventually the gas becomes purely atomic at the outer surface of the disk (Fig. 1.2). This means that different molecules are tracers of different parts of the disk's three-dimensional structure. For instance, N_2H^+ is produced in areas where CO is removed but N_2 is still present (van 't Hoff et al. 2017a), while CO and its isotopologues are found in different parts of the disk which depend on the ability of the different molecules to self-shield (Miotello et al. 2014), and CN is bright in the upper parts of the disk where excited H_2 is abundant (Cazzoletti et al. 2018).

Disk substructures

While the original, smooth disk density profiles work well in many situations, it was known already in the late 1980s that some disks have smaller mid-IR excesses than average T Tauri stars (Strom et al. 1989), which was attributed to gaps in the inner disk. In recent years high-resolution observations of disks in scattered light, (sub)millimeter continuum emission, and gas lines have shown conclusively that many disks show rich structures. In scattered light, arcs and rings are seen with instruments like SPHERE and GPI (Avenhaus et al. 2018; Rapson et al. 2015). At millimeter wavelengths, many disks now show a wealth of rings and gaps (e.g., ALMA Partnership et al. 2015; Andrews et al. 2016a, 2018, Chapter 2 of this thesis). For some of these objects, there is also evidence that the gas density is decreased in the gaps (van der Marel et al. 2016a). Non-axisymmetric dust structures have now also been found, from extreme asymmetries (such as IRS 48) (van der Marel et al. 2013) to more subtle spiral structures (Huang et al. 2018).

The origin of these structures, and in particular of the axisymmetric dust rings, is currently a matter of significant debate. Any model needs to explain why these structures are seen in young, embedded objects, such as the previously mentioned HL Tau, as well as in disks like the very old ($\sim$ 10 Myr) TW Hya disk (Andrews et al. 2016a). The two main hypotheses are that the dust rings are caused by planet-disk interactions, or by the presence of snowlines of different molecules. In the latter explanation, rings occur in the region where volatile molecules start to condensate on grains for the first time, and affect their collisional properties. In other words, instead of an increase in overall grain density, the sub-mm rings are an effect of local dust opacity changes. However, this hypothesis seems to be increasingly at odds with the observed locations of these rings, since they often fail to align with the expected locations of snowlines (Long et al. 2018; van der Marel et al. 2018a, Chapter 2 of this thesis). Planet-disk interactions may lead to rings at any radius, provided a sufficiently massive planet is present. In this scenario, the planet carves out a gas gap flanked by two pressure maxima. The dust will drift towards these pressure maxima and be trapped, leading to rings and gaps. However, this implies that planet formation can happen even in the embedded phase. Alternative hypotheses for ring formation include dead zone edge-effects, and (secular) gravitational instability; but the former has difficulty in producing the number of rings seen in some sources while the latter requires very massive disks, which is difficult to achieve in Class II YSOs.

Class II to Class III

Ultimately, the disk is dissipated, typically on a timescale of millions of years if viscous evolution alone is the primary mechanism. Stars without significant contribution from disk material at infrared wavelengths, but other indications of youth, are called Class III sources (Fig. 1.1, bottom right). However, the evolution of YSOs depends on external factors as well as internal processes. An extreme example is the evolution of disks in binary systems, which seem to be consistently less luminous than those around single stars (Akeson et al. 2019). Even single stars can be affected significantly by their large-scale environment, as will be discussed in Section 1.2.2.

In some cases, some orbiting dust remains around the host stars after the protoplanetary disk's gas has dissipated, and is visible as a debris disk. The other, much longer-lived outcome of the disk's evolution is of course a possible planetary system. In recent years, the rapid growth in the number of known extrasolar planets has made it clear that our theories of disk evolution do not only need to explain the Solar System, but also the wide variety of planets

seen around other stars.

1.2 Star formation in the local galaxy

So far, we have discussed the evolution of protoplanetary disks from the perspective of an individual star. However, in practice, stars are formed near other stars, from larger clouds. The scale of this process varies dramatically across the universe. Star-forming clouds can produce anything from small groups with a few dozen members, such as the TW Hya moving group, to massive clusters like 30 Doradus, which contain hundreds of thousands of solar masses worth of stars, including hundreds of high-mass stars ($M_\star > 15 M_\odot$). In this thesis, we focus on the star-forming regions (SFRs) found in the local galaxy, out to distances of ~ 500 pc. While the most extreme high-mass star-formation regimes are not present in this region, the Orion Molecular cloud does host several O-type stars with masses over $15 M_\odot$, and there is a wide variety of low-mass SFRs within this distance, allowing us to study disks in different environments and at different ages.

In order to map the populations of YSOs, it is essential to have sensitive coverage at multiple wavelengths, in order to characterize their evolutionary state. Infrared observations are particularly important, since the distinction between Class I, II and III sources is based on their infrared spectral index. For this thesis, the excellent sensitivity of the *Spitzer* space telescope has been particularly important. The deep surveys of nearby star-forming regions by this telescope (the Gould Belt and c2d Legacy Programs; Evans et al. 2003; Harvey et al. 2008), as well as the survey of the Orion A and B molecular clouds by Megeath et al. (2012, 2016)) provide a uniquely deep look into the stellar populations of nearby SFRs at infrared wavelengths. For the survey of disk masses in NGC 2024, presented in Chapter 5, infrared observations with the UKIRT telescope were used (Meyer 1996). Apart from targeting the wavelength range where the presence of disks is most obvious, what makes these surveys important is that they are deep enough to be complete for objects with stellar masses down to $\sim 0.1\, M_\odot$. This means that we sample the peak of the Initial Mass Function (IMF) of these regions, which prevents the resulting analyses from being biased towards higher-mass objects.

1.2.1 Low-mass star-forming regions

The low-mass star forming regions in the nearby universe are not as visually spectacular as those which form many O- and B-type stars, like the Orion Nebula. Since the stellar masses and densities involved are lower, they are associated with dark clouds. These were systematically surveyed for the first time by Barnard (1927), who concluded, correctly, that these were foreground objects in the nearby Galaxy, as opposed to regions without stars (Barnard 1919). These clouds were soon found to contain T Tauri stars (Joy 1945), and when the young nature of these objects was realized, the link between star formation and dark clouds was quickly made.

A typical example of a nearby low-mass star-forming region which is particularly relevant to this thesis is Lupus (Fig. 1.3). About half the size of the Taurus-Auriga and Chamaeleon regions, it contains a population of about one hundred Class II YSOs, associated mostly with the Lupus I, II, III and IV molecular clouds. The Class II sample is dominated by Lupus III, which hosts a small but – for low-mass clouds – quite dense cluster of young stars, and the more massive HR5999 and HR6000 stars (located in the center of Figure 1.3) (Comerón

2008a). The ages of YSOs are subject to large uncertainties. However, Lupus as a whole is generally assumed to be 1–3 Myr old.

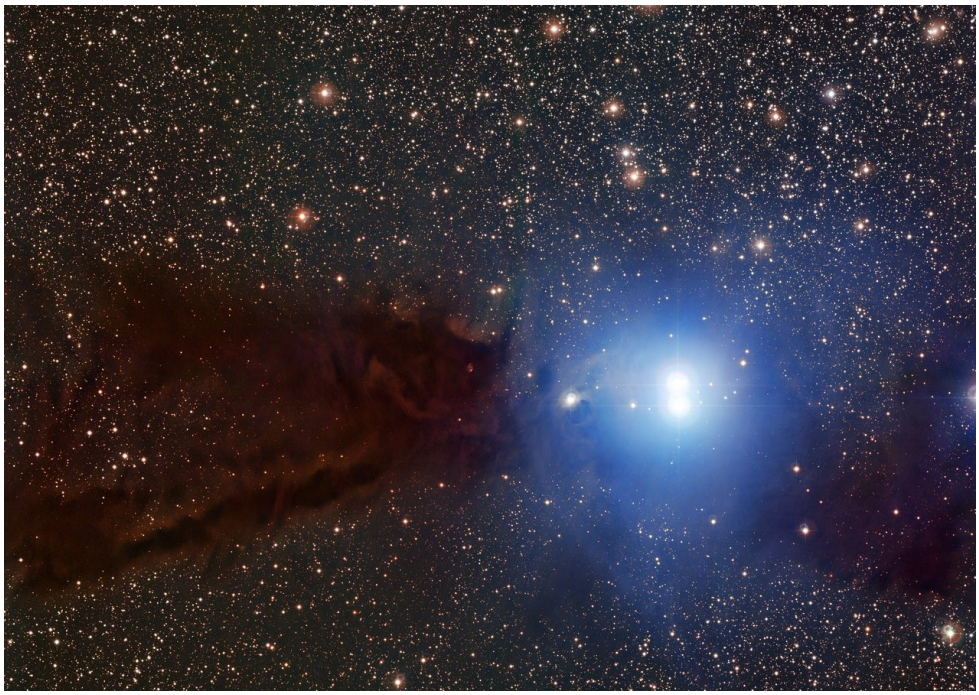

Figure 1.3: The Lupus III dark cloud at optical wavelengths, hosting a group of Class II YSOs studied in this thesis (Chapter 2). *ESO/F. Comeron, 2013*

The Lupus disk population is very well characterized at sub-millimeter wavelengths, thanks to an ALMA program in Band 6 and Band 7 that observed the known Class II population with high resolution ($\sim 0.25''$, or ~ 20 AU radius in physical distance). The observations targeted continuum wavelengths as well as several key gas lines :^{12}CO and its rarer isotopologues ^{13}CO and C^{18}O, as well as CN (Ansdell et al. 2016, 2018; van Terwisga et al. 2019c). At the same time, a large VLT/X-SHOOTER program produced consistent and accurate stellar properties (Alcalá et al. 2017). Like for other star-forming regions in the nearby galaxy, the *Gaia* satellite also provides important information on the absolute and relative distances of cloud members. In this thesis, these projects stood at the basis of Chapter 2 and Chapter 3: the completeness of the Lupus ALMA survey makes it possible to compare extraordinary individual objects to the rest of the population, while the gas line coverage sheds light on the properties of relatively abundant simple molecules.

Lupus is interesting also because it is, in many ways, rather generic. Lupus, Taurus-Auriga, and Chamaeleon show similar small groups with higher densities and a more dispersed population of Class II sources (Kenyon et al. 2008; Luhman 2008); ρ Ophiuchus and Corona Australis have simpler morphologies with only one density peak, but otherwise seem to have similar population sizes, containing 50–250 disks (Wilking et al. 2008; Cazzoletti et al. 2019). Comparing their ages (and taking into account again the substantial uncertainties involved), these regions also seem to be very similar. This leads to one of the central questions in the field of disk demographics: given the apparent large-scale similarities between these

regions, are the disks also similar?

In contrast with these young regions, the older Upper Scorpius/Centaurus OB association is also important to mention. As its name suggests, this region contains rather more massive stars than the low-mass SFRs discussed so far, although not as many as Orion (see Section 1.2.2). It is significantly older: its age is typically given at 6–10 Myr (Preibisch et al. 2002; Pecaut et al. 2012). Despite this, it has a well-characterized disk population, and has therefore become an important data point for the properties of evolved disks. Another important sample of young stars in the solar neighbourhood is the TW Hya Association. Like Upper Sco, it has an age of between 6–10 Myr (Ducourant et al. 2014; Bell et al. 2015). However, it is much smaller in terms of membership: apart from the famous TW Hya disk, it contains only a handful ($\sim$ 30) young stars, and fewer disks (Gagné et al. 2018).

1.2.2 Massive star-forming regions

Figure 1.4: The Orion Nebula along the Integral-Shaped Filament (ISF), the most massive nearby star-forming region. North is to the right in this image. *ESO/J.Emerson/VISTA/Cambridge Astronomical Survey Unit*

Compared to a region like Lupus, the Orion nebula is a far more spectacular sight: the bright glow of gas, ionized by hot young stars, contrasts with the dark molecular clouds (Fig. 1.4). Indeed, the nebula is visible to the naked eye and was already an object of interest for astronomers with access to telescopes in the 16th century, who discovered its nebulous character and identified the Trapezium stars.

In terms of its stellar population, the massive star-forming regions of Orion are in every way scaled-up from the low-mass case. Massive stars do not form on their own: the IMF

peaks at M-types and therefore several thousand low-mass YSOs are also found throughout the Orion complex. The Trapezium cluster reaches a much higher peak stellar density than any of the low-mass groups discussed so far, of 10^4 YSOs pc^{-2}, two orders of magnitude higher than the densest low-mass counterpart (Megeath et al. 2016).

The Orion molecular cloud complex extends far beyond the Nebula, and hosts multiple well-studied sites of massive star formation. The most important of these are the Trapezium cluster, located in the southern Orion A cloud. Immediately to the north of the Trapezium, a dense molecular cloud – the Integral-Shaped Filament, or ISF – also hosts a large population of low-mass stars, and star formation is also ongoing to the south of the Trapezium, along the full Orion A cloud. In Orion B, the NGC 2024 cluster is the most massive. However, other massive stars are also found throughout the complex: σ Ori is a late O-type star, and also accompanied by a large population of young stars.

The different sites of (massive) star formation in Orion do not all have the same ages. Typically, the Trapezium is assumed to be 1–3 Myr old, while NGC 2024 is very young in comparison, with an age of $\sim$ 0.5 Myr; σ Ori, in contrast, is expected to be 3–5 Myr old (Oliveira et al. 2002, 2004). However, there is evidence of age gradients in the Trapezium and NGC 2024, which complicates this view (Getman et al. 2014).

Orion's massive stars do not just lead to the formation of visually spectacular ionized nebulae: their impact on the environment also extends to the YSOs formed in these regions. The discovery of proplyds (Churchwell et al. 1987) did not just confirm the model of protoplanetary disk structure (Section 1.1.2) Many of these objects have emission from ionized species (particularly, [O III]), seem to be concentrated around the primary ionizing source in the Trapezium, θ^1 Ori C, and have tails pointing radially away from that star (O'dell & Wong 1996). These properties all point to the circumstellar material in the proplyds being ionized and removed from the envelopes and disks due to the strong ultraviolet (UV) radiation field in this environment.

The dramatic impact of external irradiation by massive stars on circumstellar material of YSOs has since then been a source of significant research interest. Since regions like Orion likely form the majority of stars in the galaxy (Lada & Lada 2003), and are likely representative of the environment in which the early solar system formed (Adams 2010), understanding the evolution of circumstellar material in these conditions is an important constraint on the formation of planetary systems. There is now a large amount of literature discussing this, both from an observational and modeling perspective (e.g., Scally & Clarke 2001; Haworth et al. 2018; Concha-Ramírez et al. 2019) The results show that external photoevaporation is a common and important process for disk mass-loss in massive SFRs. Precise solutions to photoevaporative disk structures are difficult, since they form compact photon-dominated regions wih complex extinction properties. However, the general behaviour seen from these models is that material evaporates off the disk from the outside in, since the outer material is less strongly bound. Puzzlingly, disks in the ONC seem to be more abundant than their predicted lifetimes would suggest. To explain this observation, the 'proplyd lifetime problem', ongoing star formation has been suggested as an explanation (Winter et al. 2019). Interestingly, most research into disk mass loss in massive SFRs has also shown that disk truncation by dynamic interactions is less important by far except in the densest and most massive regions (Wijnen et al. 2017).

1.3 Protoplanetary disk demography

The existence of multiple distinct populations of YSOs, in different environments and at different ages, is what enables astronomers to study them from a demographic perspective, as opposed to focusing on individual objects. Here, we will focus first on some of the key results from pre-ALMA studies that used this approach, before considering the main results from ALMA surveys of disk populations. Like in all fields of astronomy, results from different wavelength regimes provide information on different, but often complementary, processes.

1.3.1 The optical and near-infrared perspectives

Near-infrared continuum emission from protoplanetary disks is a useful tool for demographic studies. Since it traces the optically thick, warm dust in the inner regions of the disk, it is a (relatively) simple indicator of the presence of any amount of such material around a YSO. It is also a relatively accessible tracer, since the relevant wavelengths can already be targeted by Earth-based infrared telescopes in the J, H, K and L-bands; as usual, however, the *Spitzer* space telescope has allowed this type of study to be extended to longer-wavelengths Haisch et al. (e.g., 2001); Calvet et al. (e.g., 2005); Ribas et al. (e.g., 2014).

The central idea here is to observe the fraction of stars belonging to a young star-forming region with and without disks, and compare the disk fractions between different regions. This means that it is extremely important that the sample be selected uniformly and that no contamination is present. In addition, we must assume here that all disks have an NIR excess. While this is normally the case, transition disks may have sufficiently empty inner gaps that they appear to be similar to Class III sources if no longer-wavelength information is taken into account (Merín et al. 2010).

Haisch et al. (2001) showed, based on JHKL photometry, that the disk fraction across different regions is a strong function of age: young ($\sim$ 0.5 Myr) regions have disk fractions of $\sim$ 80%, but this drops to less than half in 3 Myr; this result is shown in Figure 1.5. A single characteristic lifetime of 6 Myr governs the loss of inner disks. Other work, in Orion OB1, and with *Spitzer* supports this fundamental result, but with added complexity from deeper wavelength coverage. Calvet et al. (2005) show that not just disk fractions but also disk structures as traced in NIR wavelengths change, consistent with the process of dust settling discussed previously. *Spitzer*'s excellent mid-IR performance allowed Ribas et al. (2014) to extend the idea of disk fractions to longer wavelengths. This revealed that dust emitting at $12 - 24\,\mu$m evolves more slowly ($\sim$ 6 Myr, rather than $\sim$ 3 Myr) in nearby SFRs, suggesting that colder dust in the outer regions of disks remains present for longer than the optically thick warm disk. Another important result is that the disk and stellar masses are strongly linked, with massive stars hosting fewer disks in Upper Sco, suggesting that these disks may evolve more rapidly (Carpenter et al. 2006; Ribas et al. 2015).

Apart from tracing the fraction of disks in general, disk surveys have also been used to characterize populations of peculiar objects, such as disks with inner dust cavities (Merín et al. 2010; van der Marel et al. 2016c). The fraction of such objects is particularly interesting, as they are thought to host massive planets. Accurately determining the structure of such objects, however, is difficult, and it has therefore not been possible until the advent of ALMA to compare such objects to the known giant planet population in an unbiased way.

Infrared spectral indices do, however, allow us to constrain another important set of timescales: those relevant for the evolution of Class 0 and Class I sources. By comparing the numbers of Class 0, I and II sources in different regions and assuming a single evolutionary

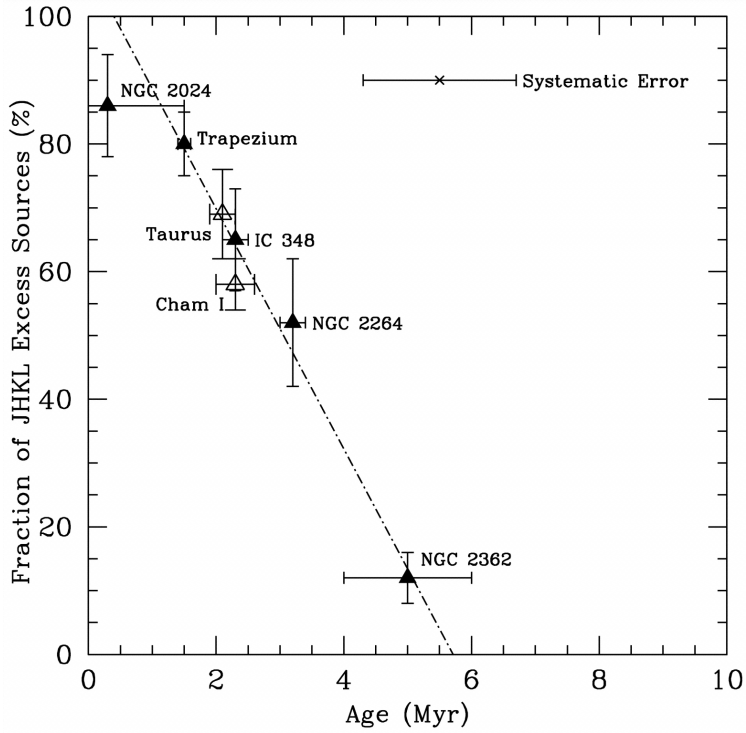

Figure 1.5: The disk fraction based on JHKL-band photometry as a function of cluster age for a range of nearby star-forming regions. Vertical error bars represent the statistical errors in the derived disk excess fraction, while horizontal error bars show the standard deviation and mean of the ages of the individual sources, assuming a single model. The systematic error in the top right shows the effect of using different models for pre-main sequence stellar evolution on region ages. Figure taken from Haisch et al. (2001)

timescale for all Class II sources, it is possible to convert the fractions of younger Classes into lifetimes (Dunham et al. 2015; Carney et al. 2016). This does, however, imply that star formation is continuous over the lifetime of a Class II disk, and implicitly averages over different regions.

So far, we have discussed tracers of dust in various parts of the disk. However, the flow of gas from the disk onto the star can also be traced, using accretion tracers like the Hα line; other lines are used as well (Hartmann et al. 2016). As with disk fractions, comparing the accretion rates of objects in different regions and with different ages can provide important constraints on how disks accrete onto their stars. There is a large body of research into this topic, which we cannot fully discuss here, and which is complicated by the fact that accretion is not a steady process, but instead variable. This is particularly problematic for Class I and younger objects, but even the case for 'normal' T Tauri-stars. However, some trends can be seen. While the accretion rate for older regions is lower (e.g., Hartmann et al. 1998; Manara et al. 2012), large accretion rates can be found in old regions, and in general there is a real but otherwise unexplained scatter along the accretion-age relation. Likewise, accretion rate and stellar mass are correlated, with higher-mass stars accreting more rapidly;

again, this relation has a quite large intrinsic scatter (e.g., Muzerolle et al. 2003; Calvet et al. 2004; Alcalá et al. 2017).

1.3.2 The submillimeter perspective

While they clearly provide important information on the evolution of disks, the disk fractions discussed above do not reflect the total mass of the disk. In the submillimeter wavelength regime, this is less of a problem. Observing the continuum and gas line emission from protoplanetary disks at these long wavelengths, however, is difficult, since these observables are faint. In addition, ideally, we would want to *resolve* the disk's gas and dust in order to study their spatial distribution, something that is difficult to infer from SEDs. This means that sub-arcsecond resolution is often needed. The combined requirements of sensitivity and resolution mean that the study of disks at (sub)millimeter wavelengths has been sensitively dependent on the development of large interferometric arrays at these wavelengths. The Sub-Millimeter Array (SMA), and in particular ALMA, have therefore been crucial tools for disk surveys in the past decade, since their sensitivity makes it possible to study the large samples needed for disk demography studies with sufficient completeness.

At the time of writing of this thesis, a large fraction of the nearby star-forming regions have been the subject of large, unbiased (with regards to stellar mass) surveys: Taurus (Andrews et al. 2013), Chamaeleon I (Pascucci et al. 2016; Long et al. 2017), Upper Sco (Barenfeld et al. 2016), ρ Ophiuchus (Cieza et al. 2019; Williams et al. 2019), σ Ori (Ansdell et al. 2017), IC 348 (Ruíz-Rodríguez et al. 2018), the Orion Nebula Cluster (ONC) (Eisner et al. 2018), Corona Australis (Cazzoletti et al. 2019), OMC-2 (this thesis; van Terwisga et al. 2019a) and NGC 2024 (this thesis; van Terwisga et al. in prep.). All of these surveys have observed the unresolved continuum flux from the disk populations they targeted; in all but the OMC-2 survey, at least some disks were resolved, with most surveys in regions at less than 250 pc reaching resolutions of ~ 30 AU in radius. In addition to this, for a few regions (Lupus, σ Ori, Upper Sco, Chamaeleon I, the Trapezium, and Corona Australis) at least one CO isotopologue line was included in the survey settings, giving access to the molecular gas component of disks.

In addition to these Class II disk populations, there is now also an increasing number of well-studied Class 0 and Class I disks (in Perseus and Orion; Tychoniec et al. 2018, Tobin et al. subm.). For debris disks, the sample is less complete, but they were included in the Upper Sco survey by Barenfeld et al. (2016), and Panić et al. (2013) presented a sample of nearby debris disks.

Dust masses

One key result from these surveys is shown in Figure 1.6, which shows the disk luminosity distributions in several different regions, estimated using a Kaplan-Meier estimator. If we assume that all disks have the same effective midplane temperature and dust emissivity, and that all disks are optically thin, the disk flux can be converted to the total mass of millimeter-size dust grains:

$$M_{\text{dust}} = \frac{d^2 F_{\nu,\,\text{dust}}}{\kappa_\nu B_\nu(T_{\text{eff}})}. \tag{1.1}$$

The most commonly used assumptions on the values of the parameters in Eq. 1.1 are that $T_{\text{eff}} = 20\,\text{K}$ (Andrews & Williams 2005), $\kappa_\nu = \kappa_0\,(\nu/\nu_0)^\beta$ with $\beta = 1$ and $\kappa_{1000\,\text{GHz}} = 10\,\text{cm}^2\,\text{g}^{-1}$ (Beckwith et al. 1990).

Leaving aside, for the moment, the validity of these assumptions, and just looking at the luminosity of circumstellar material, it becomes immediately obvious that the picture is

much more complicated than for disk fractions. However, some general observations can be made: disk luminosities in Lupus, Chamaeleon I, OMC-2, and Taurus appear to be very similar, while these regions are also known to have similar ages. The disk flux distribution in the older Upper Sco region, in contrast, shows much lower luminosities, suggesting a similar evolution to that of disk fractions takes place here. Compared to younger regions, however, Tychoniec et al. (2018) show that the difference between disk luminosities in Class 0 and I and Class II YSOs is large enough that significant changes must occur in the early evolution of the disk, and that the simple, single-timescale model for disk fractions may not apply. Another important result from disk surveys with ALMA is that stellar mass and disk continuum mass (or luminosity) are correlated in these regions, but that the steepness of this correlation changes by region and with age (Ansdell et al. 2017; Pascucci et al. 2016).

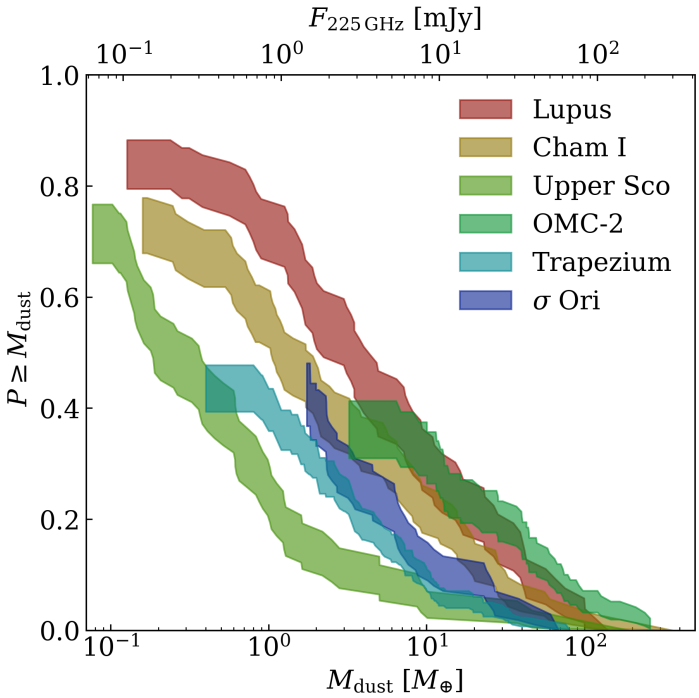

Figure 1.6: Disk flux and mass distributions determined with the Kaplan-Meier estimator for 6 nearby star-forming regions: Lupus (Ansdell et al. 2016, 2018), Chamaeleon I (Pascucci et al. 2016), Upper Sco (Barenfeld et al. 2016), OMC-2 (van Terwisga et al. 2019a), the Trapezium (Eisner et al. 2018), and σ Ori (Ansdell et al. 2017). Disk fluxes have been normalized to 200 pc. For the disk masses, optically thin emission is assumed.

The Trapezium, in contrast, a young stellar population hosts disks much less luminous than those in Lupus or Chamaeleon. In this region, however, we see strong evidence of external photoevaporation, which is likely to affect the disk masses. A similar effect has also been posited in σ Ori; both regions are in the vicinity of O stars.

The similar continuum luminosity distributions of young disk populations in distinct regions without external photoevaporation might suggest that, as we implicitly assumed

in Fig. 1.5, disk evolution proceeds similarly everywhere. However, there are some uncertainties in this, mostly driven by the small number of distinct populations that have been sampled. As Cazzoletti et al. (2019) show, the Corona Australis region appears to have 'old', low-mass disks but a young stellar population – a puzzling result in this context. Surveying more populations is a straightforward solution to this problem.

Another important consideration here is to what extent disk continuum fluxes really trace the disk solids. Even those populations with high average disk masses do not contain large amounts of millimeter-sized dust at 1–3 Myr. Thus, massive planet formation should either be relatively rare, or a significant amount of mass is not observed. The latter is possible if sufficiently large bodies form early on: we would not see protoplanets at submillimeter wavelengths easily with these sensitivities. Alternatively, the assumption that the disk is optically thin may not be true. This is now a topic of active debate: from disk surveys, a clear correlation in disk luminosity and radius is seen (Tripathi et al. 2017), which might be caused by optically thick rings. The DSHARP project did find abundant narrow rings in its sample of massive disks (Andrews et al. 2018), but with opacities $\tau < 1$; the V1094 Sco disk, studied in this thesis, shows indications of similar behaviour. This has been suggested to be a natural cause of ongoing planetesimal formation (Stammler et al. 2019), or alternatively the effect of self-scattering at millimeter wavelengths (Zhu et al. 2019) or the effect of radial drift setting grain sizes (Rosotti et al. 2019), but is still a matter of very active debate.

Gas masses

Apart from dust, submillimeter observations also give a window on an elusive, but important part of the disk: the molecular gas that makes up the majority of a disk's mass, which is typically assumed to be one hundred times the dust mass. However, there are some significant difficulties in both observing and interpreting the observations from gas. First, gas lines are faint, even for relatively abundant molecules like ^{12}CO, leading to low detection rates. This is especially unfortunate from the perspective of a demographic approach of disk evolution, which depends on large sample sizes and sampling multiple populations. Second, the bright lines quickly become optically thick – this is the case for ^{12}CO, and even the less abundant isotopologue ^{13}CO, especially in massive disks. Lastly, the interpretation of any molecular line observation depends sensitively on our understanding of the disk structure and the chemical network that underlies it. However, on this front, important advances have been made in recent years.

For surveys, large grids of disk models to interpret the observations are particularly important. Such grids have now been made for CO, both from relatively simple parametrization (Williams & Best 2014), and from much more sophisticated physical-chemical modelling codes. In particular, Miotello et al. (2016) used a grid that included isotope-selective photodissociation for CO and its isotopologues, as well as freeze-out, created with the DALI code (Bruderer et al. 2012; Bruderer 2013). Since disk mass is the most important parameter for setting the CO flux in these models, this has made it possible to calculate CO-based disk masses for large samples of disks in Lupus and Taurus (Ansdell et al. 2016; Miotello et al. 2017; Long et al. 2017).

The CO-(isotopologue)-based gas masses, however, show unexpected behaviour in both Lupus and Taurus. Compared to the usual assumption that the bulk gas-to-dust ratio in protoplanetary disks is ~ 100, the average gas-to-dust ratio in both regions is significantly lower, when inferred using these models (Ansdell et al. 2016; Miotello et al. 2017; Long et al. 2017). Together with observations of individual disks where CO isotopologues do not seem to be good tracers of the total gas mass (e.g., Favre et al. 2013; Kama et al. 2016a; Bergin et al.

2016), this has been interpreted as a sign that the chemical evolution of disks is more complex than previously expected. In the average disk, a large fraction of volatile CO is removed.

For CN, which is more sensitive to a combination of incident UV flux and surface area, a DALI-based grid is now also available (Cazzoletti et al. 2018); these models are used in this thesis (Chapter 2; van Terwisga et al. 2019c) to compare to observations of this molecule in Lupus. In the future, homogeneous, deep observations of gas lines in disks in different SFRs will hopefully provide more information on the structure and the chemical evolution of this and other species.

Disk radii

The ability of an instrument like ALMA to not just detect faint gas and dust emission but also to resolve it means that we can also consider the properties of disk radii in different populations. However, this should be done carefully: observations with different convolving beams and different sensitivities can lead to different disk radii. Additionally, the optical depths of gas and dust differ, and dust may migrate radially inward (Trapman et al. 2019). However, some general trends can be seen: large dust disks ($R_{\rm dust} > 100$ AU) are often transition disks in Lupus (van der Marel et al. 2018a); similar behaviour is seen in other regions. In the Trapezium cluster, dust disk radii are particularly compact on average; this is likely due to external photoevaporation, which removes material from the outside in (Eisner et al. 2018). In general, even in the low-mass star-forming regions, compact dust disks seem to be present, and their counterpart gas disks appear to be compact as well (this thesis, Chapter 3; van Terwisga et al. 2019c).

1.4 From disk populations to planet populations

So far, the demographics of one of the possible outcomes of the evolution of circumstellar material, the formation of one or more planets, has not been discussed in depth. To do so would require more space than is necessary here, but given the rapid growth in the numbers of extrasolar planets and planetary systems, and the increased sensitivity with which these objects are now observed, increasingly direct links can be made between the observed population of disks and planets.

One of the reasons that such comparisons are often still quite tentative is that the two approaches are sensitive to different environments: ALMA, even with its extraordinary sensitivity, is only beginning to probe AU-scale features in the nearest disks (Andrews et al. 2016a) and most surveys have effective resolutions of more than 20 AU in radius. At the same time it is relatively easier to find a massive, close-in (< 1 AU) planet with most current planet-searching techniques. The wealth of rings and other substructures that are now being found in the most massive disks by high-resolution ALMA imagining campaigns provide another way to make the link between planets and disks more explicit. As Zhang et al. (2018) show, the overlap in mass and semimajor axis-space is still small.

However, it is possible to compare bulk disk dust masses to the total mass in solids in a protoplanetary disk. This was done by Manara et al. (2018), who find that disks are significantly less massive than the typical planetary system. Apart from the previously discussed ongoing debate on how accurate the mass estimates from millimeter continuum observations are, several explanations for this puzzling result are possible. The authors suggest that disks may continue to accrete material from the larger-scale cloud, which would replenish the material lost to planetesimal formation. Alternatively, a common suggestion is that planet

formation is already complete by the time the YSO reaches Class II. This interpretation is also consistent with the observations of rings in the young HL Tau system which may be carved by planets (ALMA Partnership et al. 2015). Detections of planets inside protoplanetary disks are still rare at the moment, but likely to increase, and should make it easier to answer this question.

1.5 This thesis

The work presented in this thesis is based on ALMA surveys of protoplanetary disks in three star-forming regions: Lupus, OMC-2, and NGC 2024. The motivation for this thesis is to study the evolution of protoplanetary disks from the population level, and each of these regions offer new information from this perspective. The first two chapters focus on the Lupus clouds: a typical low-mass star-forming region. It has been the subject of a deep, uniform, and complete survey in two ALMA bands, targeting both bright gas lines (from CO, its isotopologues, and CN), as well as the continuum emission from millimeter-sized grains. This allows us to answer two important questions on disk evolution: how common are > 200 AU-sized disks with continuum substructure, and how are these substructures formed? Do the compact disks observed in the continuum observations also correspond to compact gas disks?

The chapters focusing on disks in Orion deal with the impact of the large-scale environment, and in particular, of massive stars, on disk evolution. OMC-2 provides a view of a population of disks that are formed in a massive cloud, but are isolated from the radiation of massive stars by distance and extincting material. They are particularly interesting for linking disks that do form near these massive stars to those in low-mass YSOs. NGC 2024 also hosts several massive stars, and is the youngest region surveyed so far. It is a complex environment, where the presence of multiple populations of young stars has been suggested. ALMA provides a new view of the young stellar population in this region, allowing us to independently test the complexity of this environment.

- Chapter 2 describes observations of V1094 Sco, an extended, multi-ringed disk discovered serendipitously in ALMA Lupus disk survey and places this object in the wider context of the Lupus disk population. Due to the low temperature of the disk midplane, snow lines can be excluded as the drivers behind ring and gap formation in this disk. Disks the size of V1094 Sco, with continuum emission out to 300 AU, are rare: only $2.1 \pm 1.5\%$ of Lupus disks show continuum emission beyond 200 AU.

- In Chapter 3, we characterize the CN emission from 94 Class-II disks in the Lupus star-forming region, compare it to observations in other regions, and interpret our observations with a grid of models. The cyanide radical CN is abundant in protoplanetary disks, with line fluxes often comparable to those of ^{13}CO. However, a large fraction of Lupus disks are faint in CN. Only disks with exponential gas surface density cutoffs $R_c \leq 15$ AU can reconcile these observations with models, providing the first observational evidence of a compact gas disk population in Lupus. CN rings observed in two resolved sources can be replicated by disk models without need for dust density substructures.

- In Chapter 4, we present observations of a sample of disks in the Orion Molecular Cloud-2 (OMC-2) region, and compare their dust masses to both externally photoevaporated disks in the Trapezium cluster and to disks in nearby, low-mass star-forming

regions. This allows us to test whether initial disk properties are the same in high- and low-mass SFRs, and enables a direct measurement of the effect of external photoevaporation on disks. The disk mass distribution in OMC-2 is statistically indistinguishable from that in nearby, low-mass SFRs like Lupus and Taurus, and we conclude that age is the main factor that determines these disks' evolution. The difference between the OMC-2 and Trapezium cluster samples is consistent with mass loss driven by far-ultraviolet radiation near the Trapezium. Taken together, these results imply that in isolation disk formation and evolution proceed similarly, regardless of cloud mass.

- Chapter 5 discusses the NGC 2024 star-forming region: the youngest and second most massive star-forming region in the Orion clouds, with an age of just 0.5 Myr. This environment provides a unique view of a population of 179 disks that are close to the ionizing source(s), but have not been exposed to it for a long time relative to the Trapezium disks. We find independent evidence for two distinct populations: disks along the dense molecular ridge are young ($0.2 - 0.5$ Myr) and partly shielded from the FUV radiation of IRS 2b; their masses are similar to isolated $1 - 3$ Myr old SFRs. The western population is older and at lower extinctions; the disk mass distribution in this region resembles that of the Trapezium cluster, suggesting it has been impacted by external photoevaporation.

From the perspective of disk demographics, some of the future steps are clear. The still relatively small number of regions in which submillimeter disk masses have been measured, and the diversity of such environments, mean that more populations must be observed. This is also true for gas observations, and particularly for species other than CO and its isotopologues, which can provide valuable insight in what the chemistry of a 'typical disk' looks like, beyond our current focus on the most massive few percent of such objects. In addition, properties of the stars themselves will remain an important ingredient in our characterization and intercomparison of protoplanetary disk populations.

Between the ongoing wealth of results from ALMA, the continued development of our understanding of planetary systems and their diverse natures, and in the near future, the launch of the James Webb Space Telescope, the grounds on which our understanding of comets and planets and the production of the world will become firmer still. Although there are many open questions still, they are now, at least, firmly in "the reach of human Knowledge [and] Conjecture".

2

V1094 Sco: A rare giant multi-ringed disk around a T Tauri star

S.E. van Terwisga, E.F. van Dishoeck, M. Ansdell, N. van der Marel, L. Testi, J.P. Williams, S. Facchini, M. Tazzari, M.R. Hogerheijde, L. Trapman, C.F. Manara, A. Miotello, L.T. Maud, and D. Harsono.
2018, A&A, 616, 88

Abstract

A wide variety of ring-like dust structures have been detected in protoplanetary disks, but their origin and frequency are still unclear.

Aims: We aim to characterize the structure of an extended, multi-ringed disk discovered serendipitously in the Atacama Large Millimeter/submillimeter Array (ALMA) Lupus disk survey and put it in the context of the Lupus disk population.

Methods: ALMA observations in Band 6 at 234 GHz and Band 7 at 328 GHz at 0.3″ resolution toward the K6 star V1094 Sco in Lupus III are presented, and its disk structure analyzed. The spectral index $\alpha_{\rm mm}$ is determined in the inner 150 AU of the disk.

Results: The ALMA continuum data show a very extended disk with two gap-ring pairs. The gaps are located at 100 AU and 170 AU, the bright rings at 130 AU and 220 AU. Continuum emission is detected out to a 300 AU distance, similar to IM Lup but a factor of five larger than typically found for Lupus disks at this sensitivity and resolution. The bright central region of the disk (within 35 AU) is possibly optically thick at 1 mm wavelengths, and has a brightness temperature of only 13 K. The spectral index increases between the inner disk and the first ring at the location of the first gap.

Conclusions: Due to the low temperature of the disk midplane, snow lines can be excluded as the drivers behind the ring and gap formation in this disk. Disks the size of V1094 Sco are rare, and only 2.1 ± 1.5% of disks in Lupus show continuum emission beyond 200 AU. Possible connections between the large primordial disk population, transition disks, and exoplanets are discussed.

2.1 Introduction

One of the key discoveries of the Atacama Large Millimeter/submillimeter Array (ALMA) has been the unexpectedly wide variety of structures seen in protoplanetary disks, ranging from (asymmetric) dust cavities to multiple rings at a range of radii. These multiple rings have been found in disks around both Herbig Ae/Be and T Tauri stars (Isella et al. 2016; Fedele et al. 2017a; Walsh et al. 2016; van der Plas et al. 2017; Walsh et al. 2014; ALMA Partnership et al. 2015; Andrews et al. 2016a; Loomis et al. 2017; Cieza et al. 2017; Dipierro et al. 2018; Fedele et al. 2018). Of these T Tauri stars, HL Tau, Elias 2-24, and AS 209 are very young objects (< 1 Myr), while the massive TW Hya disk is unexpectedly old (up to 10 Myr). The bulk of the disks imaged in continuum surveys of nearby star-forming regions such as Lupus do not seem to show substructures at 0.2 − 0.3″ resolution, apart from transition disks with large inner dust cavities (> 20 AU) (Ansdell et al. 2016; Tazzari et al. 2017; van der Marel et al. 2018a; Ansdell et al. 2018).

The existence of multi-ringed disks raises important questions on the evolution of disks, and therefore on planet formation, since dust particles trapped in a ring may grow efficiently without being accreted onto the star (e.g., Pinilla et al. 2012). Thus, rings can provide the material necessary for possible future planet formation. So far, several mechanisms have been proposed in the literature to generate ring-like continuum structures: (secular) gravitational instabilities, the effect of snow lines of various molecules, dead zones and, most tantalizingly, the presence of already-formed planets in the intervening gaps (e.g., Takahashi & Inutsuka 2014; Zhang et al. 2015; Okuzumi et al. 2016; Flock et al. 2015; Papaloizou & Lin 1984). Our understanding of the physics behind these multi-ringed disks is limited by the small number of known examples ($N = 5$ around T Tauri stars), as well as the difficulty of placing them in the context of a well-studied, similar population. Moreover, it is still not clear how common it is for disks to show multiple continuum rings, whether they correlate with stellar or disk parameters, or when in their evolution features like these are most likely to be present.

Another, less obvious structure found in many protoplanetary disks is an intensity profile with a bright central region surrounded by a fainter, extended outer region, resembling a “fried egg”. This structure can be seen both in multi-ringed disks, such as AS 209 and HD 163296 (Isella et al. 2016; Fedele et al. 2018), and in full disks where no rings have been identified, such as V883 Ori (Cieza et al. 2016). In the well-studied case of V883 Ori, the origin of the morphology is due to a steep (spatially unresolved) increase in optical depth at the location of the knee in the intensity profile. This increase may be linked to the presence of a water snow line, inside of which the originally large icy grains fragment into many smaller bare silicate grains. These smaller particles have smaller drift velocities causing a "traffic jam" and thus a dust pile-up in the inner disk increasing the optical depth (Birnstiel et al. 2010; Pinilla et al. 2015; Banzatti et al. 2015; Cieza et al. 2016). More generally, this type of intensity profile must trace the underlying grain properties (number density, composition and size, or both).

In this paper, we present ALMA Band 6 and Band 7 observations of V1094 Sco, a newly-identified giant multi-ringed disk in Lupus. The star V1094 is a K6 star with a luminosity of 1.7 (1.95) $L_\odot$ and an accretion rate of $\log(\dot{M}_{\rm acc}/(M_\odot {\rm yr}^{-1})) = -8.12$ (−7.7) (Alcalá et al. 2017). Throughout this article, we take a 150 pc distance to the source, consistent with the latest *Gaia* distance estimate of 153 ± 1 pc (Gaia Collaboration et al. 2018; Bailer-Jones et al. 2018); the values between brackets correspond to the published values assuming a pre-*Gaia* 200 pc source distance.

The V1094 disk had previously been recognized as an enigmatic object, in particular

by Tsukagoshi et al. (2011), who inferred from spectral energy distribution (SED) modeling that it was a cold and massive disk. Photometry from the *Herschel Space Observatory* shows a large far-infrared excess, with an SED classification inconsistent with that of a transition disk (Bustamante et al. 2015). Previous direct imaging searches for companions, either stellar or of planetary mass, have not found any down to $\sim 10\,M_J$ beyond 75 AU (Joergens et al. 2001; Uyama et al. 2017).

Several key aspects of this disk make it an especially valuable addition to the so-far small sample of multi-ringed disks around T Tauri stars: first, the population of Class II young stellar objects in the Lupus clouds is exceptionally well-studied, with a 100% coverage in ALMA Band 6 and 7 continuum at $0.3''$ resolution and 0.3 mJy beam^{-1} sensitivity (Ansdell et al. 2016, 2018). Eighty percent of these sources, including all the objects discussed here, also have Very Large Telescope X-Shooter spectroscopy data available resulting in accurate stellar types and accretion properties (Alcalá et al. 2014, 2017). This enables us to compare the disk and its host star to a large, homogenous sample, and calculate the occurrence rate of this type of object at the age of the Lupus cloud. Moreover, at ~ 3 Myr, the age of this disk places it in the middle between the young (< 1 Myr) objects, such as Elias 2-24 and HL Tau, and the 10 Myr-old TW Hya disk (Wichmann et al. 1997; Sokal et al. 2018).

In Sect. 2, the ALMA observational details are discussed, whereas continuum images showing a bright central millimeter emission core with two outer gaps and rings are presented and analyzed in Sect. 3. The availability of data at two frequencies allows the spectral index as function of radius to be determined. The V1094 Sco disk is compared with other similar disk structures in Sect. 4.1, and put in the context of the full Lupus disk sample in Sect. 4.2, demonstrating that such large disks are rare.

2.2 Observations and data reduction

The data presented here are part of the ALMA Lupus completion survey (ALMA proposal 2016.1.01239.S, P.I.: S.E. van Terwisga), which aimed to provide data on the sources not previously included in the ALMA survey of Lupus protoplanetary disks (Ansdell et al. 2016, 2018) and for which no data at similar spectral and resolution settings were available at the time. The sources included are EX Lup, GQ Lup, RX J1556.1-3655, Sz 102, Sz 76, Sz 77, and V1094 Sco.

Our observations cover Band 6 and Band 7 continuum, and the ^{12}CO $2-1$, ^{13}CO $3-2$ and $2-1$, and C^{18}O $3-2$ and $2-1$ lines, as well as CN $3-2$. The Band 6 observations were performed on 7 July 2017, using 44 antennae and $2600-16700$ m baselines, and a PWV of around 0.64 mm. The sample was observed in Band 7 on 21 May 2017, using 41 antennae and baselines between 1100 m and 15100 m at PWV columns of ~ 0.7 mm. On-source integration times were 3 and 4.5 min in Band 6 and 7, respectively.

The Band 6 data were flux-calibrated using J1427-4206, and had J1610-3958 as phase- and J1517-2422 as bandpass calibrators. The Band 7 data used J1517-2422 as flux- and bandpass calibrator and J1607-3331 and J1610-3958 as phase calibrator. While no additional flux calibration on solar-system objects was done, the Band 6 data were observed on the same day as their flux calibrator, and therefore have a small absolute flux error ($\sim 10\%$) typical of ALMA. However, the Band 7 flux calibrator was both highly variable (by a factor of 1.5 in the month following the observations) and not observed close to the date on which our data were obtained. As such, its flux – and therefore the flux calibration of all Band 7 data – is very uncertain, complicating the calculation of spectral indices and disk masses.

Fortunately, the Band 7 data in this proposal also cover GQ Lup, which has previously

been observed in that band at a high signal-to-noise ratio (S/N) and with excellent flux calibration (on Titan and Ceres) by MacGregor et al. (2017). In addition to their accurate fluxes (a less than 10% systematic uncertainty is quoted), these authors do not find any evidence for variability of this source at millimeter-wavelengths, retrieving fluxes consistent with previous studies in the 1997 − 2015 period (Nuernberger et al. 1997; Dai et al. 2010). Because our observations covered GQ Lup and V1094 Sco on the same day, it is safe to compare these data with the MacGregor et al. (2017) results to re-calibrate the Band 7 fluxes. This gives a flux ratio of $F_{\text{MacGregor et al.}}/F_{\text{this work}} = 1.3 \pm 0.009$, which we will implicitly apply to the Band 7 data throughout this paper.

Phase-only self-calibration was used to maximize the S/N of the observations in both bands. The Band 6 data allowed self-calibration down to the integration interval (6 s), whereas for Band 7 we found useable solutions down to a 15 s interval. Imaging the continuum data using the CASA `tclean` task with Briggs weighting with a robust parameter of 0.5, the beam shapes become $0.25'' \times 0.22''$ and $0.19'' \times 0.18''$ in Band 6 and Band 7 with rms noise values of 0.11 and 0.3 mJy beam^{-1} , respectively for V1094 Sco.

The discussion in this article will focus on the high-S/N continuum observations. Fluxes for the CO (isotopologue) lines can be found in Ansdell et al. (2018), and CN is discussed in Van Terwisga et al. (in prep.). The gas emission covers a (very) extended region, so that it is partly resolved-out. Also, the S/N of the line data is low, with just a few minutes of integration time, so they are not useful for a spatially resolved analysis.

2.3 Results and analysis

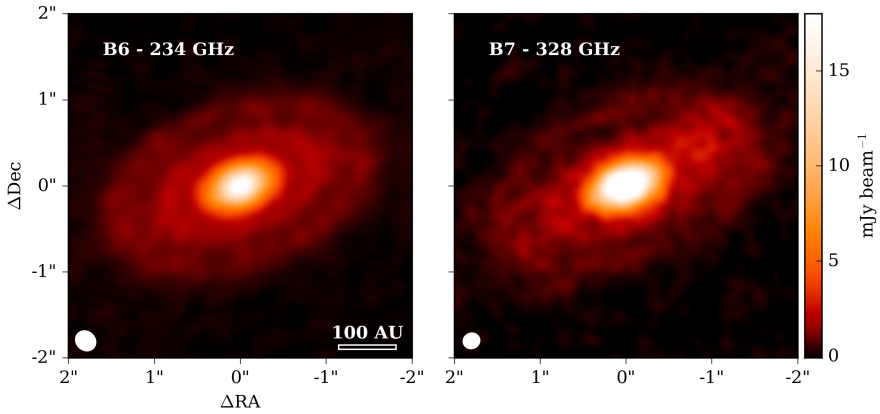

Figure 2.1: Continuum emission of the V1094 Sco disk in ALMA Band 6 (left panel) and Band 7 (right panel). Peak fluxes are 19.5 mJy beam^{-1} (Band 6) and 28.6 mJy beam^{-1} (Band 7) within the central beam. Beam sizes are indicated in the bottom right; the physical distance scale assumes a 150 pc distance towards the source.

Figure 2.1 presents the Band 6 and Band 7 continuum images resulting from the data reduction procedure described above. The continuum rings and bright central core are immediately obvious, especially in the Band 6 image. Also evident is the large radial extent of

the source, with continuum emission detected up to 300 AU when placed at 150 pc. This is comparable to the radius of the well-known massive IM Lup disk (Cleeves et al. 2016), one of the largest and most massive disks in Lupus. The full integrated flux (inside of a 2.16″ radius aperture, beyond which the image is entirely dominated by noise) in Band 6 is 180 ± 14 mJy, while in Band 7 it is 390±19 mJy. The fluxes and errors here were derived using aperture photometry with a curve-of-growth method to set the aperture radius, identical to the method used in Ansdell et al. (2016, 2018).

The key features are clearly the same in both images: the disk has a large radial extent, with two bright rings superimposed over a fainter, extended continuum, and a bright and at this resolution apparently featureless central region. Like other multi-ringed disks, V1094 Sco does not show significant azimuthal asymmetries at this sensitivity and resolution. Assuming the disk is indeed purely radially symmetric, fitting a two-dimensional Gaussian in the image plane with the `imfit` task in CASA led to a beam-deconvolved PA= 109 ± 1.9° and $i = 53 \pm 1.3°$, and a J2000 phase center of 16h08m36.17s, -39°23m02.87s.

Comparing the Band 6 and Band 7 data in the image plane, however, is not entirely straightforward. Due to the lower S/N and worse weather conditions affecting the Band 7 data, the phase-calibration is only partially successful. As a result, the Band 7 phase noise is higher than that of the Band 6 observations. Also, the u,v-plane coverage of the Band 7 data is different. These conditions particularly affect the emission in the north-east and south-west of the disk at $\sim 1''$ from the disk center, and make the presence of the rings less obvious. The Band 6 data, on the other hand, suffer from a low-amplitude north-south ripple, since the longest baselines are only sampled in a single direction. However, its impact is relatively minimal. Therefore we choose the Band 6 data as the basis for the subsequent analysis.

2.3.1 Disk structure: Core, gaps, and rings

In order to compare the continuum structure of V1094 Sco with that of other, similar disks around both earlier and similar spectral-type stars, we model the intensity profile using an approach similar to that of Zhang et al. (2016): the intensity at radius R is considered as the sum of Gaussian contributions, multiplied by a cosine. This model is then Fourier-transformed and fit to the derotated, deprojected data in the u,v-plane, after binning the data to 10 kλ bins. The advantage of this method is that it uses a minimal number of parameters and can easily formally confirm the presence of structures, and precise locations of the brightness maxima and minima. Moreover, it does not rely on a model-dependent temperature profile or assumptions about the dust properties. The u,v-plane data show four local maxima between 0 and 700 kλ; therefore, we use up to $n = 4$ terms, for a total of 13 free parameters:

$$I(\theta) = \frac{1}{\sqrt{2\pi}\sigma_0} \exp\left(-\frac{\theta^2}{2\sigma_0^2}\right) + \sum_1^3 \cos(2\pi\theta\rho_j) \times \frac{a_j}{\sqrt{2\pi}\sigma_j} \exp\left(-\frac{\theta^2}{2\sigma_j^2}\right). \tag{2.1}$$

In this model, θ is the angular separation from the source center, σ_i the width of the ith component, a_i its intensity, and ρ_i the spatial frequency of the cosinusoidal perturbation. No baselines longer than 700 kλ are included in the fit, since the data are noise-dominated beyond that point. A Monte Carlo Markov Chain (MCMC) fitting procedure was used to

infer the best fit parameters, using the `pymc` package. Since the model is degenerate if the ranges for ρ_i overlap, their allowed values were restricted based on the location of the peaks in the u,v-plane, but always at least 100 kλ wide in order to sample the full width of each peak. We confirmed that the behavior of the Markov chain was proper, by ensuring the walkers were burnt-in and inspecting their sampling of the parameter space, and checking that the posterior distributions for the parameters showed a single clear maximum. Since we start our model with values for the disk inclination, position angle, and coordinates, derived with the `imfit` task, the resulting best-fit parameters are conditional on these priors. We confirmed their impact on the resulting fit was minimal by re-running the fitting code with different initial choices of inclination, position angle, and source center within their error bars.

Figure 2.2 presents the resulting model of the intensity distribution for the Band 6 data, with the best-fit values in Table 2.1 and inferred positions for the gaps and rings in Table 2.2. The best-fit ring and gap positions are also shown on top of the Band 6 data in Figure 2.3. The results show that our four-component model is a good description of the data, fitting all local maxima within this baseline range. The parameter values also indicate that our description of the disk as a bright core with an extended outer region featuring two rings is accurate: the "core" of the disk is contained within the $i = 1$ component, having a characteristic radius of 35 ± 2 AU.

In the best-fit model, the two bright rings and two gaps are also present in the image plane, arising from the combination of the various components in Equation 2.1. They are identified by taking local maxima and minima of $I(\theta)$. Taking into account the errors on the fit parameters, the locations of the bright rings become 130 ± 9 AU and 220 ± 16 AU, while the gaps are found at 100 ± 6 AU and 170 ± 13 AU. This closely matches the intensity profile of the disk after deprojecting and derotating in the image plane (see also Sect. 2.4.1). The best-fit model gives an intensity ratio of 2.3 for the first ring-gap combination and 1.4 for the second ring and gap. It is difficult to constrain the width of the gaps and rings from this fit, as there may be a structure at smaller scales that is not probed, due to insufficient S/N at large baselines and the resolution limit.

Table 2.1: Parameter values and inferred errors from the MCMC fit to the Band 6 u, v-data.

	$i = 0$	$i = 1$	$i = 2$	$i = 3$	$i = 4$
a_i [Jy]	-	1.8 ± 0.3	0.64 ± 0.096	0.46 ± 0.05	0.52 ± 0.18
σ_i [AU]	161 ± 8.3	35 ± 1.9	57 ± 5.0	130 ± 37	120 ± 29
ρ_i [kλ]	-	20.7 ± 0.1	446 ± 12	146 ± 15	255 ± 9
λ/ρ_i [AU]	-	1495 ± 7	69 ± 1.9	212 ± 22	121 ± 4

Table 2.2: Ring and gap positions from the MCMC fit to the Band 6 u, v-data.

	Gap 1	Ring 1	Gap 2	Ring 2
R [AU]	100 ± 6	130 ± 9	170 ± 13	220 ± 16

2.3.2 Spectral index analysis

The continuum observations of V1094 Sco show that in both Band 6 and Band 7, the structure is dominated by two azimuthally symmetric regions: the bright, inner "core" and a fainter,

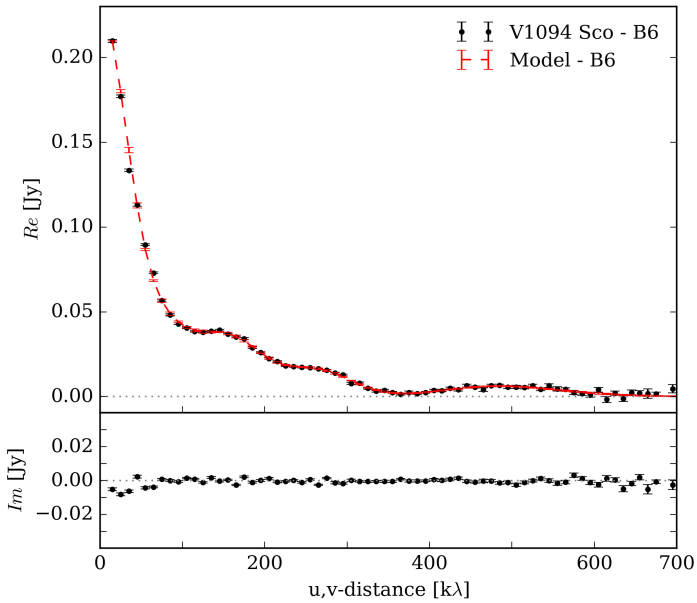

Figure 2.2: Best-fit model presented in Table 2.1 (red) and deprojected, derotated, and binned u, v-plane data for V1094 Sco (black).

more extended outer disk, where the rings are located. Directly linking intensity to dust properties is difficult, but necessary for tying these observations to models of ring formation. Thanks to the range in frequencies covered by our observations (between 234 and 328 GHz), the spectral index $\alpha_{\rm mm}$ of the continuum emission can be determined. In particular, if the intensity at a given radius is given by $I_\nu = B_\nu(T)(1 - e^{-\tau_\nu})$ and $\tau \sim \nu^\beta$, then if $\tau \gg 1$ and $h\nu/k_B T \ll 1$, $\alpha_{\rm mm} = 2$, while if $\tau \ll 1$, $\alpha_{\rm mm} = 2 + \beta$. However, these simple relations only hold in the Rayleigh-Jeans regime. If this does not apply, an extra (negative) temperature-dependent term appears, and values of $\alpha_{\rm mm}$ lower than two can occur.

The resolution and sensitivity of our data allow us to determine the spectral index as a function of radius. However, we cannot immediately use the results presented in Figure 2.1, since their imaging beam sizes and the u, v-plane coverage of the underlying data differ. To ensure that $\alpha_{\rm mm}$ contains only variations due to actual spectral index variations and image noise, the data were re-imaged with a circular, 0.25″-radius beam, using only baselines with lengths between $17 - 1260\,{\rm k}\lambda$. This is the largest baseline range with which it is possible to cover all the continuum spectral windows in both Band 6 and Band 7. The profile of $\alpha_{\rm mm}$ was subsequently derived by deprojecting and derotating the images in both bands, calculating the value of $\alpha_{\rm mm}$ and its standard error in each pixel, and radially averaging these values. Full maps of $\alpha_{\rm mm}$ and $\sigma(\alpha_{\rm mm})$ are included in Appendix 2.A, but here only the radially averaged profiles will be used.

The uncertainty in $\alpha_{\rm mm}$ at any point is determined primarily by two components: first, the noise properties of the images in both bands, and second, the absolute flux calibration errors in the images. The image noise consists of the random noise term to $\alpha_{\rm mm}$, which

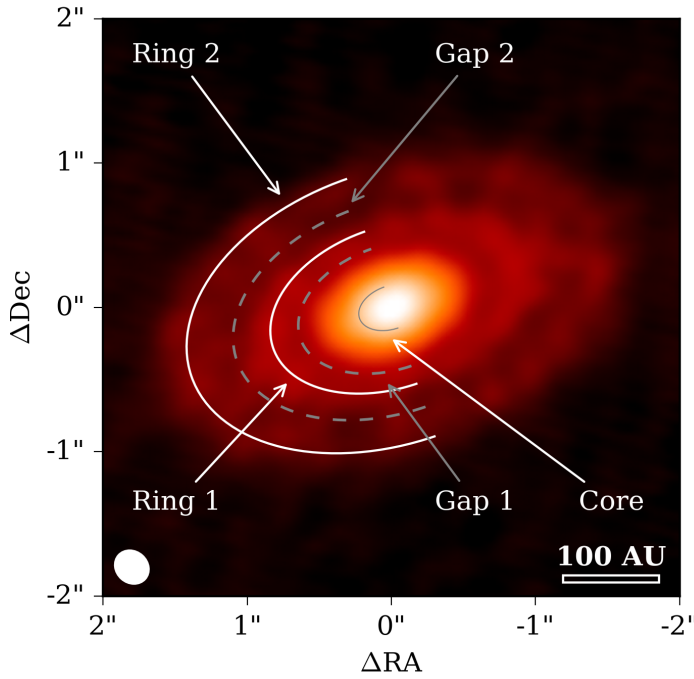

Figure 2.3: Best-fit locations of the bright rings (white) and gaps (gray) and the bright core (σ_1 in the model) as listed in Table 2.2, superimposed on the Band 6 continuum.

affects each beam separately, but is also affected by residual phase noise. This is particularly relevant for the Band 7 data. Figure 2.A.1 shows that the effect of this type of error does propagate into the $\alpha_{\rm mm}$-map. However, the result is that the radial spectral index profile becomes much noisier in those low S/N regions where the azimuthal asymmetries are located, which happens at distances beyond $\sim 1''$(150 AU). Therefore, we restrict the range of radii over which we discuss the spectral index variations to within this region.

In contrast to the random noise, the absolute flux calibration error adds a constant at all positions. Since our data have been self-calibrated, and the rms phase noise on the shortest baselines is less than 15%, assuming a 10% flux calibration error is appropriate in both bands (ALMA Partnership et al. (2017); MacGregor et al. (2017); see also Sect. 2.2). This uncertainty leads to an 0.42 error on $\alpha_{\rm mm}$. A third source of error, specific to the radial profile of the spectral index, is the impact of our self-calibration models on the resulting image properties. It is difficult to quantify the result of slightly different source models. However, in general, their main influence should be constrained to changes in the steepness of $\alpha_{\rm mm}(R)$ in the bright inner disk region (the inner 38 AU), where the self-calibration's impact is the largest. They may also introduce some extra noise in the radial profile.

The profile of the spectral index $\alpha_{\rm mm}(R)$, shown in Figure 2.4 shows several key features: a low spectral index in the inner disk, and a peak and subsequent drop at the location of the first gap identified in Sect. 2.3.1. Here we explore these features in more detail.

A cold inner disk

In the inner beam of our observations (dominated by the bright central component with characteristic radius 38 AU in the model fit in Sect. 2.3.1, see Figure 2.3), the spectral index appears to be consistent with $\alpha_{\rm mm} = 2.09 \pm 0.03$, increasing outward. The dominant source of error in this region is the flux calibration uncertainty in both bands, resulting in an absolute uncertainty in $\alpha_{\rm mm}$ over the entire image of 0.42.

If we assume the emission is in the Rayleigh-Jeans regime, then $\beta \lesssim 0.5$, a value that can only be reached if the particles have grown significantly, possibly down to gray ($\beta = 0$) opacity indicating grains with sizes much larger than the wavelengths of these observations. On the other hand, values for $\alpha_{\rm mm} \leq 2$ can be explained if the emission in this part of the disk is optically thick, or if the Rayleigh-Jeans approximation does not apply. In both of these cases, the intensity of the central part of the disk becomes sensitive to the temperature of the dust. The observed Band 6 peak intensity of 0.022 Jy beam^{-1} in the central 0.25″ beam corresponds to a brightness temperature of only 12.9 K if we assume the emission is optically thick. This suggests that the disk midplane could be cold enough for CO to be frozen out within a $\sim$ 20 AU radius.

To test the hypothesis of an optically thick inner disk, an independent dust temperature estimate is necessary. Previously, a temperature profile for V1094 Sco has been given by Tsukagoshi et al. (2011), who fit a power-law temperature structure to the disk's spectral energy distribution (SED). In their best-fit model, $T(R) = 99.3\,{\rm K}\left(\frac{\rm R}{1\,{\rm AU}}\right)^{-0.68}$, giving a temperature of 13 K at 20 AU. An additional check of a plausible range of midplane temperatures was done with the physical-chemical disk modeling code DALI (Bruderer et al. 2012; Bruderer 2013), which was used to perform dust radiative transfer calculations for a set of 45 disk models to obtain their dust temperatures, raytrace their emission, and image the data with the same 0.25″ beam used for the observations. These models were based on a parametric surface density structure and dust properties with values in a range that produces a near- to mid-infrared SED similar to that of V1094 Sco. The parameter ranges and sampling for these models are given in Appendix 2.B, Table 2.3.

In both approaches, the underlying disk density structure is smooth and does not contain rings or gaps, and both therefore have radially decreasing midplane temperature profiles. In the Tsukagoshi et al. (2011) model, the midplane temperature at 20 AU is 13 K. In the grid of DALI models, we find midplane temperatures of 20 ± 4 K at this radius. The resulting raytraced images of the disk show peak brightness temperatures between 17 and 10 K and a median temperature of 12.7 K, very close to the observed peak temperature. This shows that our observations are consistent with a cold inner disk for V1094 Sco.

An important consequence of the low midplane temperatures predicted by these models is that the midplane CO snow line, which is expected to be around 20 K for pure CO ice (Öberg et al. 2005a), is not or, in the most optimistic cases, is barely resolved. The gaps and rings are located far outside the inner 20 AU, meaning that another explanation for the presence of these features than the influence of a snow line is needed.

If the mm emission in this region is indeed optically thick, this implies that additional substructures could be present in the inner disk, not revealed by these data. High-angular resolution $\geq$ 3 mm data are needed to probe this region, and will also allow for a large reduction in systematic uncertainty in $\alpha_{\rm mm}$ across the disk.

Radial spectral index variations in the first gap-ring pair

The high S/N achieved in the image plane in both bands allows us to describe the radial variations of $\alpha_{\rm mm}$ out to a radius of $\sim$ 150 AU. Crucially, this region contains the first gap-ring pair in the disk, allowing us to place some constraints on the grain properties in these features.

As can be seen from Figure 2.4, $\alpha_{\rm mm}$ increases from 2.1 ± 0.03 in the inner disk, by ~ 0.9, toward 3.0 ± 0.2 in the first gap at 100 AU. Subsequently, the spectral index drops by ~ 0.7 to 2.3 ± 0.3 in the first ring at 130 AU. Some tentative hints of a subsequent increase in $\alpha_{\rm mm}$ can be seen towards the location of the second gap, but are very small compared to the (large) increase in image noise at those radii, and will therefore not be further discussed.

Due to the previously mentioned absolute flux calibration error, two possible interpretations for the behavior of $\alpha_{\rm mm}$ between $20-130$ AU can be found. On the one hand, the inner region may be optically thick. In this scenario, the material in the gap is optically thin with a $\beta \sim 1$, consistent with grain growth up to millimeter sizes in this region (Draine 2006), and the material in the first ring may be optically thick as well, or, interestingly, have a very low $\beta(\sim 0.3)$ due to a population dominated by grains with sizes larger than a few centimeters, even if the emission is not in the Rayleigh-Jeans regime.

Alternatively, the entire disk could be optically thin, so that β becomes even higher (up to $\sim$ 1.4) in the gap, requiring grains in the this part of the disk to be small (μm-sized), while larger grain sizes are found in the rings and central disk. Indeed, in simulations, local pressure maxima in the disk can reproduce both rings and gaps in disks as well as this type of spectral index profile, as shown in, amongst others, Pinilla et al. (2012).

Intriguingly, similar radial spectral index variations have so far also been identified observationally in both TW Hya and HL Tau (Huang et al. 2018; Liu et al. 2017; ALMA Partnership et al. 2015), suggesting that this behavior occurs more often in rings and gaps in protoplanetary disks. A decreasing β with radius is also present in HD 163296, although these observations lack the S/N to resolve the rings (Guidi et al. 2016).

2.4 Discussion

2.4.1 Comparing multi-ringed disks

Besides studying the detailed properties of a single object, the comparison of V1094 Sco with other multi-ringed disks, as well as with other disks in the Lupus star-forming region, can provide insight into the mechanisms that drive this peculiar emission morphology. Despite the small size of the sample of multi-ringed disks found in the literature, there is quite a large spread in the temperatures and luminosities of the stars around which they are found. For example, HD 163296 has an effective temperature of 9333 K and a luminosity of 36 $L_\odot$ (Natta et al. 2004) while V1094 Sco is both much cooler at $T_{\rm eff} = 4205$ K and an order of magnitude fainter with $L_\star = 1.95\,L_\odot$ (Alcalá et al. 2017). To facilitate the comparison between other disks in the literature, Figure 2.5 presents the normalized radial intensity profile of V1094 Sco compared to several other protoplanetary disks. The left panel compares the V1094 disk with two of the other largest and brightest Lupus disks, both around relatively cool stars: IM Lup ($T_{\rm eff} = 4350$ K) and Sz 98 ($T_{\rm eff} = 4060$ K) (Ansdell et al. 2016; Cleeves et al. 2016; Alcalá et al. 2017). The right panel compares the disk around V1094 with that of TW Hya, an old, massive, multi-ringed disk around a cool star with $T_{\rm eff} = 3800$ K (Sokal et al. 2018), and the previously mentioned Herbig Ae star HD 163296. All radial distances of the Lupus disks have

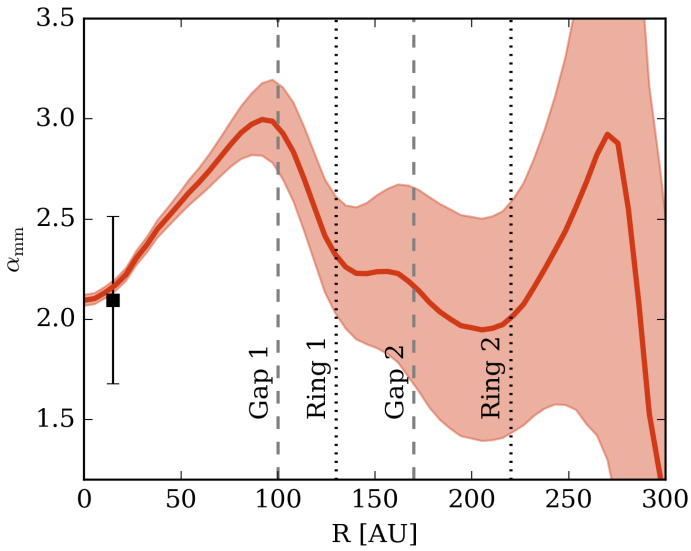

Figure 2.4: Spectral index as a function of radius (red) for V1094 Sco, with 1σ errors from image noise in light red. The impact of a flux calibration error of 10% is shown by the black error bar. The gaps are indicated with dashed gray lines and dotted black lines correspond to the bright rings.

been calculated assuming a uniform 150 pc distance (as opposed to the 200 pc distance, used in Ansdell et al. 2016, 2018).

Several conclusions can be drawn from Figure 2.5. First, it is clear that the continuum emission from V1094 Sco is similar in extent to that of IM Lup (Cleeves et al. 2016), with the caveat that the IM Lup observations shown here are with a larger beam width of 0.4″, and the outer radius might thus be smaller. This disk also seems to show a continuum break at similar radii of $\sim$ 100 AU and relative intensity to V1094 Sco. Such a break is also seen in Sz 98, albeit at a higher intensity relative to the peak flux and a smaller radius ($\sim$ 80 AU). Intriguingly, Tazzari et al. (2017) found ring-like residuals for this disk when fitting it with a smooth decreasing surface density profile, implying there may be additional structures present in this object. The older TW Hya disk, in contrast, is much more compact than the Lupus disks compared here. This source also shows substructures down to much smaller scales, which would not be resolved with the beam used for the other sources, demonstrating that rings in protoplanetary disks are not necessarily limited to the most radially extended objects.

It is illustrative to compare the observed intensity profile of V1094 with that of HD 163296 as derived by Isella et al. (2016). While HD 163296 is more compact than V1094 Sco, the two disks share remarkably similar intensity profiles, with a central core and more extended outer region, which hosts two rings. The more compact central core of the HD 163296 disk is at least in part due to the smaller beam of the Isella et al. (2016) observations (0.2″ at a distance of 122 pc).

The difference in ring locations around both stars is significant, since it provides an additional, independent indication that snow lines are an unlikely explanation for the rings

in V1094 Sco: in the hotter HD 163296 system, the rings are located further inward. This contrasts with the result in Zhang et al. (2016), who found an overlap in the (inner) ring and gap of HD163296 and the CO snow line, as well as coinciding rings and CO snow lines in the T Tauri stars in their sample (HL Tau and TW Hya). However, both of these T Tauri disks are much more compact than the V1094 Sco disk.

An alternative explanation for the formation of rings, the presence of a magnetohydrodynamic dead zone, also does not appear to be sufficient. Although the models presented by Flock et al. (2015), for instance, show a ring and gap at the outer edge of the dead zone, their model does not lead to a double ring structure, such as in these disks. However, the total (gas+dust) column density where the Flock et al. (2015) model predicts a gap and ring is similar (at $\sim 3\,\mathrm{g\,cm^{-2}}$) to that of the best-fit V1094 Sco model of Tsukagoshi et al. (2011) at 100 AU, indicating that one of the rings could be linked to the dead zone edge. Alternatively, the change in turbulence inside the dead zone may be an explanation for the bright inner region of the disk and the "fried-egg" morphology of the emission. The volatile snow lines, located inside 20 AU, may contribute to the bright inner core region, as per Banzatti et al. (2015).

A (secular) gravitational instability (GI) or the effect of planets are both plausible mechanisms for ring formation at large radii. Secular GI effects can form rings at 100 AU scales around Sun-like stars (Takahashi & Inutsuka 2014). Likewise, it is well established that one (or more) previously formed planets of sufficient mass can form gaps and rings of dust in protoplanetary disks (Papaloizou & Lin 1984); however, the nature of the planets (their mass and the number of planets per gap) is difficult to constrain based on these data alone. Observations of V1094 Sco by the Strategic Explorations of Exoplanets and Disks (*SEEDS*) survey have not led to the detection of a companion (Uyama et al. 2017); however, the median sensitivity of those observations is between $4-10\,M_J$ in the $100-300$ AU region. This means that even a quite massive planet could easily escape detection using current instruments. Alternatively, perhaps several lower-mass planets are responsible for one or both of the observed gaps.

2.4.2 The occurrence rate of large dust disks

Since our survey of disks in Lupus is – with the addition of this sample from the Lupus completion survey (see Sect. 2.2) – complete, it is now for the first time possible to place concrete upper limits on the occurrence rate of bright, radially extended disks. Here, we look at the radii of disks based on their millimeter-continuum emission. Although ^{12}CO emission is often more extended than the continuum, (Ansdell et al. 2018) show that the average ratio $R\mathrm{gas}/R_{\mathrm{dust}}$ is within a factor $1.5-3$ in Lupus. In total, there are 95 Class-II sources in the Lupus clouds. Of these disks, IM Lup and V1094 Sco are by far the most extended with radii up to ~ 300 AU, assuming a 150 pc distance, with the next largest disk at a radius of ~ 160 AU. This implies an occurrence rate of $2.1 \pm 1.5\%$ for these largest disks.

Given the high surface densities at large radii of disks like V1094 Sco and IM Lup, and the finding of rings in V1094 Sco that could be sculpted by planet-disk interactions, it is interesting to compare the statistics of large disks to the number of massive planets at large orbital radii. Bowler (2016) find an occurrence rate of $< 2.1\%$ for planets in orbits between $100-1000$ AU with masses of $5-13\,M_J$, around $5-300$ Myr-old stars across all spectral types. In contrast, the number of full (non-transitional) disks in Lupus where continuum emission was detected beyond 100 AU is significantly larger: $8 \pm 3.0\%$ of the full population (van der Marel et al. 2018a). Since we might not detect disks with fainter continuum emission at

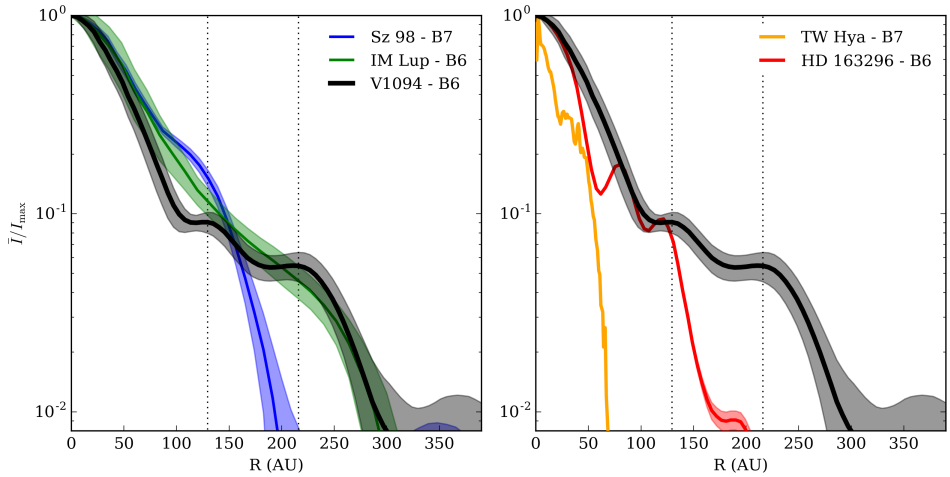

Figure 2.5: Normalized radial intensity profile of V1094 Sco compared to two large Lupus disks (IM Lup and Sz 98; Ansdell et al. 2016; Cleeves et al. 2016) (left panel) and to two multi-ringed disks (TW Hya and HD 163296; Andrews et al. 2016a; Isella et al. 2016). The locations of the rings of V1094 Sco are indicated with vertical dotted lines. For all Lupus sources, a 150 pc distance is assumed. The effective resolution of the Sz 98 and V1094 Sco disks is 38 AU; for IM Lup, 65 AU; for TW Hya, 1.6 AU; for HD 163296, 27 AU.

large radii, this is a lower limit to the actual number of these disks. If we also consider the Lupus transition disk population, the number of disks with continuum emission beyond 100 AU further increases, to 18 ± 4.3%. However, these transition disks are consistent with clearing by planets interior to the gap radius, which is < 100 AU for the entire sample (van der Marel et al. 2018a). Thus, the transition disk population is not necessarily comparable to the statistics of massive exoplanets in the $100 - 1000$ AU interval.

The exoplanet occurrence rates discussed here are, in either case, much smaller than the number of disks with significant amounts of continuum emission at similar radii. However, the statistics of the extrasolar planet population at these orbital radii are very incomplete, especially for lower-mass planets ($< 5\,M_J$) around fainter stars. Thus, it is possible that the discrepancy in the occurrence rate of planets at large orbital radii is due to the disks forming mostly lower-mass planets. Indeed, no particularly massive planets are needed to open detectable gaps at large orbital distances, since the Hill sphere radius increases linearly in orbital distance but only as the third root of mass. Both Isella et al. (2016) and Dipierro et al. (2018), for instance, find planet masses below $5\,M_J$ are sufficient to form gaps in HD 163296 and Elias 2-24 respectively. Alternatively, the large difference in planet detection statistics could be due to significant planet migration moving most of the planets that formed at large distances from their stars to smaller orbits.

Apart from comparing the population of large disks directly to the exoplanet population, relating large primordial disks to the entire Lupus transition disk sample is also informative. Interestingly, although transition disks with large cavities make up $\gtrsim 11 \pm 3.7\%$ of the disks in Lupus (van der Marel et al. 2018a), they are strongly over-represented in the sample of largest disks: 50% of disks with continuum radii in the upper octile show evidence of central cavities in their continuum emission. This led van der Marel et al. (2018a) to propose a two-

mode evolutionary sequence for protoplanetary disks. In this view, large primordial disks like V1094 Sco and IM Lup are the progenitors of transition disks, while the majority of lower-mass, more compact disks may evolve through a different pathway, either without a transitional stage or as a scaled-down version of the pathway of the large disks. The massive primordial disks may trap dust by some means (possibly through planet-disk interactions, or by some other mechanism), which prevents its inward drift. This leads to the formation of rings and, later, the emergence of a large, possibly multi-ringed, transition disk with a large dust cavity.

In the context of this hypothesis, it is possible to interpret the ratio of large primordial disks to transition disks as an indication of the speed at which this evolution occurs. Since half the disks larger than 120 AU are transition disks at the $1 - 3$ Myr age of Lupus, this process should take place on $\sim$ 1 Myr timescales. Importantly, this means we have a testable prediction for the occurrence rate of large primordial disks in other star-forming regions: they should be rarer in more evolved regions, and more common in younger systems, if the absolute rate of evolution across regions is the same. In terms of disk mass, too, it is then expected that the disk mass distribution in more evolved regions is dominated by a small number of transition disks, while younger regions should have an upper mass distribution with mostly large primordial disks. Although statistics across other regions at similar sensitivity and resolution are still lacking, this framework is at least consistent with the observation of several large, multi-ringed systems in very young systems: HL Tau, Elias 2-24, and AS 209 are all at most 1 Myr old (ALMA Partnership et al. 2015; Andrews et al. 2010; Dipierro et al. 2018; Natta et al. 2006; Fedele et al. 2018). However, such young systems tend to be brighter, leading to an observational bias for high-resolution imaging campaigns toward these disks, which in turn results in their over-representation in the already small sample of multi-ringed disks.

2.5 Conclusions

In this work the nature of V1094 Sco as a giant, multi-ringed protoplanetary disk is identified for the first time, based on data from the Lupus survey of protoplanetary disks. Analyzing its structure and comparing this disk to the rest of the Lupus disk population allows us to exclude some pathways for ring formation, and provides a possible link to a general disk formation picture. Our results are summarized as follows:

- Continuum emission from V1094 Sco extends out to 300 AU from the central star, making it larger than the other Lupus disks by a factor ~ 5, but similar in size to the well-studied IM Lup disk.

- Two bright rings are identified at 130 and 220 AU, separated by gaps at 100 and 170 AU, based on a u,v-plane fit of the intensity profile.

- Disks with continuum radii of this size (> 200 AU) are rare: only $\sim 2\%$ of the Class II objects in Lupus are giant disks similar to V1094 Sco.

- Radial variations in $\alpha_{\rm mm}$ are consistent with optically thick emission in the bright disk core. The spectral index increases at the location of the first gap, and subsequently decreases again towards the first ring, possibly as a result of efficient grain growth in this ring.

- Based on the temperature of the optically thick emission and on independent disk models, the midplane dust temperature at the ring locations is too low for snow lines to be a valid explanation, while a dead zone would only be expected to cause one ring. However, gravitational instabilities or the presence of planets up to $\sim 10\,M_J$ in the gaps cannot be excluded.
- The number of primordial disks with continuum emission at radii > 100 AU in Lupus seems to be much larger than the occurrence rate of giant planets with $5 - 13\,M_J$ between $100 - 1000$ AU. The large disk/transition disk ratio may be a probe of disk evolution, if large multi-ringed disks evolve into (multi-ringed) transition disks with large cavities on ~Myr timescales.

Appendix

2.A Spectral index map of V1094 Sco

Figure 2.A.1 shows the full maps of $\alpha_{\rm mm}$ and $\sigma(\alpha_{\rm mm})$ that were used to construct the radial $\alpha_{\rm mm}$ profile discussed in Section 2.3.2. Pixels in both Band 6 and Band 7 with $S/N < 2.5$ were masked.

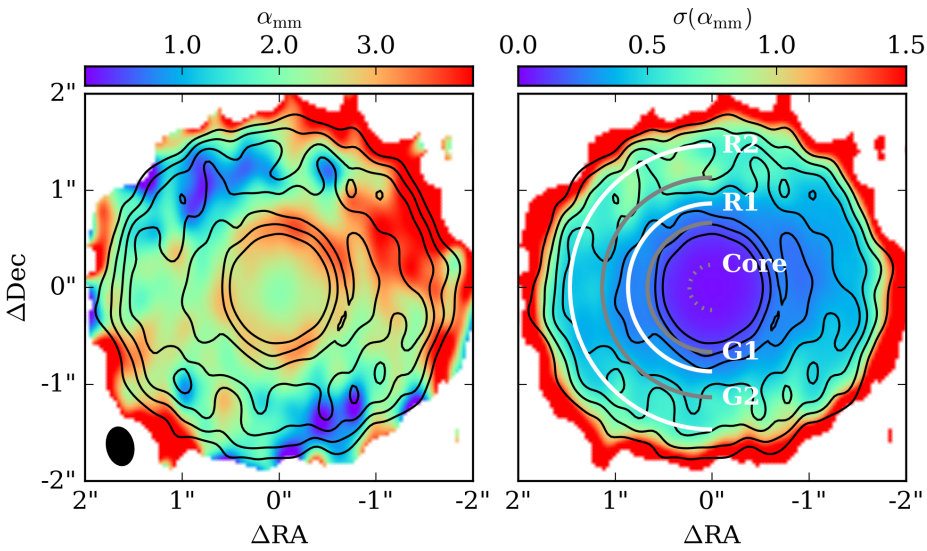

Figure 2.A.1: Left: $\alpha_{\rm mm}$, deprojected and derotated. Right: Standard error on $\alpha_{\rm mm}$, not including the ±0.42 offset due to flux calibration errors. The Band 6 data are overplotted in black, with contours at 3, 5, 7.5, 10, 15, 20, and 30σ. The locations of the rings (R1 and R2), gaps (G1 and G2), and the bright core are indicated with white and gray arcs.

2.B Midplane temperatures of V1094 Sco disk models

In Table 2.3, the parameters chosen for our DALI mini-grid of V1094 Sco-like disks are listed. DALI (Bruderer et al. 2012; Bruderer 2013) is a physical-chemical code that was used to perform dust radiative transfer calculations for the range of dust distributions, and to obtain the dust temperatures and raytrace their emission.

The disk models themselves are based on the parametric disk density structure introduced in Andrews et al. (2011), here truncated at a radius R_c, so that $\Sigma(R) = \Sigma_c \left(\frac{R}{R_c}\right)^{-\gamma} \times \exp\left((R/R_c)^{2-\gamma}\right)$. The truncation radius R_c was set to 250 AU based on the Band 6 continuum image, and we fix γ to 0.6. For a full disk, the key parameters are then the total mass (gas + dust) M_d, the scale height h_c (the standard deviation of the vertical Gaussian distribution of the dust), flaring angle ψ (defined so that $h(R) = h_c(R/R_c)^{\psi}$), the large grain fraction f_{ls}, and the relative settling factor χ, which sets the large grain scale height as $h_{c\,\rm large} = \chi h_c$. Large grains have sizes up to 1000 μm, while small grains do not exceed 1 μm in size. The

total mass was fixed at 0.1 $M_\odot$, reproducing the Band 6 continuum flux assuming a gas to dust ratio of 100.

Table 2.3: Parameter ranges and number of samples for the disk models.

Parameter	minimum	maximum	$N_{\rm samp}$
Scale height h_c	0.02	0.1	4
Flaring angle ψ	0.1	0.3	3
Large grain fraction f_{ls}	0.85	0.99	2
Settling parameter χ	0.2	1.0	2

Table 2.4: Stellar properties used for the disk models.

$M_\star$ [a]	$R_\star$	L_{star}	$T_{\rm eff}$	SpT	d
$[M_\odot]$	$[R_\odot]$	$[L_\odot]$	[K]		pc
0.92	1.9	1.7	4205	K6	150

Notes. Values derived from Alcalá et al. (2017) assuming a 150 pc distance to the disk.
[(a)] Mass derived with the Siess et al. (2000) model grid.

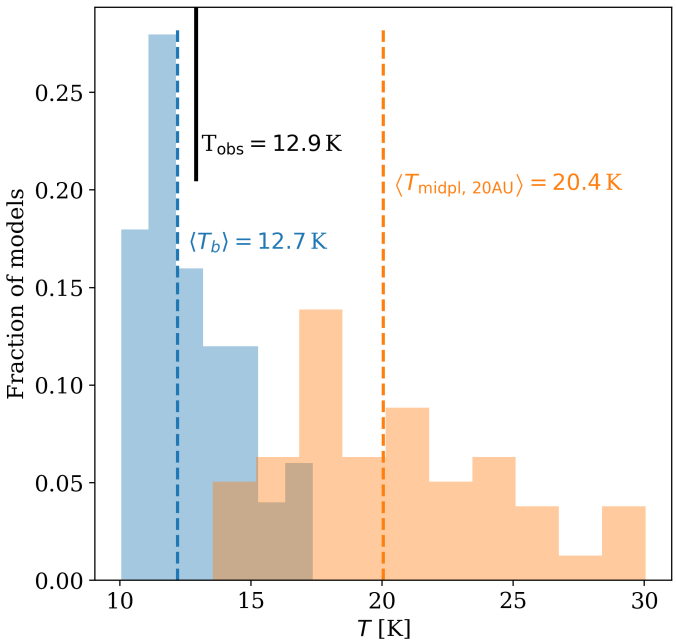

Figure 2.B.1: DALI model midplane temperatures at 20 AU (orange) and Band 6 peak brightness temperatures (blue) after convolution with an 0.25″ beam for a grid of disks. The black line indicates the observed peak brightness temperature of V1094 Sco. For pure CO ice in typical disk midplane conditions, the freeze-out temperature is 20 K (Öberg et al. 2005).

3

The ALMA Lupus protoplanetary disk survey: evidence for compact gas disks and molecular rings from CN

S.E. van Terwisga, E.F. van Dishoeck, P. Cazzoletti, S. Facchini, L. Trapman, J.P. Williams, C.F. Manara, A. Miotello, N. van der Marel, M. Ansdell, M.R. Hogerheijde, M. Tazzari, and L. Testi.
2019, A&A, 623, 150

Abstract

The cyanide radical CN is abundant in protoplanetary disks, with line fluxes often comparable to those of ^{13}CO. It is known to be sensitive to UV irradiation of the upper disk atmosphere, with models predicting ring-shaped emission.

Aims: We seek to characterize the CN emission from 94 Class-II disks in the Lupus star-forming region, compare it to observations in other regions, and interpret our observations with a grid of models. The CN emission morphology is discussed for two primordial disks, Sz 71 and Sz 98, and is modeled in more detail.

Methods: ALMA observed CN $N = 3-2$ in Lupus disks down to sensitivities better than previous surveys. Models constructed with the physico-chemical code DALI are used to study the integrated fluxes of the disks and resolved emission of CN in disks without (dust) substructures.

Results: CN $N = 3-2$ is bright, and detected in 38% of sources, but its disk-integrated flux is not strongly correlated to either ^{13}CO or continuum flux. Compared to pre-ALMA single-dish surveys, no significant difference in the CN flux distributions in Lupus and Taurus-Auriga is found, although ρ Ophiuchus disks may be fainter on average. We find ring-shaped CN emission with peak radii of ~ 50 AU in two resolved disks.

Conclusions: A large fraction of sources are faint in CN; only exponential gas surface density cutoffs at $R_c \leq 15$ AU can reconcile observations with models. This is the first observational evidence of such a compact gas disk population in Lupus. Absolute intensities and the emission morphology of CN are reproduced by DALI models without the need for any continuum substructure; they are unrelated to the CO snowline location. The observations presented here, together with the modeling of these rings, provide a new probe of the structure and conditions in disks, and particularly their incident UV radiation field, if disk size is determined from the data.

3.1 Introduction

The primary motivation for the study of protoplanetary disks is to understand the formation of planetary systems. For this purpose it is essential to characterize the structure and composition of both dust and gas in the disks, with different molecules providing different information on the gas structure and conditions.

Initially, most disk observations were limited by low spatial resolution and sensitivity, and focused on disk-integrated observations of well-known, bright objects (see the review by Henning & Semenov 2013). In recent years, ALMA has been instrumental in detecting as well as resolving millimeter(mm)-sized dust and a number of gas species near the midplanes of protoplanetary disks, thus providing a new window on the environment where planets are formed. A number of large, unbiased, and deep surveys have significantly improved our understanding of the protoplanetary disk populations in nearby star-forming regions (e.g., Andrews & Williams 2005; Pascucci et al. 2016; Barenfeld et al. 2016; Ansdell et al. 2016). Among the puzzling results from these surveys is the weaker-than-expected CO isotopolog emission when assuming normal CO abundances and an interstellar medium(ISM)-like gas-to-dust ratio (Ansdell et al. 2016; Miotello et al. 2017; Long et al. 2017).

While most of these surveys focused exclusively on the (resolved) continuum emission of Class-II disks, or on CO and its isotopologs, relatively few surveys have targeted other molecular species. Targeting other molecules is scientifically valuable: if their chemistry is sufficiently well understood, they can provide additional independent constraints on the properties of disks. However, molecular lines are often faint, or the chemical pathways behind their formation and destruction not well understood, making them less attractive targets for a survey.

The cyanide radical (CN) is, in this context, of particular interest. After ^{12}CO, it is one of the brightest molecules in disks, and has line fluxes comparable to or higher than those of ^{13}CO (e.g., Dutrey et al. 1997; Thi et al. 2004; Öberg et al. 2011; Salter et al. 2011). Due to its brightness, several large single-dish surveys of this molecule have already been performed using the IRAM 30-meter telescope (Guilloteau et al. 2013; Reboussin et al. 2015). Together these surveys cover 74 disks in Taurus and ρ Ophiuchi. However, the samples studied suffer from two key drawbacks: they are not complete, and are biased towards the brightest or most radially extended sources at mm wavelengths.

Despite these issues, the abundance of CN has been suggested to be enhanced in Class-II versus Class-I disks (Kastner et al. 2014; Guilloteau et al. 2016). Also, Guilloteau et al. (2014) successfully used the cyanide radical as a stellar mass probe. However, in order to get a better understanding of the dependence of CN on disk properties, it is necessary to use an unbiased, large, and uniformly observed sample of disk observations.

The observational basis for this study is the complete survey of Class-II disks in the Lupus star-forming region (Ansdell et al. 2016, 2018). This survey offers good angular resolution at $\sim 0.3''$, or a $\sim$ 24 AU radius at 160 pc (the typical distance for these objects, based on *Gaia* DR2 Gaia Collaboration et al. 2018; Bailer-Jones et al. 2018). The sensitivity of this dataset is a factor of approximately three better than previous large single-dish CN surveys. Moreover, the sample studied here is unbiased. By covering 94 of 95 Class-II disks in Lupus I, III, and IV with stellar masses $\geq 0.1\,M_\odot$, this survey is very complete and more than doubles the total number of disks observed in CN.

From an evolutionary perspective, the objects in the Lupus survey must be relatively close in age, around $1-3$ Myr (Comerón 2008b), and formed in a similar environment. This reduces the impact of different disk ages on observational properties. Finally, the Lupus

disks have been characterized at multiple wavelengths. Apart from the dust continuum, the Lupus disk survey targeted ^{12}CO and its most common isotopologs, ^{13}CO and C^{18}O. Additionally, intermediate-resolution *XSHOOTER* spectra of most sources in the sample have also been taken (Alcalá et al. 2014, 2017), meaning that accurate measurements of the host star properties and accretion rates are available.

Apart from providing disk-integrated observations of CN towards many sources, resolved images are also obtained, even at integration times of just one minute. In comparison to pre-ALMA interferometric studies of individual objects (e.g., Öberg et al. 2011; Guilloteau et al. 2014), our effective physical resolution is improved by a factor of ≥ 2. With these short integration times, the signal-to-noise ratio (S/N) of the molecular gas emission is low: for the brightest sources in CN, the line peak has a $S/N \approx 12$ relative to the channel noise. However, we are able to discuss in greater detail the ring-like radial distribution of CN emission in two favorably inclined, bright sources, and study its underlying causes in a general way.

This is relevant because, in recent years, the high-resolution capabilities of ALMA have lead to the discovery of many rings and other radial structures, in gas emission (e.g., Kastner et al. 2015; Teague et al. 2017) and in dust (e.g., ALMA Partnership et al. 2015; Isella et al. 2016), in a variety of sources and molecules. These structures occur both in transitional disks, which are characterized by central cavities in their dust distribution (Espaillat et al. 2014; van der Marel et al. 2016b) as well as in full disks, which are the focus of this article. Indeed, ALMA observations of TW Hya also show CN to be distributed in a ring (Teague et al. 2016), suggesting this type of emission morphology may be more common for this species.

For molecular species with ring-like emission, several different processes have been identified as their root cause: CO is depleted in at least some of the gaps in the dust in the HD 163296 system (Isella et al. 2016), while CS emission coincides with a region of decreased dust surface density in TW Hya (Teague et al. 2017). More complex chemical processes also play a role for some species: dust grains locking up volatile carbon and oxygen in the outer disk have been suggested as an explanation for rings observed in C_2H and c-C_3H_2 (Kastner et al. 2015; Bergin et al. 2016). Snow lines are also an important mechanism for causing the ring-like emission of some molecules. For instance, N_2H^+ is distributed in a ring in several disks (Qi et al. 2013, 2015), of which the radius is sensitive to the position of the CO ice line (Aikawa et al. 2015; van 't Hoff et al. 2017b). Many other molecular species are now showing a rich variety of emission morphologies, including single and multiple rings: DCO^+, DCN, H^{13}CN, and H^{13}CO$^+$, H_2CO (Mathews et al. 2013; Öberg et al. 2015; Huang et al. 2017; Carney et al. 2017; Salinas et al. 2017). However, for many of these species, finding the underlying cause of the emission morphology from observations alone is difficult, due to the variety in emission profiles between different molecules, and between disks.

To study integrated fluxes and the radial distribution of CN emission in disks, the chemical network that sets its formation and destruction must be understood. Significant advances have recently been made on this front: the physical-chemical code DALI (Bruderer et al. 2012; Bruderer 2013), which self-consistently calculates the chemical and thermal structure of the disk models, has been expanded to include nitrogen chemistry (Visser et al. 2018) using the most recent rates and branching ratios from Loison et al. (2014). Moreover, DALI now uses updated UV cross-sections for CN photodissociation (Heays et al. 2017). This allows us to predict the CN emission expected for a wide variety of disks, and study how the models depend on various disk parameters, such as radius, mass, and incident UV flux (Cazzoletti et al. 2018). Several key predictions have been found: first, an increasing integrated CN flux with increasing disk size; second, a strong dependence of CN flux on the UV radiation field of

stars; and third, a relatively weak dependence on total disk mass and on the volatile carbon abundance. In terms of the distribution of CN emission over the disk, a ring-like morphology is always found in the models, with the ring radius depending on the characteristic radius R_c of the gas disk, the vertical profile of the disk, and the UV radiation field.

In this paper, we discuss the CN emission in the full Lupus Class-II disk population (Section 3.3), investigate possible correlations with other disk tracers, and compare the Lupus disks to previous large single-dish surveys. In Section 3.3.3, the properties of the full disk sample are compared to a DALI model grid, focusing on the consequences for disk gas radii and the sensitivity to UV radiation. To investigate resolved CN emission, two full (i.e., non-transitional) disks are described in detail (Section 3.4). These disks – Sz 98 and Sz 71 – are amongst the brightest sources in CN, have clearly detected and resolved emission in both lines and continuum, and are not strongly inclined (around 45°). Section 3.4.2 discusses individual DALI models for CN emission in Sz 98 and Sz 71 to see if a smooth power-law surface-density distribution can reproduce their CN intensity profiles.

3.2 Observations and data reduction

The data for this project are part of the ALMA Lupus disk survey (Ansdell et al. 2016, 2018), which targeted 86 Class-II stars with ALMA Band 7 and 6 (ID: 2013.1.00220.S, 2015.1.00222.S, PI: J. Williams), combined with the 7 sources from the Lupus Completion Survey (ID: 2016.1.01239.S, PI: S. van Terwisga).

To these 93 disks, we add previously published data for IM Lup (Öberg et al. 2011). On top of the ^{12}CO $J = 2-1$, ^{13}CO, and C^{18}O $J = 2-1$ and $J = 3-2$ lines, and 335 and 225 GHz continuum, the spectral settings of these surveys targeted the CN $v = 0$ $N = 3-2$ transition in Band 7. Of the fine-structure transitions of this molecule, we focus on the brightest ($J = 7/2 - 5/2$) line, and in particular the $F = 7/2 - 5/2$ and $F = 9/2 - 7/2$ transitions at 340.247770 GHz and the partially overlapping $F = 5/2 - 3/2$ transition; all others are too faint to be detected in our data but these transitions together are responsible for 95% of the flux in the $J = 7/2 - 5/2$ line in the optically thin case (Hily-Blant et al. 2017). CN was observed at a lower spectral resolution of 0.24 MHz compared to ^{13}CO $J = 3-2$, for which a 0.12 MHz resolution was used. The analysis in this article mainly focuses on the Band 7 results, and only uses the Band 6 ^{12}CO $J = 2-1$ data.

In Band 7, all M-type stars were observed for 1 minute on source, while earlier-type stars were observed for 30 s, giving continuum sensitivities of 0.25 and 0.41 mJy beam^{-1}. Band 6 integration times were twice as long. For the sources in the Lupus Completion Survey, longer integration times were used, of 3.5 and 4.5 minutes in Bands 6 and 7, respectively, but a smaller beam lead to similar sensitivities (Ansdell et al. 2018); otherwise all observing parameters were identical.

Pipeline calibration of the data was performed by the NRAO. Flux, phase, bandpass and gain were calibrated using observations of Titan, J1427-4206, and J1604-4228, and J1610-3958, respectively. We also performed self-calibration on the data in order to maximize the S/N of the resulting images. Phase- and gain self-calibration were performed for all objects at the largest solution interval of one minute (for the highest sensitivity). These disks are not so bright as to be dominated by phase- and gain noise even in the continuum images, but this procedure resulted in an improvement in S/N.

Both continuum and line imaging were performed using the *clean* task in CASA. The continuum of the sources discussed in detail here was imaged using Briggs weighting with a robust parameter of +0.5 after averaging over all continuum channels, which optimized our

resolution and S/N in the image. The resulting effective beam size in Band 7 is $0.3'' \times 0.3''$, while in Band 6 it is $0.27'' \times 0.27''$. In the Lupus completion survey, the beams were $0.25'' \times 0.22''$ (Band 6) and $0.19'' \times 0.18''$ (Band 7), respectively.

The CN channels were binned for an effective velocity resolution of $0.5\,\mathrm{km\,s^{-1}}$, and imaged using natural weighting to maximize S/N. The resulting typical beam shape is $0.37'' \times 0.31''$; for the Lupus completion survey it is $0.22'' \times 0.20''$. The ^{12}CO $J = 2 - 1$ and ^{13}CO $J = 3 - 2$ lines were imaged with the same parameters. In these observations, the typical resulting channel rms of these CN observations is $10\,\mathrm{mJy\,beam^{-1}}$. The median noise level on the disk- and velocity-integrated line fluxes is $48\,\mathrm{mJy\,km\,s^{-1}}$.

Of the 93 disks observed with ALMA, we focus specifically on the two brightest disks that are moderately inclined ($< 50°$), resolved across multiple beams, have high-S/N moment-zero maps, and do not show any signs of depleted inner dust cavities. For these two disks, Sz 98 and Sz 71, it is possible to study the spatial distribution of CN. To generate and analyze the moment-zero maps at the highest sensitivity without introducing bias (by, e.g., using significance cuts in the individual channels), image-plane Keplerian masking was used to create their moment-zero maps (Loomis et al. 2018; Salinas et al. 2017). For this method to work, several properties of the system must be known. The stellar masses have been derived by determining the stellar properties of the targets with optical spectroscopy (Alcalá et al. 2017) and comparing the stellar temperature and luminosity with evolutionary models by Siess et al. (2000), while the mm-continuum observations allowed us to constrain the position angles and inclinations of the disk using the *imfit* task in CASA, version `4.3.1`. These results are combined with a line-width uncertainty factor (here taken as $0.5\,\mathrm{km\,s^{-1}}$ for CN, and $0.3\,\mathrm{km\,s^{-1}}$ for the CO isotopolog lines) which accounts for uncertainties in the precise stellar position, the disk position angle and inclination, and the effect of adjacent hyperfine lines in CN (specifically, the partial overlap of the $F = 7/2 - 5/2$ and $F = 9/2 - 7/2$ transition with the $F = 5/2 - 3/2$ transition). The resulting mask allowed us to use only those voxels in the objects' data cubes in which a signal can be reasonably expected. Compared to a normal moment-zero map, the biggest gain in sensitivity using this mask is in the outer regions of the disk, where (often) only a single channel contains a line signal. For ^{13}CO in Sz 98, we additionally used u, v-plane tapering to create a $0.5''$ circular beam, in order to maximize S/N.

3.3 Integrated CN flux survey results

The full Lupus sample consists of 95 Class-II disks, 93 of which have been observed in CN in this survey. Of the two missing objects, Sz 91 and IM Lup, only Sz 91 has no CN observations available. Instead of the CN $N = 3 - 2$ transition, CN $N = 2 - 1$ has been observed and detected towards IM Lup by Öberg et al. (2011).

In these observations, 36 of 94 sources are detected, for a total detection rate of 38% across the sample. All but three of these sources are also detected in ^{13}CO. The brightest sources in terms of CN flux are the transition disk J16083070-3828268 (van der Marel et al. 2018a), Sz 98, V1094 Sco (van Terwisga et al. 2018a), IM Lup, Sz 133, and Sz 71. Interestingly, the transition disks with large inner cavities in the sample that were identified in van der Marel et al. (2018a) are all detected in CN. These sources were also found to be among the brightest in the sample in continuum and ^{13}CO emission. Integrated fluxes for these objects were determined in the same way as those in Ansdell et al. (2016, 2018): circular aperture photometry was performed on the source position after integrating over all channels with significant emission, with the smallest aperture containing the full disk flux determined using a curve-of-growth method.

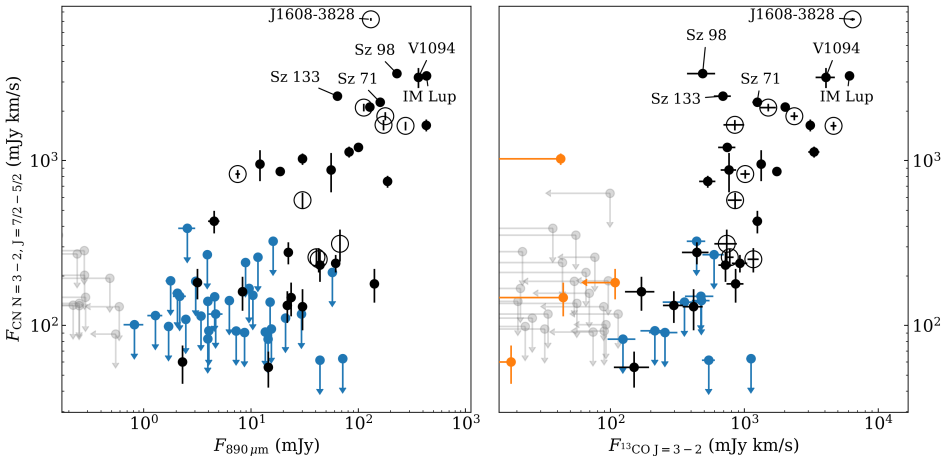

Figure 3.1: Disk-integrated CN $N = 3 - 2$, $J = 7/2 - 5/2$ vs. Band 7 continuum *(left panel)* and integrated ^{13}CO $J = 3 - 2$ fluxes *(right panel)* for the Lupus disk sample. Detected sources are black, CN upper limits are blue, ^{13}CO upper limits orange, and double upper limits are gray. Transition disks are marked with a circle. All upper limits are at the 3σ level. The six brightest disks are labeled.

For nondetections, a beam-sized aperture was used, and a conservative velocity range with a width of 10 km s^{-1}, to be consistent with our previously used noise definitions.

3.3.1 CN versus other disk tracers: ^{13}CO and continuum

The large, unbiased sample of Class-II disks in Lupus allows us to compare the resulting CN fluxes to the other important disk tracers: their continuum flux (proportional to the disk dust mass, if we assume the emission to be optically thin at these wavelengths) and integrated ^{13}CO $J = 3 - 2$ emission, which is the most commonly detected CO isotopolog, and more optically thin than ^{12}CO $J = 2 - 1$. The results of this comparison are presented in Figure 3.1. Appendix 3.A shows CN versus the C^{18}O emission in Figure 3.A.1, but we do not discuss it further here due to the low detection rate of this molecule in both Band 6 and Band 7.

The CN fluxes detected towards Lupus span several orders of magnitude, and are presented in full in Table 3.E.1. Compared to the continuum- and ^{13}CO fluxes, a large scatter becomes apparent, of several orders of magnitude, especially due to the impact of upper limits in the data. Consider, for example, the position of Sz 71 (labeled) in both panels of Figure 3.1: a source with similarly bright ^{13}CO is undetected in CN, while another disk with a similar 890 μm flux has CN emission that is an order of magnitude fainter. Similar behavior is seen in the other direction.

To formally test for correlations between these observables, a modified Kendall-rank test taking into account upper limits was used (Isobe et al. 1986). This test confirms that neither the 890 μm continuum nor the ^{13}CO $J = 3 - 2$ line flux are correlated with the CN flux ($p > 0.05$), consistent with the results from the IRAM 30-m telescope survey in Taurus-Auriga by Guilloteau et al. (2013). Not being able to reject the null result does not mean that no information can be extracted from this figure; however, to do so, more sophisticated

models are needed, which are discussed in Section 3.3.3.

3.3.2 CN in Lupus versus Taurus-Auriga and ρ Ophiuchi

Comparing the results of the Lupus sample to those of other literature surveys allows us to test if different regions (possibly with different ages, typical disk sizes, or external UV fields) have different CN emission properties. Here, we compare the Lupus CN observations to the results presented for CN in Guilloteau et al. (2013) and Reboussin et al. (2015), who targeted 42 and 30 stars respectively with the IRAM 30-m single-dish telescope, primarily in the Taurus-Auriga and ρ Oph star-forming regions.

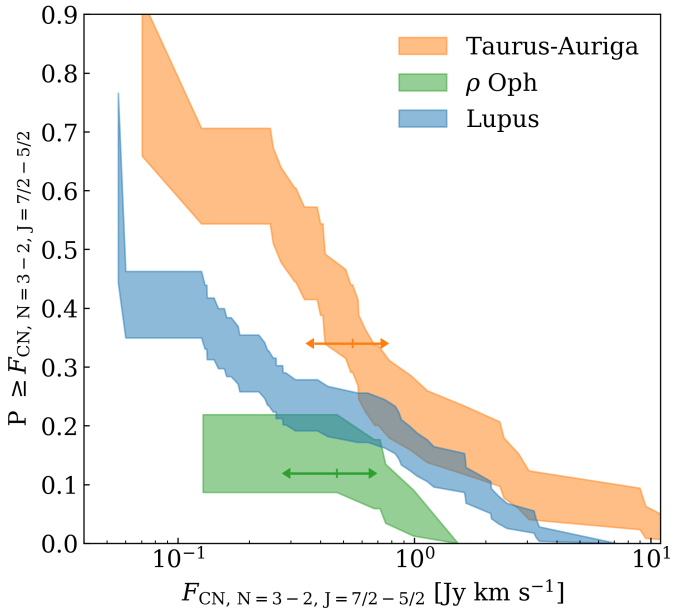

Figure 3.2: Disk-integrated CN $N = 3 - 2$, $J = 7/2 - 5/2$ fluxes in the complete Lupus disk survey (this work) compared to those of a sample of disks in Taurus-Auriga (Guilloteau et al. 2013) and ρ Oph (Reboussin et al. 2015). Source distances for all objects were taken from *Gaia* DR2, if available; otherwise, median distances to the three populations were used (Gaia Collaboration et al. 2018; Bailer-Jones et al. 2018). Fluxes were then scaled to the median distance of Lupus (160 pc). Colored arrows indicate the effect of using different CN ($N = 2 - 1$ $J = 5/2 - 3/2$) / ($N = 3 - 2$ $J = 7/2 - 5/2$) scaling parameters over the full range of model values.

Some caveats apply to this analysis. First, the IRAM 30-m sample covers a range of spectral types, stellar luminosities, and disk masses, but might be biased to bright or radially extended targets. Large-scale cloud contamination is a possibility, but is ruled out by the authors of both studies. Likewise, we must assume similar underlying stellar properties in all these samples. Fortunately, this assumption has already been found to hold for these regions (Ansdell et al. 2016; Cieza et al. 2018), and we do not expect this to have a significant

effect.

Second, previous CN observations have typically targeted the $N = 2-1$ lines. Specifically, both Guilloteau et al. (2013) and Reboussin et al. (2015) quote integrated fluxes for the $N = 2-1$, $J = 5/2-3/2$ components, which need to be related to the transition observed here. The CN ($N = 2-1,\ J = 5/2-3/2$) / ($N = 3-2,\ J = 7/2-5/2$)-ratio is partially dependent on the disk (temperature) structure. Based on the grid of models discussed in Cazzoletti et al. (2018), this ratio is found to vary between 1.1 and 2.1, depending on the disk flaring angle and scale height, but only weakly on mass. For IM Lup, a detailed model of the disk structure exists, based on both gas and dust observations (Cleeves et al. 2016). For this disk, with flaring angle $\psi = 0.15$ and scale height $h_c = 0.12$, we can infer a scaling ratio of 1.4, and an $N = 3-2,\ J = 7/2-5/2$ flux of 1.4 ± 0.1 Jy km s^{-1}.

Since such detailed models are not generally available, a single scaling factor was used here to obtain estimated CN $N = 3-2,\ J = 7/2-5/2$ fluxes from these surveys, assuming an intermediate value of 1.6. Where appropriate, the typical spread of values introduced by this assumption is indicated in the Figures by arrows to either side. It is important to note that – while some transition disks are included – these were not included in the models used to derive the flux ratios used here. However, transition disks with large inner cavities are rare enough (making up $\sim 11\%$ of the Lupus disks van der Marel et al. 2018a) that we do not expect this to significantly affect our results.

The results of three different CN surveys are shown in Figure 3.2. Using a logrank test (applicable to unbiased data with upper limits), we cannot identify a significant difference in the CN flux distribution between the disks in Lupus (this survey) and Taurus-Auriga (Guilloteau et al. 2013) ($p = 0.064$) if we use $p = 0.05$ as the rejection criterium, and the difference becomes significant only if we take an ($N = 2-1,\ J = 5/2-3/2$) / ($N = 3-2,\ J = 7/2-5/2$) flux ratio of 1.1. Taurus-Auriga seems to be relatively richer in intermediate-luminosity disks, which drive most of this trend. It is however possible that the disks sampled in the Guilloteau et al. (2013) survey are biased towards those disks in which both continuum and lines are more readily detected, leading to apparently brighter disks in CN. This seems to be the case for the ρ Ophiuchus sample; comparing it to the resolved ALMA images in Cieza et al. (2018) reveals a trend towards more radially extended disks, with only two objects included in the CN survey being unresolved. In Taurus-Auriga, such a bias would lead to the difference with Lupus becoming less significant, especially at lower CN luminosities. Comparing the Lupus CN results to those of the ρ Oph disk sample presented in Reboussin et al. (2015), however, the difference in flux distributions is always significant: ρ Oph has fainter overall CN emission, and a lower detection rate. A bias towards more radially extended disks in this region would make the lack of CN emission more significant, since we would expect such disks to be brighter rather than fainter on average (see Section 3.3.3, below).

3.3.3 CN models in the context of the Lupus population

The Lupus disk survey is uniquely suited to testing models of CN production in protoplanetary disks, both by looking at individual resolved objects and by comparing the full sample properties to the results from a large grid of models. In this section, this model grid is generated by the DALI physical-chemical disk code, which produces chemical abundances, performs non-local thermal equilibrium (LTE) excitation calculations, and produces ray-traced images. As mentioned, Cazzoletti et al. (2018) find several key results for CN emission in disks in their models made with this version of the code: first, an increasing integrated CN flux with increasing disk size; second, a strong dependence of flux on the UV radiation field

of stars; and third, a relatively weak dependence on total disk mass or volatile carbon abundance.

Here, a small DALI grid is used for comparison with our data, and the results of two previous surveys by Guilloteau et al. (2013) and Reboussin et al. (2015). Since both the Lupus data and the previous surveys give fine-structure fluxes, we used the collisional rates for CN from Lique et al. (2010), and raytrace the $N = 3-2,\ J = 7/2-5/2$ and $N = 2-1,\ J = 5/2-3/2$ lines. The grid is constructed using the standard viscous disk model of Lynden-Bell & Pringle (1974) as used, for example, in Andrews et al. (2011), and samples disks with critical radii R_c in the gas disk between 15 – 60 AU, and in the range $2\times10^{-6} - 9\times10^{-2}\ M_\odot$ in total disk mass. The stellar spectrum is given by a 4000-K black-body spectrum emitted by a star of $1.65\ R_\odot$; the grid includes models with UV excess (spanning two orders of magnitude in flux) as well as models without excess UV added to this stellar spectrum. The disk structure does not vary in these models: the surface density parameter $\gamma = 1$, while the scale height at 60 AU $h_c = 0.1$ and the flaring angle $\psi = 0.2$. While the CN flux is sensitive to these parameters, their effect is smaller than that of the varying UV luminosity used in these models (Cazzoletti et al. 2018), especially since the variation in flaring angles seems to be fairly small (Bustamante et al. 2015). Although our disks are not in hydrostatic equilibrium, the range of scale heights used here generally reproduces the observed SEDs of disks (van der Marel et al. 2016d).

In order to compare the models to the observational data, several assumptions must be made. First, a disk (gas) mass tracer is needed. Since ^{13}CO is not be a good tracer of the total gas mass, we will assume that the gas-to-dust ratio of these disks is 100 throughout, and that the dust is optically thin, leading to the same approximation used in Ansdell et al. (2016):

$$M_{disk} = 100\frac{F_{890\,\mu\mathrm{m}}d^2}{\kappa_\nu B_\nu(T_{\mathrm{dust}})}, \tag{3.1}$$

where the factor 100 comes from the gas-to-dust ratio (assumed to be constant and equal to the ISM value), $F_{890\,\mu\mathrm{m}}$ is the 890 μm flux, and d is the distance (typically around 160 pc, and taken from the *Gaia* DR2 results for the individual objects in the sample). The factor κ_ν is the grain opacity (assumed to be $10\,\mathrm{cm^2\,g^{-1}}$ at 1000 GHz with a power-law index of $\beta = 1$ (Beckwith et al. 1990)). The T_{dust} used here is 20 K.

The assumed initial abundances of carbon and oxygen are also potentially important, in the context of volatile carbon depletion found in protoplanetary disks (e.g., Bergin et al. 2013; Favre et al. 2013; McClure et al. 2016). However, for CN this is less relevant. For all disk models discussed here, the initial overall abundances are the same as those used in the default models of Cazzoletti et al. (2018), since the CN abundance was found not to be sensitive to the depletion of volatile C and O.

A final important assumption is the strength of the UV radiation field. As Cazzoletti et al. (2018) discuss, CN is very sensitive to the local abundance of excited molecular hydrogen H_2^*, which in turn is sensitive to FUV line pumping. However, typically, no UV spectra exist for these sources (excepting RU Lup and RY Lup Ardila et al. 2013; France et al. 2014; Arulanantham et al. 2018). We use a range of UV luminosities, where we focus on the 91.2 – 110 nm region. In that wavelength range, the UV luminosities sampled are between 1.5×10^{-4} and $1.5\times10^{-6}\ L_\odot$ for models with a UV excess, versus $2.3\times10^{-11}\ L_\odot$ for models with a purely stellar radiation field. Using a rough approximation, this UV field can be linked to the accretion rate onto the star. Following Kama et al. (2016b), the UV is produced from the accretion rate, the stellar mass, and a 10000 K black-body spectrum for the accreting material. Using this formulation an accretion rate of $10^{-8}\ M_\odot\ \mathrm{yr^{-1}}$ corresponds to a UV luminosity of $1.5\times10^{-6}\ L_\odot$, but as will be shown below, this may be uncertain by as much as an order of

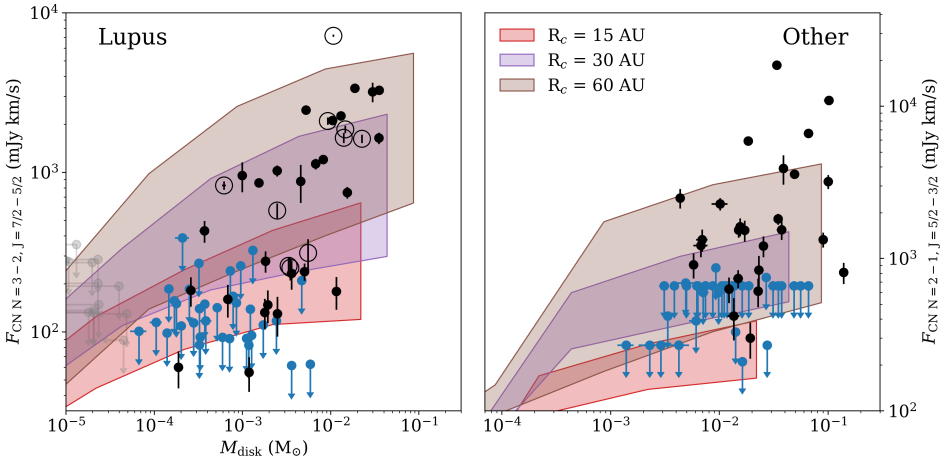

Figure 3.3: Disk-integrated CN flux vs. disk mass for the Lupus disk sample *(left panel)* and the previously observed disks in Taurus-Auriga and ρ Oph (Guilloteau et al. 2013; Reboussin et al. 2015) *(right panel)*. Detected sources are black, CN flux upper limits are blue, and double upper limits are gray. Colored regions indicate model results for the areas of parameter space covered by different UV fluxes and disk masses for a given R_c. Transition disks are marked with a circle and were not modeled. Fluxes for the Taurus-Auriga and ρ Oph sources and models are scaled to a 140 pc distance.

magnitude.

Linking CN to disk radii

In Figure 3.3, the model grid is overplotted to both the Lupus data and the previous large samples presented in Guilloteau et al. (2013) and Reboussin et al. (2015), after raytracing the appropriate transitions. The left panel shows the Lupus data and the corresponding CN $N = 3 - 2$ transition from the models; on the right panel the $N = 2 - 1$ transition fluxes are shown. In this comparison, no assumptions on the line ratios have to be made, since we directly compare to the model fluxes. The colored areas show models with different UV luminosities and disk masses at given R_c. From this figure, several conclusions can be drawn.

First, the large and unbiased disk population sampled in Lupus makes it apparent that for many of these disks the critical radius R_c must be small, even less than 15 AU, in order to reproduce the observed low CN fluxes. This result holds even when considering the impact of large variations in UV luminosity, and when considering variations in disk structure, as in Cazzoletti et al. (2018): the faintest detections and nondetections require compact gas disks. In the DALI models, the physical cause behind this strong effect is that, as the disk becomes more compact, the radius at which the CN emission would otherwise peak is located further out than the bulk of the disk material: the disk runs out before the CN can form in significant quantities.

Meanwhile, in line with Guilloteau & Dutrey (1998) and the model results in Cazzoletti et al. (2018), the brightest disks in CN clearly require large radii, and values of R_c larger than 60 AU, suggesting that the observed Taurus sample contains more massive, but also more radially extended sources than are found, on average, in Lupus.

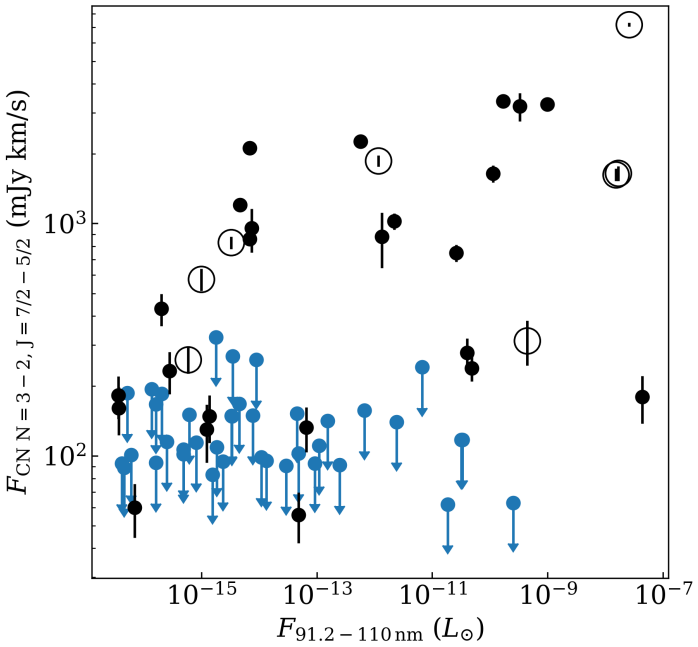

Figure 3.4: Disk-integrated CN fluxes vs. inferred UV fluxes between 91.2 and 110 nm from the combined stellar luminosity and the accretion rate onto the star (Alcalá et al. 2017). Circles indicate transition disks.

The observational determination of the R_c of a disk from resolved images is challenging, both for line- and continuum data. Even at high S/N, emission below the noise level may be missed. Moreover, gas- and continuum-derived outer radii for the same disk can differ: if a gas line is optically thick it may be detected further out than the dust (by a factor up to 3) (Facchini et al. 2017). The inward drift and growth of dust grains further change the appearance of the continuum, while leaving the gas unaffected. Both of these effects have been shown in the Lupus star forming region (Ansdell et al. 2018, Trapman et al. in prep.). While a population of unresolved or marginally resolved dust disks had previously been identified in the uniformly deep continuum survey, our CN models allow us to conclude that their underlying density structure also has a compact *gas* surface density distribution when compared to well-studied disks like IM Lup (which has an R_c of 60 AU) or TW Hya (R_c = 35 AU) (Cleeves et al. 2016; Huang et al. 2018).

CN as a UV tracer

The models run in Cazzoletti et al. (2018) and the grid used here both predict stronger CN emission from disks around stars that are more luminous in the UV, due to the sensitivity of the CN chemical network to the abundance of H_2^*. With the (known) stellar properties and accretion rates for the disk-bearing stars in Lupus, and the approximation for the UV excess

introduced above for the DALI models, we can calculate a 91.2 − 110 nm UV flux for each object in the sample. In Figure 3.4, these UV fluxes are compared to the observed CN flux. It is clear that, in contrast to the model predictions, no correlation exists between the CN flux and the UV flux estimated from the stellar flux and accretion rate, and this is confirmed by using a modified Kendall τ-test.

This apparently contradictory result, however, can be reconciled with the model predictions. The accretion rates used to infer the UV flux of these disks are accurate up to a factor of a few, being based on the Balmer continuum excess between ~ 320 and 346 nm and optical line emission (Alcalá et al. 2017). More importantly, while the total excess UV should be proportional to the accretion rate $\dot{M}_{\rm acc}$, it is not only emitted as continuum but also as line emission, which is more difficult to constrain (e.g., Herczeg et al. 2004; Bergin et al. 2004). In particular, the lines between 91.2 and 110 nm are relevant, since they may overlap with UV pumping lines for H_2 to create H_2^* via UV pumping. From previous studies of the UV lines of protoplanetary disks at these wavelengths, strong emission lines in this wavelength range have been shown to be present, and responsible for a significant fraction of UV radiation (e.g., Herczeg et al. 2005; Ardila et al. 2013; France et al. 2014).

One way to provide extra, independent information on the UV excess is to use the spatially resolved data, as opposed to the disk-integrated fluxes discussed here. This is because, as demonstrated in Figure 11 of Cazzoletti et al. (2018), the radial intensity profile of CN is also very sensitive to the UV radiation field. In the following, two disks for which CN is spatially resolved are discussed in greater detail.

3.4 CN images

3.4.1 Observations of Sz 98 and Sz 71

Table 3.1: Stellar properties of Sz 98 and Sz 71

	SpT	d [pc] (1)	$L_\star$ [$L_\odot$] (2)	$M_\star$ [$M_\odot$] (2)	$\log\left(\dot{M}_{\rm acc}\right)$ $M_\odot\,{\rm yr}^{-1}$ (2)
Sz 71	M1.5	155.89	0.33	0.42	-9.03
Sz 98	K7	156.22	1.53	0.74	-7.59

References. (1) Comerón (2008b); (2) Alcalá et al. (2017)

Table 3.2: Disk emission properties for Sz 71 and Sz 98.

	$F_{345\ \rm GHz}$ [mJy]	$F_{^{12}\rm CO\ 2-1}$ [Jy km s^{-1}]	$F_{^{13}\rm CO\ 3-2}$ [Jy km s^{-1}]	$F_{\rm CN\ 3-2}$ [Jy km s^{-1}]	PA^a [°]	i^a [°]
Sz 71	166.04 ± 0.63	2.86 ± 0.26^b	1.3 ± 0.1	2.35 ± 0.95	-37.5	47.0
Sz 98	237.29 ± 1.42	2.99 ± 0.22^b	0.51 ± 0.1	3.49 ± 0.13	107.4	-40.8

Notes. $^{(a)}$ Derived from the continuum data using the CASA *imfit*-task $^{(b)}$ Affected by foreground absorption and thus a lower limit.

The targets selected for detailed discussion in this Section, Sz 98 and Sz 71, are the second

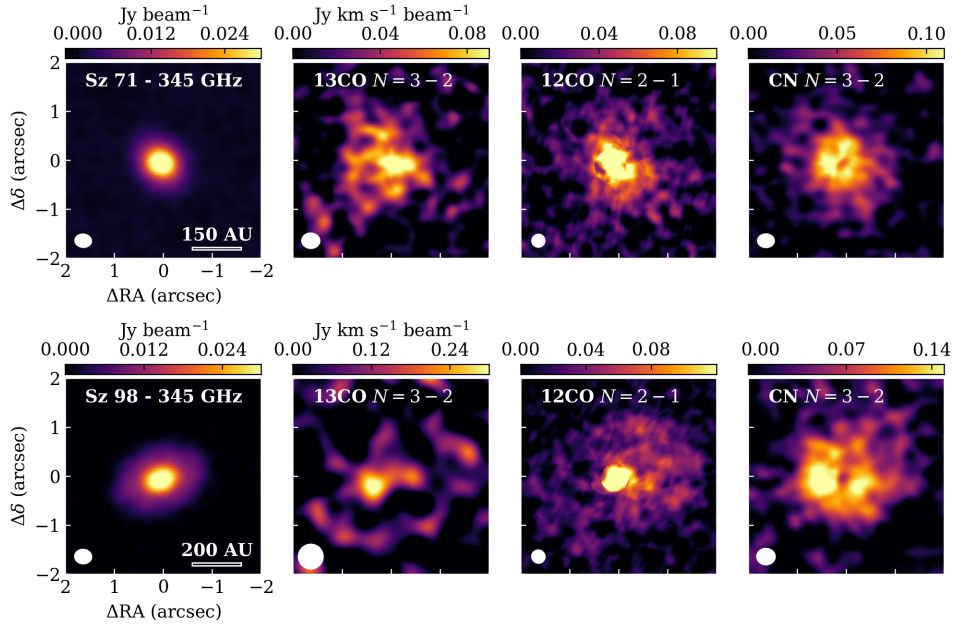

Figure 3.5: Continuum and moment-zero maps of ^{13}CO 3-2, ^{12}CO 2-1, and CN $N = 3 - 2$ (including only the brightest $J = 7/2 - 5/2$ transitions) for both sources.

and sixth brightest object in CN, respectively. These disks are particularly suited to modeling: their data have high S/N and show clear evidence of a ring-like emission morphology, as well as well-resolved emission. Based on their continuum emission, both disks have a favorable, relatively face-on inclination (45° for Sz 98, 36.5° for Sz 71). The stars do not cover the peak of the spectral type distribution in Lupus, which lies between M3 and M4: Sz 71 is an M1.5 star and Sz 98 is a K7 star.

Figure 3.5 presents the moment-zero maps as well as the disk continuum, showing CN and the bulk-gas tracers ^{13}CO $J = 3 - 2$ and ^{12}CO $J = 2 - 1$. In Figure 3.6, the radial intensity profiles of the continuum and CN line for both sources are shown. Both sources show CN rings, while Sz 98 shows evidence of significant but noncoincident continuum substructure. To improve the sensitivity of our analysis, these profiles have been made by azimuthally averaging over the (deprojected) moment-zero maps. In Figure 3.D.3 the spectra of these lines are shown; channel maps of the CN emission towards both sources can be found in Appendix 3.D. At the 3σ-level, C^{18}O is not detected towards either source. Table 3.2 shows the integrated fluxes for the lines discussed here, as well as the source position angles (PAs) and inclinations derived with the *imfit* task in CASA.

The other CN-bright sources are less suited for this purpose. A large fraction of the sources are too compact for structure in the CN emission to be apparent; 28% of the CN-detected sources are unresolved. Of the rest, many have low S/N levels, which make their detailed image-plane analysis impossible. Some of the brightest disks in CN are transition disks, which present a unique continuum structure with a large central cavity and are exposed to a different UV radiation field as a consequence. This may change the typical behavior of CN. Of the full disks, V1094 Sco is both radially extended and bright, both in continuum

and gas emission, but its CN line is partly resolved-out at the largest scales in low-velocity channels, and optically thick continuum emission in the inner disk may obscure the CN emission in those parts (van Terwisga et al. 2018a). For IM Lup, only Submillimeter Array (SMA) data for CN are available and at much lower resolution, and Sz 133 is edge-on.

CN 3-2

In both disks, CN 3-2 emission is ring-like, despite the relatively high noise levels of the final moment-zero maps. The peak emission is found at 40 and 60 AU for Sz 71 and Sz 98, respectively, although the emission does not completely vanish in the central region of the disk. The CN emission extends to large radii in both sources, and is clearly more extended than the continuum: in Sz 71, CN is detected out to approximately 200 AU, and in Sz 98 it can be seen out to 250 AU, while the continuum outer radii for both disks are 150 AU and 200 AU, respectively. The peak emission radius is further from the star in Sz 98 than in Sz 71. The latter source has the smallest contrast between emission at the disk center and peak intensity of these two sources.

In the moment-zero maps of CN, some asymmetry in the emission can be observed: this is likely due to the second-brightest hyperfine structure component ($J = 7/2 - 5/2$, $F = 5/2 - 3/2$) at $0.5\,\mathrm{km\,s^{-1}}$ from the targeted transition which is blended with the strongest hyperfine transition lines of $F = 9/2 - 7/2$ and $F = 7/2 - 5/2$, contaminating the emission redward of the primary hyperfine line. The theoretical relative intensity is expected to be up to 30% of the primary (Kastner et al. 2014; Hily-Blant et al. 2017). However, this does not appear to significantly impact the radial profile observed for the source, apart from some increase in noise in the most affected areas.

Another possible influence on the CN morphology is the existence of optically thick continuum, blanketing the lines. However, we can exclude this possibility: the observed brightness temperatures at the source center (where such an effect would be the most likely) of 6.0 K and 4.4 K for Sz 71 and Sz 98, respectively, are too low to be consistent with an optically thick continuum if an effective dust temperature of 20 K is assumed. This midplane temperature value is not unlikely given the relatively large beam size of our observations. Moreover, we do detect CO inside the CN rings in both sources, and unambiguously detect ^{13}CO in the CN hole location in Sz 71.

^{12}CO 2-1

^{12}CO is a bright and optically thick line in the atmospheres of protoplanetary disks, but it is strongly affected by absorption by foreground clouds towards both sources discussed here, at several separate velocity ranges. By inspecting the spectra in Figure 3.D.3, some cloud absorption appears to be present in the ^{12}CO line. This is consistent with single-dish observations of CO in the Lupus clouds (van Kempen et al. 2007). Cloud absorption should not have a similar effect on our CN data: the $N = 3 - 2$ transition has a much higher critical density (of $n_{\mathrm{crit}} \sim 6.0 \times 10^6$ cm^{-3}) than the low-density foreground cloud, and no evidence of cloud contamination of CN is found by Guilloteau et al. (2013) in Taurus.

Despite the absorption, there is sufficient signal to infer an outer radius for the ^{12}CO emission: the low-velocity channels blueward of the source velocity are not very absorbed. The outer radius at which CO is detected is larger than that of the CN emission radius towards both sources. Both Sz 98 and Sz 71 have detectable ^{12}CO out to about 250 AU, where the outer radius is limited by the S/N of our observations. Thus the gas extends at least a factor of

$\sim 2-3$ further than the continuum in both disks, which is typical for most Lupus disks (Ansdell et al. 2018).

^{13}CO 3-2

The ^{13}CO emission towards both sources is surprisingly faint and thus the maps suffer from low S/N (Ansdell et al. 2016; Miotello et al. 2017). Towards Sz 98, the detection of the line is marginal. Binning the data to 1 km s^{-1}-wide channels and lowering the resolution to 0.6″ by removing short baselines improves our sensitivity. The moment-zero map of ^{13}CO in this source does not show emission across the full disk, but only in 'lobes' towards the sides; this is probably caused by the low S/N of the data, as well as the limb-brightening effect of optically thin emission. In Sz 71, the emission is brighter and clearly centrally peaked, but also faint. Because of the low surface brightness of the line and the large S/N difference between the sources, we have not included ^{13}CO radial cuts in Figure 3.6.

The faintness of ^{13}CO in Sz 98 is especially surprising: it is one of the largest and brightest (in both ^{12}CO and continuum) disks in the Lupus sample, even including transition disks. Comparing the regions of the spectrum where ^{12}CO is absorbed to the ^{13}CO spectrum in Sz 71 (Figure 3.D.3, top) shows that foreground absorption is unlikely to be the full explanation for the faintness of the ^{13}CO line.

CN versus continuum

It is possible that, similar to the situation for CO (e.g., Isella et al. 2016; Fedele et al. 2017b), a link exists between continuum structure and the radial distribution of CN. Of the two disks discussed here, Sz 98 has the most obvious continuum feature: as shown in Figure 3.6, based on the u, v-plane fit in Appendix 3.B, a secondary maximum exists at the location of the 'bump' in the continuum at $\sim$ 120 AU. No counterpart of this feature is seen in the CN emission profile: CN peaks at a radius interior to it, and seems to present a fairly constant downward slope outside 100 AU.

For Sz 71, the continuum structure is less obvious: around 50 AU, the continuum profile begins to drop off less steeply. This is possibly related to an unresolved feature, but this is not clear even from the u, v-plane. The dashed line in Figure 3.6 for this object indicates the point where the turnover to a less steep profile occurs; it is fairly close to the CN peak.

Given the differences in the comparison between continuum and CN for these two sources, we therefore conclude that no obvious relation between the two is present in all cases. The clear presence of ring-like CN emission profiles in Sz 71 and Sz 98 is consistent with the predictions for rings of CN emission (Cazzoletti et al. 2018), and suggests that these features may be the result of chemistry alone, without the need for underlying continuum structures.

3.4.2 DALI modeling of CN rings

Here, a purely chemical cause for CN rings is investigated by more detailed modeling of the two bright, resolved disks discussed previously. The thermo-chemical disk modeling code DALI was used to test if simple models without the dust substructures identified in the previous subsection can produce radial distributions and integrated intensities of CN similar to those observed.

Based on the results of Cazzoletti et al. (2018), the presence of CN rings appears to be a common feature for their grid of protoplanetary disk models. Our goal is not to provide a perfect fit to the data, but rather to investigate whether rings similar (in terms of total flux

and radial profile) to those observed in these two disks can be produced without continuum substructure, and to isolate the main parameters governing CN emission strength and morphology. It is important in this context to note that in an absolute sense the uncertainties resulting from the assumptions in the chemical network alone, as well as from disk structure, lead to an uncertainty of a factor of a few in flux (Woitke et al. 2018).

Individual disk model details

In order to find a rough physical structure of the disk models, we first attempted to reproduce the objects' spectral energy distribution (SED), described in more detail in Appendix 3.C. This ensures that the large-scale distribution of the dust temperatures in the DALI models is similar to that of the source, and allows us to find, for instance, the CO snowline in the disks. Again, a parametric dust distribution model, as in Andrews et al. (2011), was used, constrained by data spanning a wide range of wavelengths between visible and mm-wavelengths. The gas surface density is 100× the dust surface density and is not decoupled. The disk structure parameters used for the models of both disks have not been varied further in their respective DALI models and can be found in Table 3.C.1. The outer radii of the disks were taken to be 200 AU, based on the CN data. The stellar parameters adopted for the input photosphere in the models were taken from Alcalá et al. (2014, 2017). As before, an initial estimate of the relevant UV flux for CN formation, $L_{912-1100\,\text{Å}}$, the UV excess emission from the model star was parametrized by the mass accretion rate, assuming 10000 K blackbody emission from the accreted material; due to the aforementioned uncertainties we have allowed for variations in the UV excess at these wavelengths of up to a factor 10.

A model of Sz 71 with a UV excess of $\log(L_{912-1100\,\text{Å}}/L_\odot) = -5.2$, based on the measured accretion rate, as well as a model with a significantly increased UV excess luminosity of $\log(L_{912-1100\,\text{Å}}/L_\odot) = -4.1$, denoted as M1 and M2, respectively, are presented in this section. For Sz 98, we only ran models with a single UV luminosity based on the observed accretion properties, and thus only have an M1, since this disk model already performed quite well in reproducing the CN flux and radial profile. The surface density profiles were kept fixed for all models of a single source. After ray-tracing each model, the images were convolved with a 0.3″ circular Gaussian beam, to see if the CN emission was similar to the observations.

Model results

As can be seen in Figure 3.7, the most remarkable feature of the CN emission, its concentration in a ring, is indeed reproduced in the model radial profiles, and occurs at radii within 20 AU of those seen in the data for Sz 71 model M2 and Sz 98 model M1. Also, the peak intensity of the emission is close (within 40%) to the observed peak value for the most similar models. The similarity in the emission profiles outside the peak is also encouraging, especially considering the uncertainty of a factor of a few in absolute fluxes from this type of chemical model.

Table 3.3 presents the total CN fluxes for the different models. The agreement is closest for Sz 98: the model flux and observed flux only differ by 5%. For Sz 71, if an increased UV luminosity is used, a larger difference can be seen, of $\sim$ 60% for all models; but the emission profile for M2 is clearly closer than that of model M1 for this disk, primarily due to the increase in peak intensity radius with increased UV flux.

No clear link appears between the CO snow-line position (defined as the location where the disk midplane reaches 20 K, following Öberg et al. 2005b) and the location of the CN peak in Sz 98. For Sz 71, the CO snow line, CN peak, and – possibly – the continuum slope

change lie within 10 AU, but the location of the snow line is quite uncertain, and both it and the continuum structure may not be closely related to the CN emission, which generally arises from the upper parts of the disk in models (Cazzoletti et al. 2018). In either case, the significant difference between the radii of the expected CO snow line position, the CN peak, and the continuum structure in Sz 98 seem to preclude a clear, one-to-one link between these quantities in all disks.

Table 3.3: Parameter values and integrated CN fluxes for the DALI models of Sz 71 and Sz 98; the most representative model is indicated in boldface.

		$\log(L_{912-1100\,\text{Å}}/L_\odot)$	F_{CN} [Jy km s^{-1}]
Sz 71	M1	-5.2	0.8
	M2	-4.1	3.9
	Obs		2.4
Sz 98	**M1**	-3.4	3.7
	Obs		3.5

CN rings as a disk probe

The main factor determining the CN radius and emission strength in these large-disk models is the excess UV flux due to accretion of material onto the star. This is especially obvious from comparing models M1 and M2 for Sz 71. It is crucial to note that in none of our models do we need the presence of substructure in the disks' surface density, either in the dust or gas components: CN rings arise purely from a chemical effect.

In the wider grid of disks in Cazzoletti et al. (2018), as well as in these models, CN rings are identified as a common feature. However, the ring radii and fluxes decrease with stellar T_{eff} and disk size, which explains why we can only study them in these two sources in the survey: below $R_c = 40$ AU, which applies to most of the objects in our sample, the ring radius drops rapidly and starts to become unresolved at our observations' effective resolution. At the same time, the flux and therefore S/N of the resolved CN images fall off. In the grid of models discussed in Section 3.3, the smallest CN peak radii would be resolved with an effective beam size of ~ 10 AU, given a face-on inclination and sufficiently good S/N.

Ultimately, CN is best used as a probe of the $91.2 - 110$ nm UV radiation field impacting the upper disk. This is especially the case if the other disk parameters, particularly the characteristic radius R_c, can be constrained independently. For this, other common molecular tracers like ^{12}CO or ^{13}CO can be used, leaving the way open for such studies in the future.

3.5 Conclusions

Our ALMA observations of a 99% complete sample of Class-II disks in Lupus allow us to study the behavior of CN, both in the full sample and – using individual models – in two resolved sources, and to use this common molecule as a probe of upper-disk atmosphere properties. With higher resolution and deeper observations, this molecule can be used to gain essential information on the properties of protoplanetary disks. The main results obtained from the observations discussed here are as follows:

- The CN $N = 3-2$, $J = 7/2-5/2$ transition is bright, and has a similar detection rate to ^{13}CO in disks in Lupus, but is not strongly correlated with either ^{13}CO or continuum fluxes in these disks.
- Comparing the CN flux distribution in Lupus to that of a population of Taurus-Auriga disks shows no significant difference, while disks in ρ Oph may be fainter on average.
- Comparing the CN fluxes of the full Lupus sample to a model grid with varying UV fluxes and gas disk characteristic radii, R_c , supports the conclusion that a significant number of disks in Lupus has a compact gas surface density profile, with $R_c \leq 15$ AU needed to explain part of the population.
- CN shows a ring-shaped emission morphology towards the bright, resolved sources Sz 71 and Sz 98, consistent with model predictions that CN is generally distributed in rings. For the bulk of objects, it is not possible to detect rings at this sensitivity and resolution, consistent with the expectations for compact, low-mass disks around late-type stars.
- Continuum substructure unrelated to the CN rings appears to be present in both sources, and particularly in Sz 98, where we infer an unresolved continuum ring at $\sim$ 120 AU. No connection between the CO snow line, the continuum structure, and the CN ring are seen in Sz 98.
- Disk models without substructure retrieve CN rings similar to those observed towards both sources, in terms of both peak emission radii and absolute intensities. Their radii are strongly dependent on the amount of excess UV emission, implying that CN rings are purely chemical in nature, and good tracers of the effective UV irradiation of the upper disk atmosphere, especially if gas disk sizes are determined from other data.

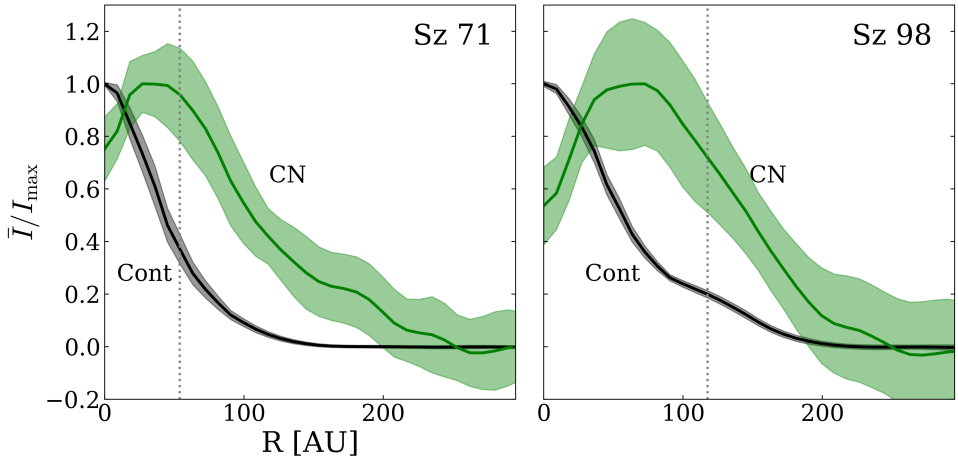

Figure 3.6: Radial cuts of the continuum (black) and CN moment-zero (green) maps for both sources, normalised to the peak radially averaged intensity, after deprojecting and derotating the image-plane data. The shaded regions indicate the 1σ noise level. The gray dotted line indicates the location of a local maximum in the continuum due to an (unresolved) dust ring in Sz 98, and the location of continuum knee in Sz 71 (see Appendix 3.B).

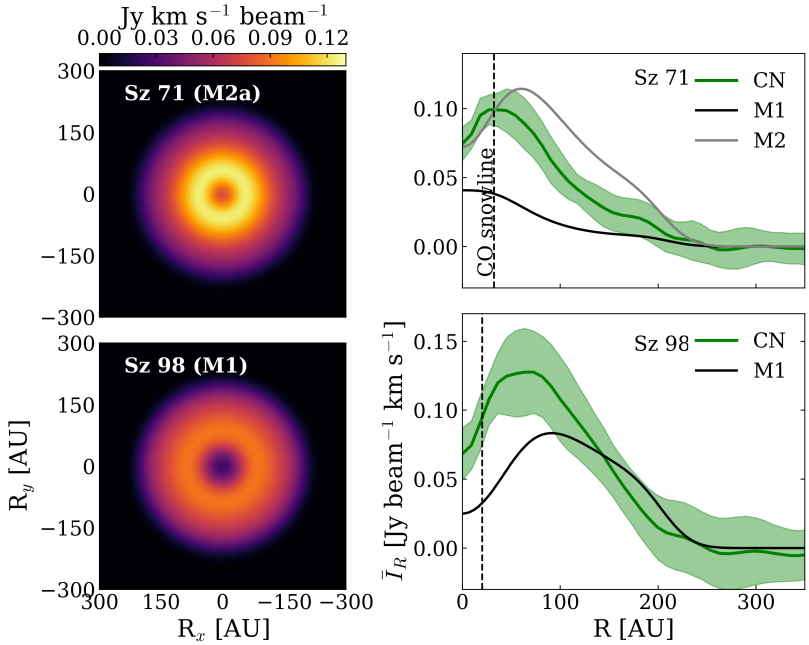

Figure 3.7: CN model images and radial intensity profiles (black and gray) from the DALI models, after convolving with a 0.″3 beam for both sources. Model M2 for Sz 71 has an increased UV luminosity relative to M1. The black dashed vertical lines indicate (approximately) the CO snow line locations in the models. The observed radial profiles of CN are shown in green, together with their 1σ errors.

Appendix

3.A CN versus C^{18}O in Lupus disks

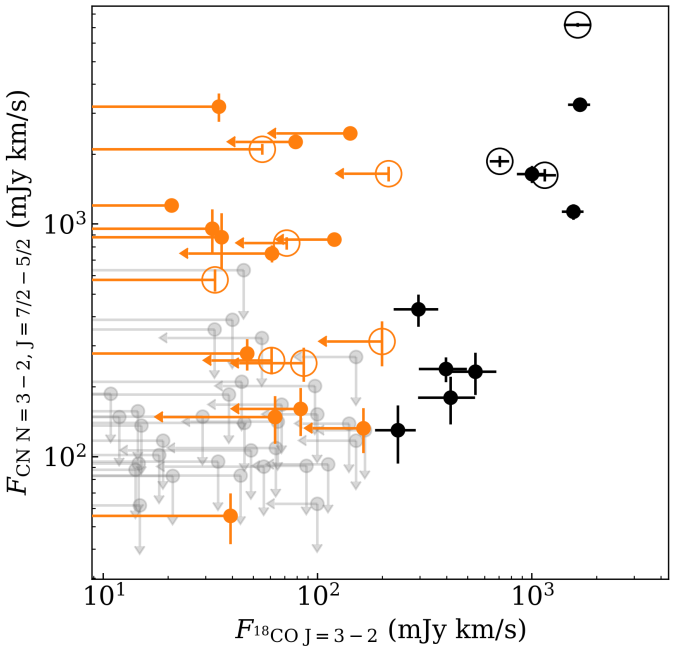

Figure 3.A.1: Integrated CN vs. C^{18}O 3 – 2 fluxes for the Lupus disk sample. Detected sources are black, C^{18}O 3 – 2 upper limits are orange, CN flux upper limits are blue, and double upper limits are gray. Transition disks are marked with a circle.

3.B u, v-plane analysis

It is possible that, in the disks in which a clear CN ring is present, some underlying continuum structure is responsible, for instance, by causing a local density enhancement. Therefore, it is relevant to first establish if any such structures are present in the disks we study in detail, and if so, where they are located.

In the two disks discussed here, based on their continuum intensity profile (Fig. 3.6), Sz 98 seems to have a bright central core, with a large, fainter outer region, giving it something of a 'fried-egg'-appearance similar to V1094 Sco (van Terwisga et al. 2018a); the radial profile seems to suggest an unresolved structure in this outer region. Sz 71, on the other hand, may have a 'knee' in its intensity profile at around 50 AU. Analyzing the continuum emission in the u,v-plane can provide a more thorough picture of the mm-dust structure underlying the CN emission, even if such features are difficult to detect in the image plane due to the deconvolution algorithm. Tazzari et al. (2017) performed a fit of both disks with a smooth self-similar disk model, including radiative transfer. However, such a smooth model is not

expected to be able to fit radial substructures in the continuum, if any are present. For that reason, a simpler fitting method is used here, focusing only on reproducing the radial intensity profile.

Both sources were deprojected and derotated based on an image-plane fit with the CASA imfit-task. We confirmed that, within the uncertainties given by these values, the results of our analysis did not significantly change. Subsequently the data were binned to 15 kλ bins in u,v space, and finally scaled and fit with two simple models: a Gaussian core (Model 1), the single-component model, and a Gaussian core modulated with a cosinusoidal term (Model 2), the two-component model, to mimic the behavior of an unresolved ring of particles. This method was successfully used by Zhang et al. (2016) to describe rings in a variety of transitional and full disks, and has the important property that it uses a minimal number of parameters, while being smooth (making it similar to these disks' appearance) and not necessarily containing nulls (which must occur for sharp-edged models).

$$I(\theta) = \frac{1}{\sqrt{2\pi}\sigma_0} \exp\left(-\frac{\theta^2}{2\sigma_0^2}\right) + \sum_j \cos(2\pi\theta\rho_j) \times \frac{a_j}{\sqrt{2\pi}\sigma_j} \exp\left(-\frac{\theta^2}{2\sigma_j^2}\right). \tag{3.2}$$

Here, a_j is the relative intensity of the jth component, σ_j its width (converted, for ease of reading, to AU in Table 3.B.1), ρ_j is the spatial frequency which modulates the jth Gaussian, and θ is the angle to the source center (in radians). Baselines up to 800 kλ are used for our fit to Sz 71, and up to 500 kλ for Sz 98; beyond these values, noise starts dominating our u,v-plane data. Parameter values for two models, with $j_{\max} = 0$ and $j_{\max} = 1$, were obtained from MCMC-fits to the observations with the *PyMC* Python module.

In Figure 3.B.1 and Table 3.B.1, the results of the fitting procedure are shown. For both Sz 71 and Sz 98, the two-component Gaussian model fits the continuum significantly better than the single-component one, when comparing the Bayesian Information Criterion (BIC) (Schwarz 1978): $\Delta_{\mathrm{BIC}} = 1296.9$ for Sz 71, and for Sz98, $\Delta_{\mathrm{BIC}} = 1382.7$ in favor of the two-component model. The two-component model performs especially well at large baselines, suggesting that there is continuum structure at small spatial scales. For Sz 98, a true second maximum is immediately obvious in the visibility plane. The similarity of this feature to those seen (at much higher resolutions and sensitivities) in, for example, Zhang et al. (2016), ALMA Partnership et al. (2015), and Andrews et al. (2016a), is remarkable, all the more so considering its amplitude – not much fainter than the structures identified in the V1094 Sco disk (van Terwisga et al. 2018a). For Sz 71 the best-fit values of ρ_1 show a fairly large uncertainty, and the amplitude of the small-scale signal is not very large.

In Sz 98, we can assign the identified u,v-plane feature to the presence of an (unresolved) ring in the image plane, located at 117 AU, depicted with a dotted gray line in Figure 3.6 (right); this is consistent with the knee that is tentatively identified in the continuum radial intensity profile. Moreover, Tazzari et al. (2017) find a clear ring-like residual when comparing their best-fit model of Sz 98 to the data, located in the same part of the disk. The visibility feature in Sz 71 is weaker and overlaps with the bright 'core' of the disk; thus, without higher-resolution and deeper data, we can only say that its brightness profile drops off less steeply beyond 50 AU in this disk (Figure 3.6 (left)). Given the similarity of these disks' visibilities, it is possible that a structure similar to that of Sz 98 is present in Sz 71, but at a fainter level and closer to the central star. However, no ring-like residual is present

for this disk in the best-fit smooth disk model by Tazzari et al. (2017). It is also important to note that our intensity profiles do not provide any information on the vertical structure of the continuum, since the mm-sized grains responsible for the emission modeled here are expected to be vertically settled with respect to the disk gas (Dullemond & Dominik 2005; Pinte et al. 2016).

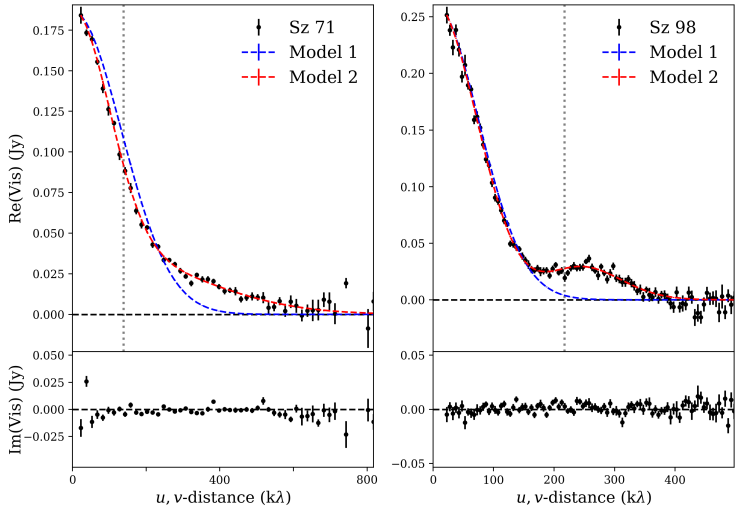

Figure 3.B.1: 345 GHz continuum visibilities for Sz 71 and Sz 98, after deprojection and derotation. The real visibilities have been overplotted with the best fitted single-component model (Model 1, blue) and the best-fit two-component model (Model 2, red). The best-fit spatial frequency of the two-component model is indicated by the gray dashed lines.

Table 3.B.1: Parameter values and inferred errors from the MCMC fit for both models and sources.

		σ_0 [AU]	a_1 [Jy beam^{-1}]	σ_1 [AU]	ρ_1 [kλ]	χ^2_ν	BIC
Sz 71	Model 1	37.1 ± 0.18	-	-	-	27.87	1071.2
	Model 2	49.8 ± 0.80	0.969 ± 0.055	19.9 ± 1.7	138 ± 23	1.71	-225.7
Sz 98	Model 1	87.7 ± 0.40	-	-	-	20.67	1306.8
	Model 2	85.3 ± 0.71	0.467 ± 0.11	91.0 ± 3.0	217.0 ± 2.1	1.45	-75.9

3.C SED fitting procedure

We attempted to closely reproduce the SEDs of both sources with our models, in order to find a dust density and temperature structure corresponding as closely as possible to the real (disk-averaged) properties of the disks, especially at mid-infrared down to mm wavelengths. Using the resulting parametrized disks as input for the DALI physical-chemical modeling code allows us to confirm if the CN rings we observe in the sources are simply the result of the global properties of the disk (particularly, the interplay between gas density and UV

radiation) or if they require underlying dust and/or gas substructures at the radius of the CN ring (neither of which would be revealed by the SED).

The disk model used is adapted from the model used in Andrews et al. (2011), but without an exponential taper at characteristic radius R_c. Instead, the disk is truncated at $R_c = R_{\rm out}$, and the surface density slope is fixed at $\gamma = 1$ for all models. The parameter space of this model was explored in two phases. For the first phase, we used the RADMC3D-code[1] to globally constrain the flaring angle of the disk ψ, its scale height h_r, the disk mass M_d, and the possibility of an inner cavity ($R_{\rm in} \geq R_{\rm sub,silicate}$).

Taking $R_{\rm in}$ as a variable was motivated by our difficulty reproducing the near- and mid-IR parts of the SED when using the standard parametrization of $R_{\rm sub,silicate}$. However, we only take values of $R_{\rm in}$ in a small interval, as radii beyond $\sim$ 2 AU would lead to obviously different SEDs. The shape of the near- and mid-IR SED is also sensitive to the choice of parametrization of the inner region structure: a puffed-up inner rim extending to the sublimation radius, for instance, could lead to a similar SED. However, such changes would make a significant difference only at scales much smaller than our ALMA observations' resolution.

The values of $R_{\rm out}$ and i in our models are taken from the 870 μm CN and continuum images, respectively. For both disks, we take $R_{\rm out}$ to be $\sim$ 200 AU. We use a single grain population between 0.5 and 1000 μm. Our opacities are based on the same abundances of amorphous and crystalline silicate and amorphous carbon grains as in Weingartner & Draine (2001).

The second phase - performed in DALI - uses the best-fit values from the RADMC3D models, but includes a population of small grains and settled large grains. The fraction of large grains, here, is f, and the decreased scale height of the settled large grain population is equal to χh_r. We explore only $f = [0.85, 0.99]$ and $\chi = [0.2, 1.0]$. Our small grain population is limited to a maximum size of 1 μm. Including this small grain population means we have a better description of the silicate features in the NIR (especially for Sz 71, for which we have an IRS spectrum). Using DALI also allows us to make sure no gridding inconsistencies are present when we run the full thermo-chemical code to calculate the CN emission.

For the stellar luminosity, effective temperatures, and accretion luminosities we used the values given in Table 3.1. We corrected the data for extinction using $R_V = 3.1$, and $A_V = 0.5$ mag and 1.0 mag for Sz 71 and Sz 98, respectively (Alcalá et al. 2017). In the case of Sz 71, the X-shooter spectra have been rescaled by a factor of 1.5 (within the instrument's systematic error; see e.g., Alcalá et al. (2014)) to agree with the 2MASS J, H, K-magnitudes. For Sz 98, we show the 2MASS and B and V-band photometry, but do not include them in our fit. This source is a known variable, and the X-shooter data have the largest amount of wavelength coverage in a single observation. Moreover, the most accurate determination of $T_{\rm eff}$ and $L_\star$ is based on these data.

3.C.1 SED data

The SEDs of the disks were constructed on the basis of available literature data. For Sz 98, the dataset consists of data from the X-Shooter (from Alcalá et al. (2017)), WISE, and the Herschel PACS and SPIRE instruments (Bustamante et al. 2015), as well as 2MASS J, H, K and B and V-band fluxes (Cutri et al. 2003). The PACS data, however, were not used in the fit since they appear to be affected by a systematic offset possibly caused by the photometric calibration.

[1] http://www.ita.uni-heidelberg.de/~dullemond/software/radmc-3d/

Sz 71 has not been observed by Herschel, and the behavior of its SED is therefore much less constrained at far-IR wavelengths. However, B, V, R-band and X-Shooter (from Alcalá et al. (2014)) and 2MASS data do exist, as well as a Spitzer IRS spectrum between 10 and 36 μm (Lebouteiller et al. 2015). The Sz 71 SED appears to be showing a significant contribution from amorphous carbonaceous grains, in the form of excess emission at wavelengths down to 1 micron. These opacities are not included in our models. However, since their primary effect is to heat the innermost part of the disk (outside our chemical region of interest) we do not expect to seriously underestimate the CN emission by excluding them in our full thermo-chemical models.

3.C.2 SED fitting results

Both disks appear to be nonflaring compared to, for example, the sample presented in van der Marel et al. (2016e) when fit with a similar methodology and disk model. This is significant, since the flaring angle has a large impact on the dust heating at radii where we expect CN to be present (Cazzoletti et al. 2018). However, there is still a significant difference between both disks' flaring angles, meaning our results are still representative of disks in general with a variety of flaring angles.

Table 3.C.1: Parameter ranges and used values for the disk models

Sz 71

Parameter	minimum	maximum	used
h_r	0.07	0.15	0.11
ψ	0.1	0.3	0.14
f	0.85	0.99	0.99
χ	0.2	1.0	0.2
$R_{\rm in}$ (AU)	0.04	1.5	1.0
M_d ($M_\odot$)	0.01	0.09	0.03

Sz 98

Parameter	min	max	best
h_r	0.07	0.15	0.1
ψ	0.07	0.1	0.085
f	0.85	0.99	0.99
χ	0.2	1.0	0.2
$R_{\rm in}$ (AU)	0.06	1.5	0.5
M_d ($M_\odot$)	0.01	0.09	0.07

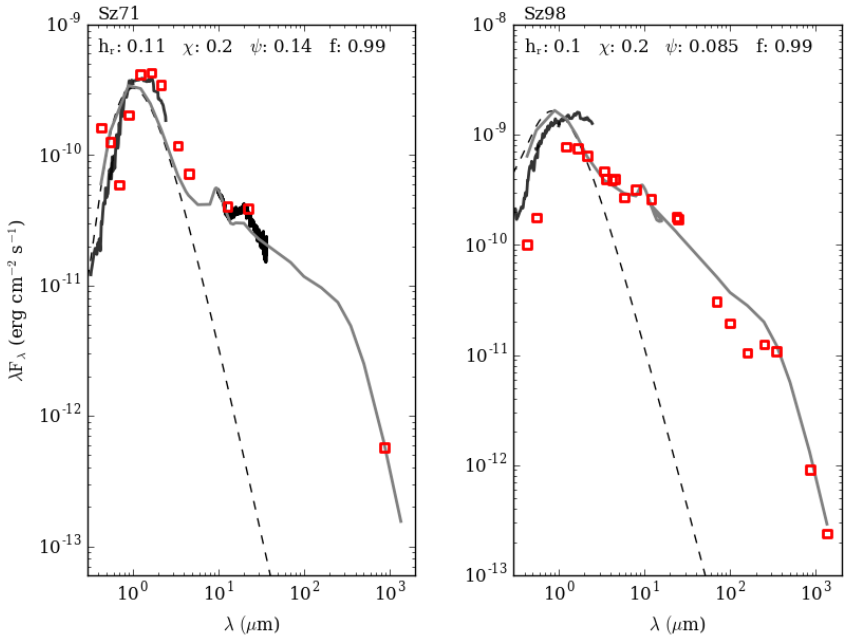

Figure 3.C.1: DALI SEDs and model parameters for the fiducial disk models. The preferred model is in gray, X-Shooter and IRS spectra are solid black lines, broadband continuum data are open red symbols, and the black dashed lines the input stellar photospheres.

3.D CN channel maps and emission line spectra for two bright, resolved sources

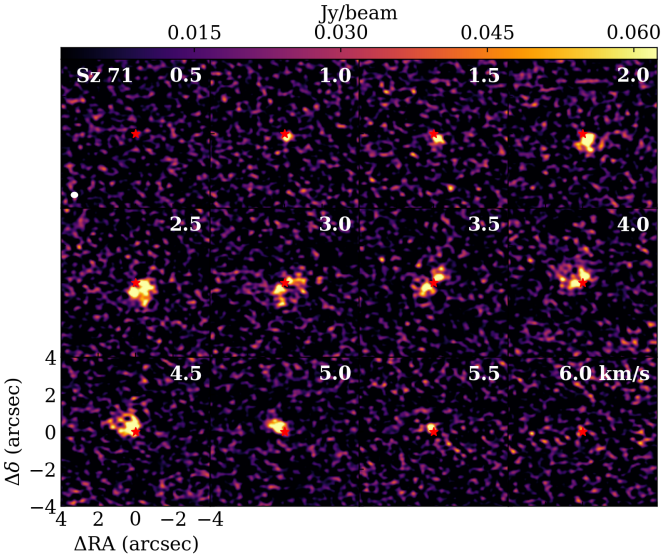

Figure 3.D.1: Channel map showing CN emission towards Sz 71, and relatively faint line wings indicative of an emission ring. The source location is marked with a red star; the contours are at the 3σ and 5σ levels.

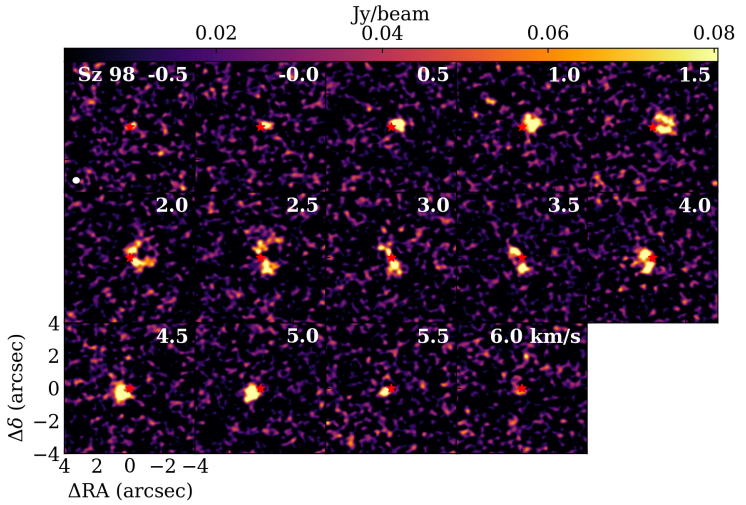

Figure 3.D.2: Channel map showing CN emission towards Sz 98, and relatively faint line wings indicative of an emission ring. The source location is marked with a red star; the contours are at the 3σ and 5σ levels.

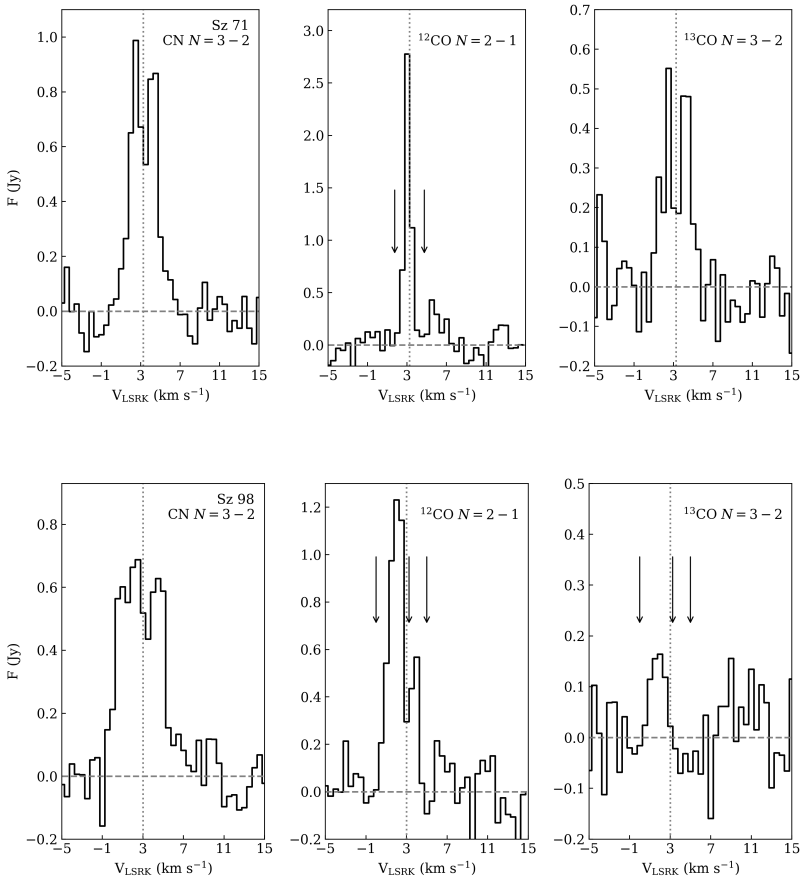

Figure 3.D.3: Spectra of CN (focusing on the brightest $N = 3 - 2$, $J = 7/2 - 5/2$ components) and the main CO isotopologs for Sz 71 (top) and Sz 98 (bottom). Arrows show the velocities of foreground cloud material (partially) absorbing the ^{12}CO line. Vertical dotted lines indicate the source velocity. The scale of the y-axis varies between panels. All spectra were extracted in an aperture overlapping with the detection in the moment-zero map (for ^{12}CO), or in a 2″ aperture on the source location (for CN and ^{13}CO).

3.E CN fluxes and upper limits for the Lupus sample

Table 3.E.1: CN $N = 3 - 2$, $J = 7/2 - 5/2$ fluxes, errors, and apertures

Source	$F_{\mathrm{CN\,N=3-2}}$ [Jy km s^{-1}]	$E_{\mathrm{CN\,N=3-2}}$ [Jy km s^{-1}]	Aperture [arcsec]
Sz 65	250	31	0.58
Sz 66	57	14	0.29

Table 3.E.1: continued.

Source	$F_{\mathrm{CN\,N=3-2}}$ [Jy km s^{-1}]	$E_{\mathrm{CN\,N=3-2}}$ [Jy km s^{-1}]	Aperture [arcsec]
J15430131-3409153	< 635	...	0.35
J15430227-3444059	< 133	...	0.35
J15445789-3423392	< 180	...	0.35
J15450634-3417378	< 139	...	0.35
J15450887-3417333	245	51	0.58
Sz 68	191	44	0.58
Sz 69	< 344	...	0.35
Sz 71	2353	95	1.45
Sz 72	< 95	...	0.35
Sz 73	< 121	...	0.35
Sz 74	< 111	...	0.35
Sz 75	< 69	...	0.35
Sz 76	949	202	1.62
Sz 77	< 124	...	0.35
Sz 81A	< 166	...	0.35
J15560210-3655282	890	238	1.16
IM Lup [2]	3289	130	
Sz 83	1630	135	1.45
Sz 84	626	68	1.16
Sz 129	724	61	1.16
J15592523-4235066	< 109	...	0.35
RY Lup	1624	100	1.16
J16000060-4221567	< 106	...	0.35
J16000236-4222145	1983	114	2.03
J16002612-4153553	< 108	...	0.35
Sz 130	< 140	...	0.35
MY Lup	1700	123	1.45
Sz 131	< 89	...	0.35
J16011549-4152351	1131	86	1.16
EX Lup	< 63	...	0.35
Sz 133	2655	112	1.16
Sz 88A	< 243	...	0.35
Sz 88B	< 95	...	0.35
J16070384-3911113	430	67	1.16
J16070854-3914075	1719	91	1.16
Sz 90	273	42	0.58
Sz 91	...	...	
J16073773-3921388	50	13	0.29
Sz 95	< 94	...	0.35
J16075475-3915446	< 388	...	0.35
J16080017-3902595	< 183	...	0.35
J16080175-3912316	< 202	...	0.35
Sz 96	< 145	...	0.35

[2] CN $N = 2 - 1$, $J = 5/2 - 3/2$ flux scaled to the CN $N = 3 - 2$, $J = 7/2 - 5/2$ transition.

Table 3.E.1: continued.

Source	$F_{\mathrm{CN\,N=3-2}}$ [Jy km s^{-1}]	$E_{\mathrm{CN\,N=3-2}}$ [Jy km s^{-1}]	Aperture [arcsec]
J16081497-3857145	160	37	0.58
Sz 97	< 152	...	0.35
Sz 98	3494	131	1.74
Sz 99	< 149	...	0.35
Sz 100	350	45	0.87
J160828.1-391310	< 235	...	0.35
Sz 102	< 83	...	0.35
Sz 103	< 258	...	0.35
J16083070-3828268	7467	134	2.03
Sz 104	< 105	...	0.35
J160831.1-385600	< 132	...	0.35
V856 Sco	< 205	...	0.35
V1094 Sco [3]	3430	475	5.34
Sz 106	< 152	...	0.35
Sz 108B	115	32	0.58
J16084940-3905393	< 98	...	0.35
V1192 Sco	< 112	...	0.35
Sz 110	< 95	...	0.35
J16085324-3914401	119	26	0.46
J16085373-3914367	182	38	0.58
Sz 111	1881	106	2.03
J16085529-3848481	< 190	...	0.35
Sz 112	< 82	...	0.35
Sz 113	140	33	0.58
J16085828-3907355	< 353	...	0.35
J16085834-3907491	< 126	...	0.35
J16090141-3925119	805	47	0.87
Sz 114	1158	55	1.16
Sz 115	< 150	...	0.35
J16091644-3904438	< 272	...	0.35
J16092032-3904015	< 277	...	0.35
J16092317-3904074	< 136	...	0.35
J16092697-3836269	< 268	...	0.35
J160934.2-391513	< 135	...	0.35
J16093928-3904316	< 281	...	0.35
Sz 117	< 153	...	0.35
Sz 118	295	65	0.87
J16095628-3859518	< 95	...	0.35
J16100133-3906449	< 132	...	0.35
J16101307-3846165	< 106	...	0.35
J16101857-3836125	< 107	...	0.35
J16101984-3836065	< 89	...	0.35
J16102741-3902299	< 130	...	0.35

[3] Partly resolved-out and continuum-shielded

Table 3.E.1: continued.

Source	$F_{\mathrm{CN\,N=3-2}}$ [Jy km s^{-1}]	$E_{\mathrm{CN\,N=3-2}}$ [Jy km s^{-1}]	Aperture [arcsec]
J16102955-3922144	787	48	0.87
Sz 123B	< 102	...	0.35
Sz 123A	241	41	0.64
J16115979-3823383	< 95	...	0.35
J16120445-3809589	< 219	...	0.35
J16124373-3815031	1015	82	0.99
J16134410-3736462	< 149	...	0.35

4

Disk masses in the Orion Molecular Cloud-2: distinguishing time and environment

S.E. van Terwisga, A. Hacar, and E.F. van Dishoeck.
2019, A&A, 628, 85

Abstract

The mass evolution of protoplanetary disks is driven by internal processes and by external factors such as photoevaporation. Disentangling these two effects, however, remains difficult.

Aims: We measured the dust masses of a sample of 132 disks in the Orion Molecular Cloud 2 (OMC-2) region, and compared them to externally photoevaporated disks in the Trapezium cluster, and to disks in nearby low-mass star-forming regions (SFRs). This allowed us to test whether initial disk properties are the same in high- and low-mass SFRs, and enabled a direct measurement of the effect of external photoevaporation on disks.

Methods: A $\sim 20' \times 4'$ mosaic of 3 mm continuum observations from the Atacama Large Millimeter/submillimeter Array (ALMA) was used to measure the fluxes of 132 disks and 35 protostars > 0.5 pc away from the Trapezium. We identify and characterize a sample of 34 point sources not included in the *Spitzer* catalog on which the sample is based.

Results: Of the disks, 37 (28%) are detected, and have masses ranging from $7 - 270\,M_\oplus$. The detection rate for protostars is higher (69%). Disks near the Trapezium are found to be less massive by a factor $0.18^{+0.18}_{-0.11}$, implying a mass loss rate of $8 \times 10^{-8}\,M_\odot\,\mathrm{yr}^{-1}$.

Conclusions: Our observations allow us to distinguish the impact of time and environment on disk evolution in a single SFR. The disk mass distribution in OMC-2 is statistically indistinguishable from that in nearby low-mass SFRs like Lupus and Taurus. We conclude that age is the main factor that determines the evolution of these disks. This result is robust with respect to assumptions of dust temperature, sample incompleteness, and biases. The difference between the OMC-2 and Trapezium cluster samples is consistent with mass loss driven by far-ultraviolet radiation near the Trapezium. Taken together, this implies that in isolation disk formation and evolution proceed similarly, regardless of cloud mass.

4.1 Introduction

Protoplanetary disks are the environments in which planetary systems take shape; planets migrate, accrete mass in various parts of the disk, and in turn they can affect the disk itself, for instance by carving out gaps or rings. Throughout these processes, the total mass of the material in the disk is a key parameter. It sets the amount of material left to accrete into planetesimals; it also plays a role in determining the temperature profile of the disk (for a given surface density profile); likewise, the surface density at a given radius determines how rapidly a planet will migrate (Benz et al. 2014; Baruteau et al. 2014). How the masses of protoplanetary disks evolve, and are affected by environmental factors, is therefore a fundamental question to answer in order to understand planet origins.

In recent years, the Atacama Large Millimeter/submillimeter Array (ALMA) and Submillimeter Array (SMA) telescopes, with their excellent sensitivities, have been essential in revealing the mass distributions of cold dust in large samples of protoplanetary disks in nearby star-forming regions (SFRs). Thanks to the presence of very complete and deep censuses of disk host stars, made primarily with *Spitzer*, these surveys are also unbiased, reaching warm dust masses as low as 0.1 lunar mass (Evans et al. 2003). This completeness makes it possible to compare the disk mass distribution across regions.

Surveys today span a wide range of physical conditions and ages, with the σ Ori (Ansdell et al. 2017) and Orion Nebula Cluster (ONC) or Trapezium cluster (e.g., Eisner et al. 2008; Mann & Williams 2010) typical of massive, young SFRs. Regions like Lupus, Taurus, and Chamaeleon I on the other hand probe a lower mass, more isolated regime of star formation, at ages between 1 and 5 Myr (Ansdell et al. 2016; Andrews et al. 2013; Pascucci et al. 2016). Observations of the Upper Scorpius OB association (Upper Sco), meanwhile, provide a window on a more evolved population (Barenfeld et al. 2016).

From the comparison of the disk masses presented in these surveys, two results become apparent. First, in low-mass star-forming regions where stars and their disks form and evolve in relative isolation, the disk mass distributions of regions of similar ages are essentially indistinguishable. For example, Taurus and Lupus disks are statistically the same in terms of dust mass distribution (Ansdell et al. 2016). With age, a steep decline (a factor of ~ 3) in the median disk mass is seen, although some massive disks persist up to 10 Myr in Upper Sco (Barenfeld et al. 2016).

However, in the dense environment of the ONC and in σ Ori, the presence of young massive stars can have a dramatic effect. Even a young population ($\sim 1-3$ Myr) like the ONC has disks that are significantly less massive than their counterparts in Lupus (Eisner et al. 2018). Also, disk mass decreases in the vicinity of the Trapezium cluster (Mann et al. 2014) and σ Ori (Ansdell et al. 2017). These results, as well as observations of proplyd structures in the inner ONC (e.g., O'Dell et al. 1993; O'Dell 1998), have led to the conclusion that externally driven photoevaporation is the main cause of the extra mass loss in these objects.

The purpose of the survey presented in this article is to characterize the bulk dust mass contained in cold, millimeter-sized grains in a population of disks around young stars centered on the Orion Molecular Cloud 2 (OMC-2) region in the Orion A cloud, away from the strong UV radiation near the Trapezium (Peterson & Megeath 2008). This is done using observations from the Atacama Large Millimeter/submillimeter Array (ALMA).

Environments like the Orion nebula play an important role in our understanding of planet formation because they are such common sites of star formation, with up to half the stars in the Galaxy forming in similar high-mass SFRs (Lada et al. 1993; Carpenter 2000, e.g.,), likely including the Sun (Williams & Gaidos 2007). Although the disk population in the

densest parts of Orion is now well studied, the properties of disks in the outer regions are in comparison much less well constrained. For instance in Mann & Williams (2010) and Mann et al. (2014), disks out to 2 pc from the Trapezium are sampled, and reveal a clear decrease of disk mass with proximity to the ONC, but the population beyond 0.5 pc is sampled with fewer than ten disks.

Megeath et al. (2012) used *Spitzer* observations to show a significant population of disks with warm dust extending far beyond the ONC, and running along the Integral-Shaped Filament (ISF). The disks in OMC-2 offer a unique view of the properties of disks in a massive star-forming region: here, bright young O-type stars are absent, leading to a much lower interstellar radiation field, which approaches the conditions in low-mass star-forming regions. This allows us to constrain, for the first time, a population of disks unaffected by external photoevaporation, but still in relatively close proximity to the Trapezium cluster. By comparing disk properties between this sample and, for example, the Lupus population, it is possible to gain insight into the initial conditions of disk formation in a massive cloud.

The large mosaic of ALMA 12m data of the OMC-1 and OMC-2 regions that form the northern part of the ISF, presented in Hacar et al. (2018), is a uniquely valuable resource in this context. Inside 0.5 pc from the Trapezium, heavy contamination from continuum emission that has been partially resolved out and from free-free emission is present. However, these observations cover a large area containing the population of interest for this study, which is located 0.5 pc beyond the Trapezium. *Spitzer* data of this region allow us to extract disk properties in a homogeneous and unbiased manner.

In this article, we present the first large ($N = 132$) blind unbiased survey of disks in OMC-2, centered on the ISF, and use this sample to infer the rate of mass loss in the vicinity of the Trapezium in a consistent manner. We also compare the properties of this sample to those in nearby star-forming regions of similar ages in order to test whether the initial conditions for disk formation are the same everywhere. We find that disk masses in this environment strongly resemble those in the nearby, low-mass Lupus and Taurus star-forming regions, but not those in the ONC, suggesting that disk formation and evolution may proceed similarly regardless of the mass of the cloud from which they form.

4.2 Observations and reference catalog

In this section, we describe the interferometric observations used in this article, as well as the specific imagining strategy that was used to retrieve the disk sample. Finally, the choice of reference catalog, an important part of disk population studies, is detailed in Section 4.2.3. The reduced ALMA image is compared to near-infrared K_s-band observations of the same region to show the variety of sources identified.

4.2.1 ALMA data

The data that form the basis of this project are 3 mm ALMA Band-3 continuum observations that were taken as part of observing program 2015.1.00669.S (PI: A. Hacar). The primary purpose of this dataset was to collect information on the large-scale distribution of N_2H^+ $(1-0)$ at 93.2 GHz in Orion; these results are described in Hacar et al. (2018). Throughout this paper, we use the same distance to the OMCs: 414 pc (Menten et al. 2007). Our data analysis relies on the same calibrators (J0423-0120 for amplitude and bandpass; J0541-0541 for phase), and covers the same area in a mosaic: a field of $\sim 20'$ in declination and $\sim 4'$ in right ascension, spanning the ISF between the Trapezium and the southern part of the OMC-3 region, and

centered on the OMC-2 cloud. The full image consists of two 148-pointing submosaics: one centered on the OMC-1 cloud and extending over the Trapezium and southern OMC-2, and the other on the OMC-2 and southern OMC-3 clouds. Of these submosaics, the southern fields generally have a lower noise level, due to a slightly deeper integration; the resulting difference in effective primary beam coverage in the full image is on the order of $\sim$ 30% between the northern and southern subfields, which we take into account throughout the following by weighting the image noise with the primary beam coverage at all points.

The continuum data span three windows of 1.8 GHz each, at 93, 104, and 108 GHz. Some line contamination is present, and the corresponding spectral ranges are removed throughout the image. The rest of the data are combined to maximize the S/N of our output images, leading to an effective frequency of 99.5 GHz for the observations discussed here.[1]

4.2.2 Point-source map of OMC-2

The original purpose of the survey data used here was to detect the extended emission of N_2H^+ (1−0) across the cloud with a compact array configuration. This was achieved by using baselines between 3.5 and 92 kλ. As a result, emission can be recovered up to scales of $\sim 1'$ from the 12-meter data alone. For this reason imaging and analyzing the continuum directly from the ALMA 12 m array data products is not suitable for our purposes: contamination from partly resolved-out cloud material is a significant concern, especially for objects that are more embedded.

Fortunately, the interferometric nature of the dataset allows us to efficiently reconstruct the data so that only mostly unresolved point sources are left in the resulting image, as done in other studies (e.g., Felli et al. 1993; Eisner et al. 2008, 2018). This is done by making a cut in the u, v-plane, and removing all baselines shorter than 30 kλ prior to imaging, which leads to a maximum resolvable scale of around $7''$ or $\sim$ 3000 AU at the 414 pc distance of Orion. This scale ensures that even the largest Class II disks are unresolved, while removing the extended cloud emission, and keeping good baseline coverage in u, v-space.

The results of the imaging procedure are shown in Fig. 4.1. In the left panel, the VISTA K_s-band image of the same region from Meingast et al. (2016) is shown; the spatially filtered ALMA map on the right shows the point sources in our field, leaving only a few very young sources marginally resolved. The absence of large-scale emission from this image is immediately obvious; however, numerous point sources are directly correlated to infrared (IR) detections of young stars in the VISTA data.

In order to image the data we used the CASA version 5.4.0 implementation of the CLEAN algorithm in the `tclean` task, to avoid a recently discovered issue with flux retrieval for rectangular mosaics like this one in earlier CASA versions. This task's `mosaic` gridder option leads to the image used in this article, which has a $2.7'' \times 1.6''$ beam, and an effective 1σ noise level of 0.1 mJy beam^{-1} in the southern (deeper) part of the image. Dust mass sensitivities are lower than in previous surveys, both due to the intrinsically fainter dust emission at longer wavelengths and the depth of these observations. We can detect sources at 3σ down to a dust mass of 17 $M_\oplus$ (see Sect. 4.3.2), compared to 0.2 $M_\oplus$ in Lupus (Ansdell et al. 2016). In the least sensitive parts of the northern submosaic, sources down to 32 $M_\oplus$ can be detected. This dataset therefore allows us to sample the upper part of the disk mass distribution function, given a sufficiently large sample.

Around the ONC, significant extended emission and structures at all scales are present,

[1]The reduced data for this project are available online, at the ORION-4D project website `https://sites.google.com/site/orion4dproject/home`.

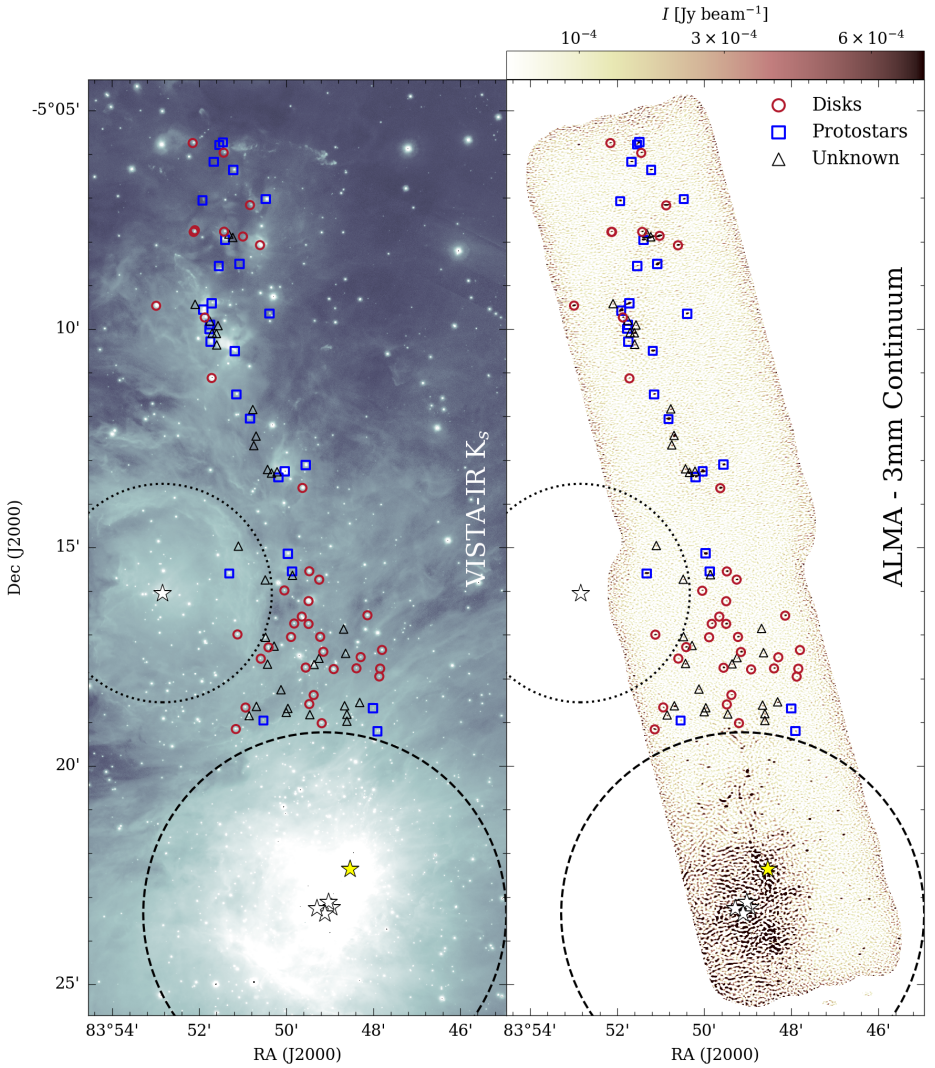

Figure 4.1: Spatially filtered ALMA observations of the OMC-2 region at 3 mm *(right)* and VISTA K_s observations of the same area *(left)* (Meingast et al. 2016). Point sources detected in the ALMA data are shown: disks and protostars from the Megeath et al. (2012) catalog (red circles and blue squares, respectively); sources without detected counterparts in this catalog (black triangles). White stars indicate the locations of the Trapezium stars θ^1 Ori A – D and HD 37061; the dashed black line indicates the photoionization region around the Trapezium out to 0.5 pc, while M42 is marked by the dotted circle. The Orion KL outflow is shown by the yellow star.

and free-free contamination is important at the wavelengths of our observations (Dicker et al. 2009). We therefore avoid the primary photoionization region, which extends out to 0.5 pc from the Trapezium cluster. Despite the lower data fidelity we note that even in the Trapezium several point sources with clear IR counterparts can be identified by eye, but we do not analyze this region further since, as Figure 4.1 shows, this area is strongly confused.

4.2.3 *Spitzer* catalog of sources

The purpose of this study is to compare the disk population in the OMC-2 region with that in other star-forming regions in a homogeneous manner. For this an unbiased and uncontaminated input catalog of YSOs is necessary. Moreover, the classification criteria of sources should be similar to those used in other studies of protoplanetary disks, which places strict limits on the possible base catalogs.

In this article, the base catalog is the *Spitzer* survey of young stellar objects in the Orion A and B clouds by Megeath et al. (2012). This catalog classifies young stellar objects based on their mid-infrared excess in a homogeneous way, and classifies them as Disks, Protostars, and Red and Faint Candidate Protostars, with Disks being Class II YSOs and the other objects younger or ambiguous in nature. Two objects are classified as Red Protostars in the field covered by our observations. These are included in the Protostar class for the purposes of this survey. For some sources (see Furlan et al. 2016; Kainulainen et al. 2017) the classification was changed based on subsequent analysis of the spectral energy distribution; we used the latest published source class in those cases, and updated the source identifications accordingly. Sources identified as protostars with a flat spectrum were not changed, since their nature is ambiguous. In all cases, this approach lead to the reclassification of a suspected disk source to a protostellar source; all reclassified sources (see below) were among the brightest detections, indicating that this is a conservative approach.

The Megeath et al. (2012) *Spitzer* catalog of Orion YSOs is a powerful tool for the type of analysis used in this paper: it is consistent with the way other samples of Class II disks in nearby star-forming regions have been defined, and since the infrared emission from warm dust detected by *Spitzer* is optically thick it is able to detect disks even when disk masses are low; likewise, in theory, it is possible to detect young stellar objects down to the hydrogen-burning limit at the distance of Orion. However, this catalog is not complete; it is limited by the resolution of the telescope ($2'' - 5''$) and because the completeness is sensitive to the nebulosity and stellar density in the area (Megeath et al. 2016; Großschedl et al. 2019), both factors that are not constant across the image.

4.3 Results

By combining the ALMA image with the reference catalog of sources, it is possible to create a flux-limited catalog of YSOs in the surveyed area. In this section, that catalog is described (in Section 4.3.1). The procedure to convert the observed fluxes to masses is detailed in Section 4.3.2, and the robustness of the inferred disk mass distribution to potential confounding effects is tested in Section 4.3.3.

4.3.1 A 3 mm catalog of YSOs in OMC-2

The full ALMA continuum map of the OMC-2 region, shown in Figure 4.1, combined with the *Spitzer* catalog, shows a number of clear detections. In agreement with Kainulainen

et al. (2017), the protostars primarily cluster along the densest part of the ISF; these objects are also those most likely to show evidence of a somewhat resolved structure (see, e.g., P1 and P10 in Fig. 4.B.2). The Class II disks appear to be more scattered over the field. To the south of the ISF, below $-5°15'51''$, the number of protostars drops rapidly due to the lack of dense pre-stellar gas (Hacar et al. 2018). In this region, there is little millimeter-wavelength contamination even prior to the spatial filtering used here, and the number of disks (in the catalog and in the millimeter image) seems to go up, as does the number of sources that do not have a counterpart in the *Spitzer* catalog.

Sources with *Spitzer* counterparts

Over the full field (excluding the ONC), we have sample sizes of $N = 132$ for disks and $N = 35$ for younger objects detected by *Spitzer*. Of the disks, 37 are detected by our ALMA observations at 3σ at least, for a detection rate of 28%. Zoomed-in $36'' \times 36''$ cutouts of all detected disks and protostars with *Spitzer* counterparts are shown in Appendix 4.B as Figures 4.B.1 and 4.B.2. They are ordered by flux for easier inspection; their disk fluxes and protostellar fluxes can be found in Tables 4.1 and 4.A.1, respectively. The full tables (including upper limits) are available on the CDS. One of the disks (D31) is a binary object with a recently reported variability at submillimeter wavelengths, and its mass should therefore be interpreted carefully (Mairs et al. 2019).

The detection rate for protostars is significantly higher than for disks: 26 detections give a detection rate of 69% for these objects. The two populations overlap in flux, but the median flux for protostars is higher than for disks, consistent with the loss of most of the envelope after Class I (Tychoniec et al. 2018). Likewise, the protostars are more likely to be associated with resolved millimeter emission (Fig. 4.B.2) than the disks in the sample (Fig. 4.B.1). Additional data are needed to constrain the mass properties of this protostellar population, preventing their comparison with our well-defined disk sample.

Comparing the results of this survey to those presented in Kainulainen et al. (2017) shows that all protostars detected in their data and in the *Spitzer* catalog are also detected in our data, although the beam in the ALMA data analyzed by Kainulainen et al. (2017) is somewhat larger ($3.75'' \times 2.27''$) and their S/N is lower (at $0.23\,\mathrm{mJy\,beam^{-1}}$). Importantly, the field observed here is also a factor of 2 larger. While the overlap in protostellar sources is large, the data presented in this paper do not allow us to recover a number of starless cores. This is in good agreement with the expectation that such cores lack the compact structures we are looking for, and that they are filtered out by the imaging procedure used here.

Fluxes for all sources were measured by searching for the brightest pixel within a $2.5''$ radius of the catalog positions in the ALMA point-source map to account for the relative beam sizes of both ALMA and Spitzer; noise levels were determined from the image noise weighted with the primary beam coverage at each position. Sources were considered detections in the case their flux exceeded the 3σ noise. In order to ensure that the detections are reliable, a simple visual check was also performed on each position, but no detections were removed or added to the sample as a result.

The brightest and presumably most massive sources in this sample are worth a closer look. For the disks, it is remarkable that the two brightest sources (D1 and D2, top rows of Fig. 4.B.1) at millimeter wavelengths are associated with very extincted regions of the VISTA K_s-image, and may be somewhat contaminated by larger scale emission. However, in general, the ten brightest disks are compact (indicating that they are not misclassified), and are scattered throughout the field. These objects then are the equivalent of the most luminous millimeter disks in nearby low-mass SFRs.

In the protostellar sample it is apparent that the brightest protostars are located in the dense clumps of the ISF; these objects are surrounded by other compact sources at millimeter wavelengths, a significant fraction of which are other protostars. These clumps are concentrated in the north of the surveyed area. There is, however, no statistically significant difference in luminosities of the northern population of protostars (corresponding roughly to the spine of the OMC-2 cloud, beyond 1 pc of the Trapezium) and the protostars in the southern part of the field, given this limited sample size.

Non-*Spitzer* point sources

The effect of the limitations of the *Spitzer* data is that we would underestimate the fraction of lower mass disks in the sample, especially toward the south of the area covered; this region has the brightest background, and while more massive and luminous YSOs are still easily detectable, less massive stars (with similarly faint disks) can be absent from the sample by failing one or more inclusion criteria for the *Spitzer* catalog. In addition, the youngest objects (Class 0) are expected to be completely absent from the *Spitzer* data as they are intrinsically very faint at infrared wavelengths.

As a result, a search for point sources not corresponding to any *Spitzer*-defined YSOs was carried out. The `peak_local_max`-function from `scikit-image` was used to identify point sources in the image, but not in the *Spitzer* catalog, and fluxes were extracted using the same 2.5″ aperture around the identified source position that was also used for the Disk and Protostar samples. This sample, the Unidentified point sources, consists of $N = 34$ sources. As was done for the other objects, cutouts superimposing ALMA data over the VISTA K_s observations from Meingast et al. (2016) are included in Appendix 4.B; fluxes and (tentative) masses are listed in Table 4.A.2.

Classifying this sample is difficult. Other surveys of YSOs in Orion do not cover the full area of our observations, or lack the depth to detect faint objects, leading to ambiguities. Here, the ALMA observations by Kainulainen et al. (2017), and the *Herschel* Orion Protostar Survey (Furlan et al. 2016), the *Chandra* Orion Ultradeep Point Source Catalog (Getman et al. 2005) and the VIenna Survey In OrioN (VISION) (Meingast et al. 2016) are used to provide context to the objects not included in the *Spitzer* catalog. We will implicitly assume that sources without counterparts in any of these surveys are still part of the Orion SFR: the number density of background galaxies is low, at 6.1 ± 3.1 per square degree or < 0.023 in our field of view (Megeath et al. 2012).

By examining the distribution of the Unidentified sources over the cloud, it becomes apparent that this subsample seems to consist of two distinct parts. In the northern part of the image, detections are located along the ISF, in a similar manner to the known distribution of protostars along this structure. If these sources correspond to young, very extincted sources, it is to be expected that this sample overlaps significantly with the youngest YSOs in Furlan et al. (2016), and this is indeed the case. While the overlap is not complete, a large number of sources (10 of 17) located north of $-5°15'51''$ are also detected by Kainulainen et al. (2017) and correspond to a PACS Bright Red Source (PBRS), Class I or Class 0, or starless cores. In contrast, most millimeter point sources in this area have no counterpart in the VISION survey data (see Fig. 4.B.3). In particular, none of the Unidentified sources with counterparts in Kainulainen et al. (2017) are detected in the VISION survey data, indicating their embedded nature. Thus, we do not consider these sources further in our analysis.

In contrast, toward the southern field, the distribution of Unidentified sources more closely resembles that of the Disks in that area. Not only are these objects more scattered over the field than their counterparts to the north, they seem to be fainter on average, al-

Table 4.1: Continuum fluxes and masses for the detected disks

ID	RA	Dec	Flux	Mass
	J2000	J2000	mJy	$M_\oplus$
D1	05:35:23.98	-05:07:53.0	5.0 ± 0.17	273.1 ± 9.78
D2	05:35:23.33	-05:07:09.8	4.8 ± 0.18	259.9 ± 10.30
D3	05:35:18.51	-05:13:38.2	4.4 ± 0.18	240.4 ± 10.42
D4	05:35:31.95	-05:09:28.1	3.9 ± 0.32	209.5 ± 18.21
D5	05:35:22.41	-05:08:04.8	2.8 ± 0.18	146.6 ± 10.22
D6	05:35:17.95	-05:16:45.0	2.5 ± 0.11	127.2 ± 6.59
D7	05:35:16.59	-05:17:23.2	1.9 ± 0.11	97.5 ± 6.32
D8	05:35:24.48	-05:16:59.4	1.8 ± 0.12	91.9 ± 6.80
D9	05:35:17.88	-05:15:32.6	1.7 ± 0.11	81.2 ± 6.12
D10	05:35:16.88	-05:17:02.7	1.5 ± 0.11	74.3 ± 6.36
D11	05:35:21.63	-05:17:17.1	1.5 ± 0.11	72.9 ± 6.41
D12	05:35:18.21	-05:17:44.9	1.4 ± 0.11	67.1 ± 6.52
D13	05:35:12.54	-05:16:33.1	1.4 ± 0.13	64.5 ± 7.68
D14	05:35:16.97	-05:15:44.2	1.3 ± 0.11	59.9 ± 6.34
D15	05:35:24.63	-05:19:09.3	1.3 ± 0.37	58.2 ± 21.32
D16	05:35:15.64	-05:17:47.0	1.1 ± 0.11	49.8 ± 6.39
D17	05:35:25.75	-05:05:57.9	1.0 ± 0.20	44.5 ± 11.44
D18	05:35:28.59	-05:05:44.6	1.0 ± 0.27	44.4 ± 15.24
D19	05:35:25.71	-05:07:46.4	1.0 ± 0.17	42.9 ± 10.01
D20	05:35:19.27	-05:16:44.4	1.0 ± 0.12	40.5 ± 6.64
D21	05:35:16.74	-05:19:01.3	0.9 ± 0.11	40.0 ± 6.29
D22	05:35:13.55	-05:17:45.9	0.9 ± 0.12	39.8 ± 6.67
D23	05:35:27.48	-05:09:44.2	0.9 ± 0.16	37.0 ± 9.41
D24	05:35:23.74	-05:18:39.8	0.7 ± 0.15	28.4 ± 8.40
D25	05:35:28.50	-05:07:46.7	0.7 ± 0.16	28.3 ± 9.22
D26	05:35:17.48	-05:18:22.6	0.6 ± 0.11	22.4 ± 6.41
D27	05:35:20.17	-05:15:59.0	0.6 ± 0.11	21.2 ± 6.32
D28	05:35:18.57	-05:16:34.9	0.6 ± 0.12	18.6 ± 6.70
D29	05:35:11.20	-05:17:20.7	0.5 ± 0.17	16.4 ± 9.65
D30	05:35:26.85	-05:11:07.3	0.5 ± 0.15	13.9 ± 8.74
D31[a]	05:35:17.95	-05:16:13.6	0.5 ± 0.12	12.9 ± 6.68
D32	05:35:11.45	-05:17:57.1	0.5 ± 0.13	12.9 ± 7.32
D33	05:35:19.56	-05:17:02.9	0.5 ± 0.11	12.2 ± 6.54
D34	05:35:17.88	-05:18:35.0	0.4 ± 0.11	11.6 ± 6.42
D35	05:35:11.37	-05:17:46.3	0.4 ± 0.14	10.0 ± 7.85
D36	05:35:22.34	-05:17:32.7	0.4 ± 0.11	9.0 ± 6.37
D37	05:35:13.16	-05:17:30.5	0.4 ± 0.12	6.9 ± 6.75

Notes. [(a)] Variable source at mm-wavelengths (Mairs et al. 2019).

though this may be an effect of the larger number of sources in the outskirts of the ONC. In this area of the map, the main sources of information are the COUPS (Getman et al. 2005) and VISION (Meingast et al. 2016) surveys. Both of these surveys (at X-ray wavelengths and in the K_s band, respectively) are more suited to identifying Class II and Class III protostars. In line with the expectations for a subsample consisting mostly of previously unidentified disks, there is a large fraction of X-ray and near-infrared counterparts for these objects: within a 2.5″ radius, 11 of 18 sources have VISION counterparts, and 7 of 18 have counterparts in the COUP survey. With a median age of 0.8 Myr (Getman et al. 2005), this suggests that Class II sources dominate the southern sample of otherwise unidentified ALMA point sources. In Sect. 4.3.3, the impact of adding these sources to the disk sample is quantified.

4.3.2 Disk masses in the OMC-2 field

In order to estimate the disk mass distribution, we must relate our observed 3 mm fluxes to the disk mass, and to do so in a manner that is consistent with the literature samples this dataset will be compared to. Typically, the following equation is used (e.g., Ansdell et al. 2016; Barenfeld et al. 2016; Eisner et al. 2018):

$$M_{\rm dust} = \frac{d^2 F_{\nu,\,\rm dust}}{\kappa_\nu B_\nu(T_{\rm eff})}. \tag{4.1}$$

Here the millimeter flux F_ν (corrected for free-free emission; see Sect. 4.3.3) is assumed to be due to blackbody emission from optically thin dust with an average temperature $T_{\rm eff}$ and a known effective opacity $\kappa_\nu = \kappa_0(\nu/\nu_0)^\beta$. For the dust opacity, usually $\beta = 1$ is used and $\kappa_{1000\,\rm GHz} = 10\,\rm cm^2\,g^{-1}$ (Beckwith et al. 1990). The effective temperature of the emitting material is taken to be $T_{\rm eff} = 20\,\rm K$, even though it could be argued that a somewhat higher temperature ($T_{\rm eff} = 30\,\rm K$) (see Sect. 4.3.3) is more plausible in a massive star-forming region like Orion. These are the same values used in the articles that present the disk masses to which we compare the OMC-2 sample, thus ensuring a consistent comparison of the samples.

Using a Kaplan-Meier estimator, it is then possible to estimate the disk mass distribution in the OMC-2 field while taking upper limits on the disk mass into account. The resulting distribution and its uncertainties are shown in Figure 4.2. Despite the low fraction of detected sources (29%), the uncertainty level is still excellent thanks to the large sample size. The disks observed clearly cover a wide range of disk masses, between $273 \pm 9.8\,M_\oplus$ and $6.9 \pm 6.4\,M_\oplus$; we note that for this latter value the free-free contribution has been subtracted (see Sect. 4.3.3). The most massive 5% of disks (six sources) have masses in excess of $100\,M_\oplus$. In the following sections, the robustness of this result is considered.

4.3.3 Robustness of results

Effect of sample incompleteness

The Unidentified sources present in our ALMA map may be the result of the underlying biases in the *Spitzer* catalog (Megeath et al. 2016; Großschedl et al. 2019). While it is not possible to find the number of Class II disks not included in the *Spitzer* sample that are also undetected in these ALMA observations, the Unidentified sources allow us to constrain the impact of any biases, and to describe how this affects the comparison of this sample to that in other regions. As discussed in Sect. 4.3.1, most of the northern sources can be matched to Class I and Class 0 YSOs, but it is likely that the southern sources (below $-5^\circ 15' 51''$) are

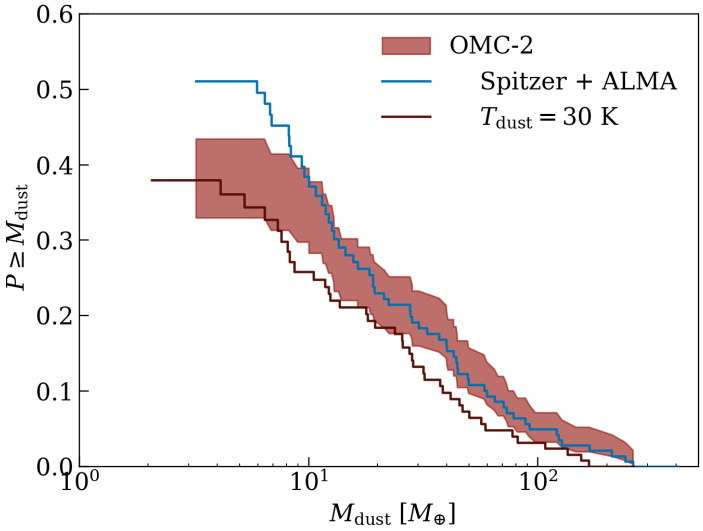

Figure 4.2: Inferred disk mass distribution for the OMC-2 disk population. The effect of adding the ALMA-detected point sources likely to be disks but missing in the *Spitzer* catalog is shown in blue; the red-brown line indicates the impact of a higher effective dust temperature of 30 K.

disks. If all of these sources are added to the *Spitzer* sample, this will give an upper limit on the effect of the missing disk population. This effect is shown in Figure 4.2 by the light blue line. It is obvious that this effect is not significant; most of the Unidentified sources seem to be relatively low in mass, and only significantly contribute to the shape of the disk mass distribution below 10 $M_\oplus$, where the number of upper limits begins to increase rapidly. This could be due to the southern submosaic being deeper; alternatively, this effect may be a true reflection of the underlying population, and an effect of its relative youth.

Contamination by free-free contamination at 3 mm

While other studies generally observe disks in ALMA Band 6 or Band 7 (at 0.8 − 1.3 mm), the longer wavelength (3 mm) at which this sample is observed implies that some of the flux may be contaminated by free-free emission. In the ONC, free-free emission from the surface layers of the disk is a significant part of the flux even at higher frequencies (Eisner et al. 2018). However, our sample is located at distances greater than 0.5 pc from the ONC. As a result, photoionization of the disk surface is not expected and our sample in fact does not overlap with the proplyds cataloged in Ricci et al. (2008). Comparison to the 90 GHz single-dish continuum map from Dicker et al. (2009) also shows that in the area surveyed here, free-free emission has dropped off steeply and continuum should dominate.

However, contamination of our sample by free-free emission from jets cannot be excluded. As a result, we have applied a correction based on the results presented in Tychoniec et al. (2018) for the median free-free emission strength and spectral index. At 3 mm, this is only a small correction of 0.25 mJy, and the results of the comparison to other star-forming regions do not change significantly without it.

Impact of disk temperature and optical depth assumptions

In this study, we followed the same approach in converting the flux due to dust to a disk dust mass as used in previously published work in order to compare our sample as fairly as possible to those results. However, any of these assumptions may not hold, either generally or in specific environments. First, in the warm environment of Orion, and especially around the ONC, it is not unreasonable to assume that the temperature of the emitting dust even in the well-shielded midplane of the disk is higher than in lower mass star-forming regions. The ammonia temperature maps of dense pre-stellar gas in Orion presented in Friesen et al. (2017), for instance, show temperatures exceeding 30 K near the Trapezium. For our data, we assume that this is not an important effect since our stars are usually located quite far from the ONC (at least 0.5 pc) and in an environment where cooler gas temperatures (around 20 K) are measured (Hacar et al. 2018). Nonetheless, temperature variations may lead to an overestimate of disk masses in the ONC (Eisner et al. 2018), an effect also noted by those authors.

In Figure 4.2, the mass distribution of disks is shown when assuming a higher temperature of 30 K. As expected, the effect is to lower the disk masses. However, the size of this effect is only somewhat greater than the scale of the uncertainties in the Kaplan-Meier estimator. In any case, a comparison of the OMC-2 disks with those near the Trapezium should not be affected by this. The Trapezium disks exist in a hotter environment than those in the OMC-2 region and their mass will therefore always be overestimated relative to the disk masses of the OMC-2 sample.

An interesting question is whether the most massive disks identified in OMC-2 are truly more massive, or simply outliers in effective temperature. The distribution of the disks with dust masses $> 100\,M_\oplus$ over the field does not seem to favor any particular environment for massive disks. It is possible that these disks have more luminous host stars than other disks in the sample. However, in nearby low-mass star-forming regions, a similar massive tail of the distribution can be present even around fainter stars, IM Lup for example, which is an M0 star (Reipurth et al. 1996). At the same time the K_s-band data from Meingast et al. (2016) for these stars also do not suggest that they are particularly luminous.

A significant quantity of literature has been devoted to the question of disk optical depths, with evidence suggesting that a non-negligible fraction of the disk surface is optically thick, suggesting that the disk-integrated flux contains information on both surface area and mass (e.g., Ricci et al. 2012; Tripathi et al. 2017). While this would mean our dust mass is incorrect, it would not prevent us from comparing the populations since we then merely apply a scaling factor to all disk luminosities; it would, however, make the interpretation of what causes a difference between populations more complicated. The recently published results from the high-resolution ALMA Large Program DSHARP have suggested (at least for massive disks, which are the objects this survey is sensitive to) that the disk material is optically thin in Band 6 even when trapped in denser rings (Dullemond et al. 2018) in nearby star-forming regions. If this holds in Orion as well, the assumption of optically thin emission can safely be made in Band 3.

Effect of contamination by Class I sources

Throughout this analysis, we have been cautious not to include Class I sources in our Disk sample, in order to make the comparison with other star-forming regions as straightforward as possible. However, the comparison of the Kainulainen et al. (2017) catalog shows several protostars misclassified as disks. This suggests the possibility that some contamination is

present in our sample, for which we have not yet accounted.

The two most massive disks in this sample are all quite close to groups of cores containing young stellar objects; this might indicate either a misclassification or simply a young age of the disk, leading to a higher mass. Compared to other star-forming regions (e.g., Ansdell et al. 2016; Pascucci et al. 2016; Barenfeld et al. 2016), the most massive disk in our sample is not particularly massive, with a dust mass of $273 \pm 9.8\,M_{\oplus}$, indicating that even these sources are still within the range of masses expected for Class II disks. Removing these sources from the sample has no significant effect on the shape of the disk mass distribution, except for removing the tail of the distribution; we therefore conclude that contamination by younger sources is not likely to be a significant concern for our subsequent analysis.

In conclusion, we have studied the effects of sample incompleteness, free-free contamination, disk temperature assumptions, and contamination with younger, embedded sources on the inferred disk masses. In particular, the completeness of the sample and the free-free subtraction have an opposite effect on the disk mass from the assumed disk temperature. In all cases, the effect on the disk mass distribution is small compared to the errors on the Kaplan-Meier estimator. It is thus possible to compare this result to other similar disk mass distributions.

4.4 Discussion

The disks in OMC-2 are a unique population: on the one hand, they are part of a population of disks around stars that formed in a massive star-forming cloud; on the other, they are at least 0.5 pc away from the Trapezium, and outside the region dominated by the radiation field from its massive O stars. Comparing the disk mass distribution of the OMC-2 population and that of disks near the Trapezium therefore allows us to observationally determine a rate of photoevaporative disk mass loss for the first time. Moreover, we can compare this rate to models of external photoevaporation. Simultaneously comparing this population to that in low-mass star-forming regions allows us to determine whether disks evolve in the same way in isolation or if the cloud from which they originated determines the initial disk mass in some way.

In Figure 4.3, the inferred disk mass distribution for our OMC field sample is shown relative to that of several other star-forming regions, derived using a Kaplan-Meier estimator to take the presence of upper limits in the data into account. We do not include the Unidentified source sample for this comparison. In order to compare these populations formally, we use the non-parametric log-rank test to compare them without having to make assumptions on the underlying distributions. In addition to the regions shown here, the same procedure was also followed for disk masses in Taurus (Andrews et al. 2013) and σ Ori (Ansdell et al. 2017).

4.4.1 Environmental dependence

In the right panel of Figure 4.3, the comparison of the OMC-2 population to that in the inner $1.5' \times 1.5'$ of the ONC (Eisner et al. 2018) immediately shows the dramatic effect that the hostile environment of the Trapezium has on disk properties. This is confirmed by a log-rank test: the ONC sample and the likewise photoevaporated population around σ Ori (not shown) are both inconsistent with the mass distribution of the OMC-2 disks, with $p \ll 0.05$ in both cases.

While a decrease in disk masses with proximity to the Trapezium has been shown, the OMC-2 sample allows us for the first time to statistically characterize the evolution of disk

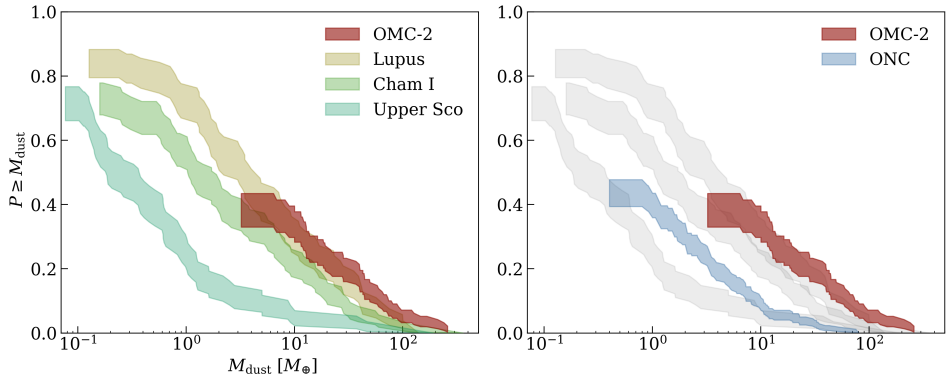

Figure 4.3: Inferred disk mass distribution in OMC-2 (red) compared to the disk mass distribution in low-mass star-forming regions (*left*) and to disks in the inner $1.5' \times 1.5'$ of the ONC (blue, *right*). Data for the low-mass regions comes from Ansdell et al. (2016) for Lupus, Pascucci et al. (2016) for Cham I, and Barenfeld et al. (2016) for Upper Sco; only Class II objects with known stellar masses are included. For the ONC, disk masses come from Eisner et al. (2018). The three low-mass regions are reproduced as gray silhouettes in the right panel to facilitate the comparison.

masses in a dense clustered environment, but outside the main photoevaporation region. To do so, we perform a log-rank test comparing the masses of the ONC population with the masses of the OMC-2 sample multiplied by a constant, given the apparent similarity between the two mass distributions. This leads to a mass ratio of $0.18^{+0.18}_{-0.11}$ between the regions, or a loss of some 80% of the dust mass in 1 Myr following the age inferred by Megeath et al. (2016) for the ONC.

It is interesting to compare the mass loss of these disks to model predictions of the effect of external photoevaporation. In the ONC, and specifically in the inner 0.1 pc around θ^1 Ori C targeted by Eisner et al. (2018), external photoevaporation by far-UV (FUV) photons is the dominant source of mass loss for disks (Scally & Clarke 2001; Hollenbach et al. 2000), and leads to a mass loss of $\dot{M}_{\rm FUV} = 2 \times 10^{-9} r_d \, M_\odot \, {\rm yr}^{-1}$, where r_d is the disk radius in astronomical units. Assuming a typical disk around a solar-mass star in our sample, with a dust mass of $20 \, M_\oplus$, an outer radius of 40 AU, and a gas-to-dust ratio of 100, but which has been exposed to FUV radiation for 0.5 Myr, our observations imply a photoevaporative mass loss rate of $1 \times 10^{-8} \, M_\odot \, {\rm yr}^{-1}$ in the ONC. Importantly, in this approach the difference in disk temperatures in the ONC and the OMC-2 sample studied here is somewhat degenerate with the age of the region: if the disks in the ONC are warmer, the time during which the disk has been exposed to the radiation field can be longer. Comparing this with the result of the equation in Scally & Clarke (2001) the expected mass loss rate for our fiducial disk in the ONC due to FUV radiation is $8 \times 10^{-8} \, M_\odot \, {\rm yr}^{-1}$. This is a remarkably close correspondence.

To test this result with a more refined model, we have also used the FRIED grid of externally irradiated disks (Haworth et al. 2018). Using the same parameters for the disk and a host star mass of $1 \, M_\odot$ yields a mass loss of $5.25 \times 10^{-8} \, M_\odot \, {\rm yr}^{-1}$ in a radiation field of $10^4 \, G_0$. Here $G_0 = 1.6 \times 10^{-3} \, {\rm erg \, cm^{-2} \, s^{-1}}$ is the Habing unit of UV radiation between $912 - 2400$ Å, appropriate for the properties of θ^1 Ori C at the distances of the ONC disks (Simón-Díaz et al. 2006). In contrast, the radiation field in the OMC-2 population must be much lower. With

purely geometric dilution of the radiation field, based on the average distances of these samples, G_0 in the OMC-2 should be a factor of 6×10^{-3} lower. This is probably an overestimate given the presence of dust absorption. In this irradiation regime, the FRIED grid predicts very low mass loss rates, and low sensitivity to variations in the strength of the UV field, for disks with a radius < 100 AU. More importantly, the resulting mass loss value is again in good agreement with the calculation made from the observations presented here. This suggests that the primary driver of disk destruction in the ONC is indeed external photoevaporation.

4.4.2 Time evolution

Comparing the OMC-2 disk mass distribution to that of low-mass regions, it becomes obvious that this population is quite massive (in terms of the most massive quartile), and it resembles the young star-forming regions much more closely than the evolved population of disks. Using a log-rank test, we cannot distinguish between the Lupus and OMC-2 disks ($p = 0.87$); the same is true for the comparison to Taurus ($p = 0.76$) and Cham I ($p = 0.2$). However, the tail of the distribution for disk masses in OMC-2 seems to be somewhat more massive than in Taurus and Lupus, and this difference is even bigger when comparing OMC-2 to Cham I. The result of the log-rank tests does not change if we assume a 30 K effective dust temperature (or, alternatively, a higher opacity). This is also true when comparing the OMC-2 disks to those in Upper Sco: in all cases, the latter population is significantly less massive.

Including the Unidentified sources that are likely to be disks leads to the OMC field population becoming somewhat more massive, but has no significant effect on the comparison between the disk mass distributions either. Interestingly, it does seem that the shape of these disk mass distributions is now more similar down to our detection limit, even if the average mass increases somewhat. However, our main conclusion is not affected: disks in OMC-2 appear to be most similar to young nearby star-forming regions, and may be somewhat more massive.

The result of this comparison is remarkable given the very different densities, histories, and scales of star formation in these regions as a whole. However, in terms of age, Lupus, Taurus, and the OMC-2 population appear to be quite similar, while Cham I with its slightly lower disk masses is older: the OMC-2 stars are around 1 Myr in age, compared to Lupus and Taurus at $1 - 3$ Myr and Cham I at $3 - 5$ Myr. This suggests that outside the 0.5 pc region dominated by the Trapezium, age alone is the dominant factor in protostellar disk evolution.

4.4.3 Disk evolution across SFRs

Our results reveal that studying the OMC-2 disk population is a bridge between disks in the well-studied low-mass star-forming regions and in the dense, highly irradiated environment of the ONC, even with unresolved and relatively shallow observations. It is a population ripe for follow-up analysis at different wavelengths and higher resolution. In particular, resolving these disks will enable us to compare disk radii as well as masses. In this context, the high-mass tail of disks in the OMC-2 and ONC populations is particularly interesting. Especially in the OMC-2 sample, the inferred masses for these disks are similar to the most massive disks in low-mass star-forming regions, such as TW Hya, IM Lup, and other well-known objects (Andrews et al. 2016b; Cleeves et al. 2016). These disks are often seen to have dust gaps and rings in nearby SFRs, consistent with planet formation, at scales that can be resolved by ALMA relatively easily even at the distance of Orion A (Andrews et al. 2018; van der Marel et al. 2018b; van Terwisga et al. 2018b). Observing such features and studying their relative properties in the OMC-2 and ONC environments would help clarify

how environment affects disk substructures. Finally, resolved observations of disks in the OMC-2 cloud will allow us to test more precisely the predictions from theoretical models of disk photoevaporation, which suggest that the radius of a disk is an important factor in the efficiency with which it loses mass.

The result that Class II disk masses, on average, do not sensitively depend on the underlying cloud properties if no strong radiation field is present has important implications for the earlier evolution of circumstellar material. It implies that disk formation can proceed similarly everywhere, with the possible exception of Corona Australis (Cazzoletti et al. 2019) and ρ Ophiuchi (Williams et al. 2019). In turn, if planet formation begins early on in the life of a disk, this too is not strongly affected by environmental factors.

4.5 Conclusions

We observed 132 protoplanetary disks in the OMC-2 cloud at 3 mm with ALMA, and a population of 35 younger protostars, and we used these observations to infer the disk mass distribution in this region. By placing the masses of disks in OMC-2 in the context of both the highly irradiated Trapezium disks, and of nearby low-mass star-forming regions, we can link the evolution of circumstellar material in these very different environments. The massive disks detected in this study are a valuable source of information on disk evolution, and emphasize the power of unbiased surveys, even on relatively shallow datasets. The protostellar sample, while small, is clearly more concentrated along the ISF, tracing local cloud properties, in line with earlier results.

- Dust masses of disks in the OMC field, outside the photoionization region of the Trapezium, reveal a population of protoplanetary disks that appears indistinguishable from the disks in low-mass star-forming regions like Lupus and Taurus, which have similar ages but much smaller populations of YSOs than the Orion molecular clouds.
- Comparing the OMC-2 sample of disks with the inner $1.5' \times 1.5'$ around the Trapezium reveals a typical mass loss of $\sim 80\%$ of the disk mass in 1 Myr. The mass ratio between OMC-2 and ONC disks is $0.18^{+0.18}_{-0.11}$; in other words, ONC disks are less massive by a factor of ~ 5.
- Both of these results are robust with respect to our parametrization of disk mass and sample biases.
- The difference in mass between the OMC-2 and Trapezium-cluster samples is consistent with disk mass loss driven by FUV radiation.
- Together, the comparisons to photoevaporated and isolated low-mass regions imply that in isolation, disk formation and evolution proceeds similarly, regardless of cloud mass.

Table 4.A.1: Continuum fluxes and masses for the detected protostars

ID	RA J2000	Dec J2000	Flux mJy	Mass $M_\oplus$
P1	05:35:27.63	-05:09:33.5	23.1 ± 0.16	1316.6 ± 9.45
P2	05:35:20.14	-05:13:15.5	21.6 ± 0.17	1229.0 ± 9.84
P3	05:35:23.33	-05:12:03.1	17.8 ± 0.16	1010.3 ± 9.03
P4	05:35:25.82	-05:05:43.6	15.0 ± 0.24	850.9 ± 14.07
P5	05:35:19.84	-05:15:08.5	9.2 ± 0.12	516.8 ± 6.69
P6	05:35:24.30	-05:08:30.6	9.0 ± 0.17	502.2 ± 9.88
P7	05:35:25.61	-05:07:57.3	8.6 ± 0.17	478.9 ± 9.92
P8	05:35:25.23	-05:15:35.7	8.4 ± 0.13	467.4 ± 7.22
P9	05:35:24.73	-05:10:30.2	7.5 ± 0.16	418.4 ± 9.20
P10	05:35:26.84	-05:09:24.6	2.9 ± 0.17	150.6 ± 9.73
P11	05:35:18.20	-05:13:06.7	2.8 ± 0.18	148.4 ± 10.24
P12	05:35:27.00	-05:09:54.1	2.2 ± 0.16	110.5 ± 9.41
P13	05:35:21.55	-05:09:38.7	2.1 ± 0.18	104.7 ± 10.42
P14	05:35:20.73	-05:13:23.6	2.1 ± 0.17	104.2 ± 9.60
P15	05:35:27.07	-05:10:00.4	2.0 ± 0.16	101.8 ± 9.35
P16	05:35:19.47	-05:15:32.7	1.8 ± 0.11	89.3 ± 6.15
P17	05:35:24.86	-05:06:21.4	1.7 ± 0.18	82.6 ± 10.18
P18	05:35:21.87	-05:07:01.6	1.6 ± 0.19	80.0 ± 10.72
P19	05:35:27.70	-05:07:03.5	1.3 ± 0.17	57.9 ± 10.07
P20	05:35:24.58	-05:11:29.7	1.2 ± 0.15	54.0 ± 8.61
P21	05:35:26.66	-05:06:10.3	1.2 ± 0.19	53.4 ± 10.70
P22	05:35:26.97	-05:10:17.2	0.7 ± 0.16	27.5 ± 9.20
P23	05:35:12.02	-05:18:40.8	0.7 ± 0.12	23.9 ± 6.82
P24	05:35:26.20	-05:08:33.4	0.6 ± 0.17	22.8 ± 10.04
P25	05:35:11.61	-05:19:12.4	0.4 ± 0.12	11.2 ± 6.87
P26	05:35:22.10	-05:18:57.7	0.3 ± 0.11	5.5 ± 6.50

Appendix

4.A Fluxes of additional sources identified in the ALMA data

In the following tables the fluxes, masses, and positions of the protostellar sources (Table 4.A.1) are listed, as are the fluxes and positions for the sample of unknown sources that are detected with ALMA but are not in the Spitzer catalog (Table 4.A.2). We note that the masses for the detected protostars are calculated with the same assumptions that were made for the disks, but that these objects are expected to have significant contamination from envelope material. Finally, for the protostellar sources, some flux may be resolved out.

Table 4.A.2: Continuum fluxes and masses for objects not included in the *Spitzer* catalog

ID	RA	Dec	Flux mJy	Mass $M_\oplus$
U1[a]	05:35:21.36	-05:13:17.8	10.5 ± 0.16	590.1 ± 9.37
U2[a]	05:35:26.42	-05:10:06.1	6.2 ± 0.16	344.1 ± 9.34
U3[a]	05:35:24.91	-05:07:54.3	5.9 ± 0.17	323.7 ± 9.84
U4[a]	05:35:19.43	-05:15:38.3	4.6 ± 0.11	249.1 ± 6.16
U5[a]	05:35:22.77	-05:12:27.0	3.2 ± 0.16	170.9 ± 9.30
U6[b, c]	05:35:22.74	-05:18:38.2	2.4 ± 0.12	122.9 ± 6.65
U7[a]	05:35:27.02	-05:09:49.0	1.3 ± 0.16	63.1 ± 9.46
U8[a]	05:35:26.81	-05:10:05.7	1.2 ± 0.16	52.0 ± 9.32
U9[c]	05:35:21.72	-05:17:40.2	1.1 ± 0.11	46.5 ± 6.40
U10[a]	05:35:25.27	-05:07:49.8	0.8 ± 0.17	33.3 ± 9.92
U11[c]	05:35:13.25	-05:18:32.8	0.8 ± 0.11	32.8 ± 6.61
U12	05:35:23.07	-05:11:50.6	0.8 ± 0.16	32.8 ± 9.17
U13[b, c]	05:35:23.40	-05:18:50.8	0.7 ± 0.14	27.8 ± 7.87
U14	05:35:20.48	-05:18:15.3	0.6 ± 0.11	22.2 ± 6.61
U15[a]	05:35:21.72	-05:13:12.9	0.6 ± 0.16	20.6 ± 9.22
U16[b]	05:35:19.85	-05:18:41.0	0.6 ± 0.11	19.1 ± 6.54
U17	05:35:26.27	-05:09:55.4	0.6 ± 0.16	19.0 ± 9.44
U18	05:35:28.37	-05:09:26.1	0.6 ± 0.16	18.2 ± 9.20
U19[a]	05:35:22.98	-05:12:40.0	0.6 ± 0.16	17.8 ± 9.05
U20	05:35:26.39	-05:10:21.9	0.5 ± 0.16	16.4 ± 9.18
U21[b, c]	05:35:17.44	-05:17:40.6	0.5 ± 0.11	15.7 ± 6.40
U22	05:35:20.84	-05:13:16.1	0.5 ± 0.17	15.6 ± 9.61
U23[c]	05:35:16.99	-05:17:32.1	0.5 ± 0.11	14.4 ± 6.34
U24	05:35:21.11	-05:17:15.5	0.5 ± 0.11	12.3 ± 6.43
U25[c]	05:35:14.43	-05:18:49.0	0.4 ± 0.11	10.9 ± 6.39
U26[c]	05:35:14.73	-05:16:52.0	0.4 ± 0.11	9.7 ± 6.41
U27	05:35:14.43	-05:18:58.5	0.4 ± 0.11	9.6 ± 6.39
U28[b, c]	05:35:20.00	-05:18:46.4	0.4 ± 0.11	8.4 ± 6.52
U29	05:35:14.64	-05:18:37.3	0.4 ± 0.11	8.2 ± 6.36
U30[c]	05:35:24.40	-05:14:58.2	0.4 ± 0.13	8.2 ± 7.26
U31	05:35:21.93	-05:15:44.5	0.4 ± 0.10	7.8 ± 5.84
U32	05:35:17.83	-05:18:49.5	0.4 ± 0.11	7.2 ± 6.38
U33[b, c]	05:35:21.90	-05:17:03.3	0.4 ± 0.11	6.8 ± 6.52
U34[b, c]	05:35:14.55	-05:17:25.3	0.4 ± 0.11	6.0 ± 6.48

Notes. [(a)] Source detected in Kainulainen et al. (2017) [(b)] Source detected in COUPS (Getman et al. 2005) [(c)] Source detected in VISION (Meingast et al. 2016)

4.B Cutouts of detected sources

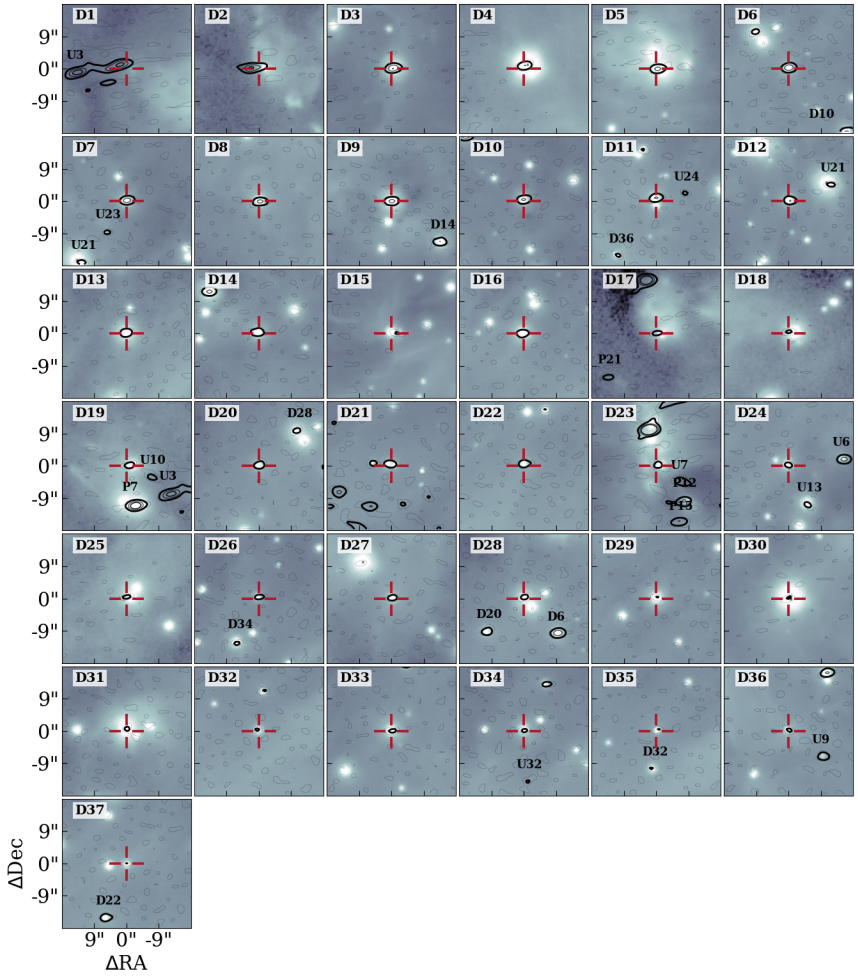

Figure 4.B.1: All disks detected in *Spitzer* (Megeath et al. 2012) and ALMA (this study), ordered by millimeter flux. Solid contours show the 3, 12, and 24σ noise levels of the ALMA observations; dashed contours show the 1σ flux. The background is the VISTA K_s image from Meingast et al. (2016). Small labels indicate the types of nearby objects in this survey.

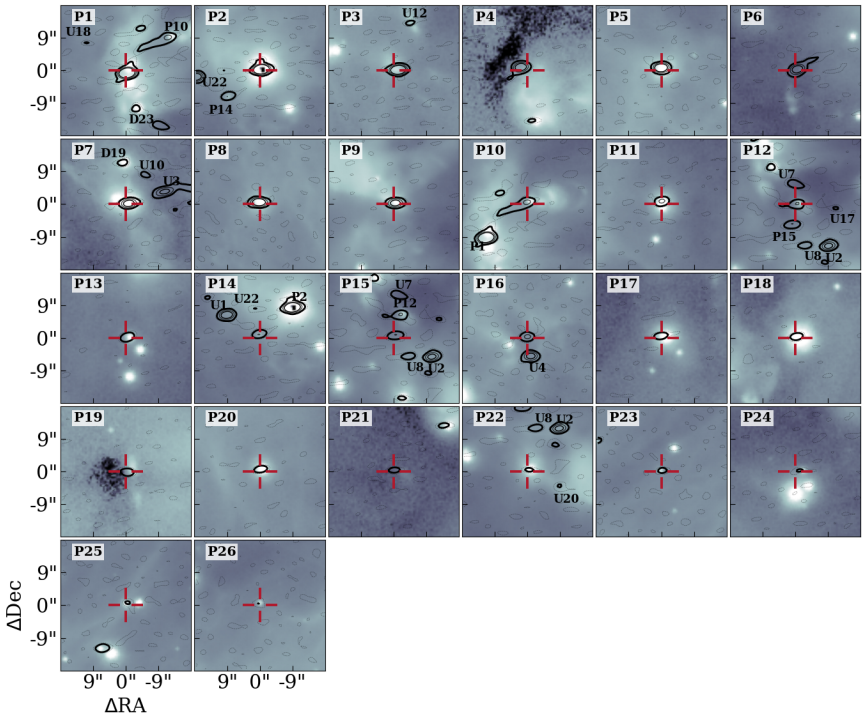

Figure 4.B.2: All protostars detected in *Spitzer* (Megeath et al. 2012) and ALMA (this study), ordered by millimeter flux. Solid contours show the 3, 12, and 24σ noise levels of the ALMA observations; dashed contours show the 1σ flux. The background is the VISTA K_s image from Meingast et al. (2016). Small labels indicate the types of nearby objects in this survey.

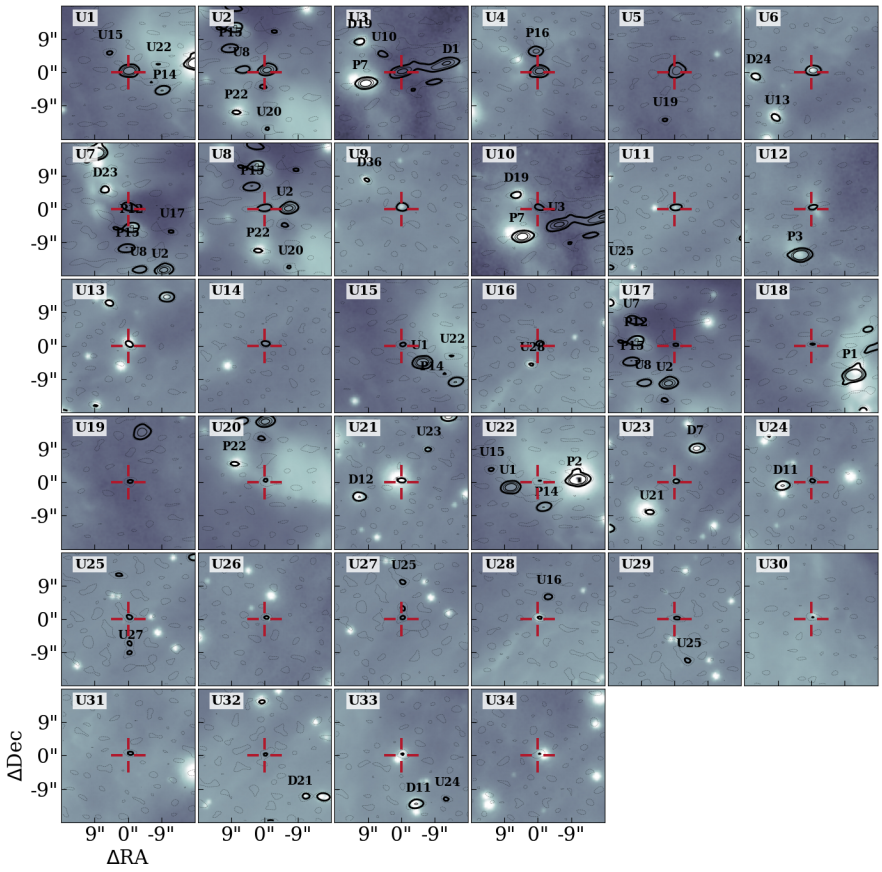

Figure 4.B.3: All point sources detected by ALMA (this study), but missing *Spitzer* counterparts (Megeath et al. 2012), ordered by millimeter flux. Solid contours show the 3, 6, 12, and 24σ noise levels of the ALMA observations; dashed contours show the 1σ flux. The background is the VISTA K_s image from Meingast et al. (2016). Small labels indicate the types of nearby objects in this survey.

5

Protoplanetary disk masses in NGC 2024: evidence for two populations

S.E. van Terwisga, E.F. van Dishoeck, J. Di Francesco, R.K. Mann, N. van der Marel, M. Meyer, S.A. Andrews, J. Carpenter, J.A. Eisner, C.F. Manara, and J.P. Williams.
To be submitted to A&A

Abstract

Protoplanetary disks in dense, massive star-forming regions (SFRs) are strongly affected by their environment. How this environmental impact changes over time is an important constraint on disk evolution and external photoevaporation models.

Aims: We characterized the dust emission from 179 disks in the core of the young (0.5 Myr) NGC 2024 cluster. By studying how the disk mass varies within the cluster, and how the NGC 2024 disks compare to other regions, we determined how external photoevaporation influences disk properties over time.

Methods: Using the Atacama Large Millimeter/submillimeter Array (ALMA), a $2.9' \times 2.9'$ mosaic centered on NGC 2024 FIR 3 was observed at 225 GHz with a resolution of $0.25''$. This field contains 179 disks, 7 new disk candidates, and several protostars.

Results: Of the 179 disks in the sample, 57 are detected, for an overall detection rate of $32 \pm 4\%$. Few of the disks are resolved, with the exception of a giant ($R = 300$ AU) transition disk. Serendipitously, we also observe a millimeter flare from a X-ray bright YSO, and resolve a Class 0 YSO in the FIR 3 core. Two distinct disk populations are found in the observed field: a more massive one in the east, along the dense molecular ridge hosting the FIR 1-5 YSOs, with a detection rate of $45 \pm 7\%$. In the western population, towards IRS 1, only $15 \pm 4\%$ of disks are detected.

Conclusions: NGC 2024 hosts two distinct disk populations. Disks along the dense molecular ridge are young (0.2–0.5 Myr) and partly shielded from the FUV radiation of IRS 2b; their masses are similar to isolated 1–3 Myr old SFRs. The western population is older and at lower extinctions, and may be affected by external photoevaporation from both IRS 1 and IRS 2b; however, it is possible these disks had lower masses to begin with.

5.1 Introduction

Protoplanetary disks are formed and evolve in a wide variety of environments: from low-mass, isolated star-forming regions (SFRs) like the Taurus and Lupus clouds, to dense, massive SFRs like the Orion Nebula. Disks are not completely independent of their environment. For instance, IM Lup's extended CO halo has been interpreted as evidence of external photoevaporation (Haworth et al. 2017). However, it is in the massive star-forming regions that the impact of environment on the evolution of disks becomes most pronounced. The proplyds in the Orion Nebula Cluster (ONC) have long been recognized as disks that are being ionized by UV radiation from the bright young stars in the Trapezium, losing mass as a result (O'Dell et al. 1993; O'Dell & Wen 1994; Mann et al. 2014; Eisner et al. 2018). Not only is the effect of environment on disks larger in massive star-forming regions, but more stars are formed in clusters overall (e.g., Lada & Lada 2003; Carpenter 2000; Porras et al. 2003). Understanding the impact that these environments have on the evolution of disks, and in particular, on the amount of mass available for planet formation as a function of time, is therefore important for our understanding of the observed planet population.

Surveys of individual populations of protoplanetary disks using their millimeter continuum emission have, in recent years, become a key tool for studying disk evolution. The Atacama Large Millimeter/submillimeter Array (ALMA) has not just the sensitivity but also the resolution to resolve disks out to the distance of the Orion clouds. As a result, the continuum emission from cold, millimeter-sized dust grains in the disk is now an easily accessible observable. Disk (dust) mass distributions that are based on the assumption that continuum flux is proportional to disk mass are now available for most nearby low-mass star-forming regions.

In Orion, several areas of massive star formation can provide a counterpart to these now well-studied low-mass envrionments. The Orion Nebula Cluster (ONC), in Orion A, is the richest cluster within 500 pc of the sun, with an age of about 1 Myr. It has now been studied quite extensively with ALMA, revealing a strongly photoevaporated population of protoplanetary disks in the inner 0.5 pc around the massive stars in the Trapezium driven by the O6 star θ^1 Ori C (e.g., Mann et al. 2014; Eisner et al. 2018). Beyond 0.5 pc of this star, however, the disk mass distribution is surprisingly close to that in Lupus and Taurus(van Terwisga et al. 2019b), which have comparable ages. The σ Orionis region in Orion B is somewhat older at 3-5 Myr (Oliveira et al. 2002, 2004), and its ionizing star (σ Ori) is an O9 star, cooler than the Trapezium's most massive stars. However, disks in this region likewise show evidence of external photoevaporation in submillimeter observations (Ansdell et al. 2017). In σ Orionis, the radius out to which this effect is important is larger (2 pc) than in the ONC, but its overall impact on the disk masses in the region is lower.

The protoplanetary disks of NGC 2024 are, in this context, an important missing link. It hosts the youngest population of YSOs in the Orion clouds, at 0.5 Myr (Meyer 1996; Levine et al. 2006). While precise ages are difficult to determine, NGC 2024's stellar population is certainly young relative to the ONC (Eisner & Carpenter 2003). There is, however, evidence of a radial age gradient (Getman et al. 2014). Apart from its youth, NGC 2024 is also the richest SFR in Orion B (Meyer et al. 2008). There is an ongoing debate on the identification of the ionizing source(s) in the region; unlike in the ONC, this is not directly visible. Burgh et al. (2012) find evidence of an O6 to B0-type star in the deeply extincted cluster core. IRS 2b is a candidate (Bik et al. 2003; Kandori et al. 2007), but its spectral type may be too late. IRS 2b, IRS 2, and possible other sources located close to each other on the sky together are the most likely drivers of ionization in the nebula (Meyer et al. 2008). Even outside the cluster's

inner regions, IRS 1 (B0.5) may also contribute to the total flux (Burgh et al. 2012).

With its young population and massive stars, NGC 2024 provides a perspective on how disks are affected by external UV irradiation in the first $\sim$ Myr after the envelope has dissipated. Previous observations of disks in NGC 2024 with millimeter interferometers have managed to detect a number of disks in this region, but did not resolve them, and are likely affected by the complicated large-scale cloud emission in this SFR (Eisner & Carpenter 2003; Mann et al. 2015).

In this article, we use a large-scale ($2.9' \times 2.9'$) ALMA mosaic of the inner part of NGC 2024, centered on the dense molecular ridge (Watanabe & Mitchell 2008), and including IRS-2b and IRS 1 in the field. Our sample of 187 disks is both larger than previous studies, while ALMA's sensitivity enables us to detect disks down to less than 1 $M_\oplus$ in dust. These observations cover a wide range of physical conditions, from the direct vicinity of IRS 2b, to the deeply obscured parts of the dense molecular ridge, to the less obscured environment to the west of the cluster core. Combined with the large sample size, this means that we can study how disk properties vary across the cluster. By comparing the dust mass distribution to that of disks in the ONC and nearby low-mass star-forming regions, we are able to trace the disk mass evolution across time in a photoevaporating sample.

5.2 ALMA observations and data reduction

The observations published in this article were taken as part of the ALMA program 2017.1.01102.S (PI: R. Mann), and consist of a Band 6 mosaic of a $2.9' \times 2.9'$ square region. The imaged area covers both the immediate environment of IRS 2b, the dense molecular ridge hosting the FIR-3 and FIR-2 sources, the FIR-4 source (resolved as a binary Class 0 protostar) and a relatively emptier region to the West.

The full mosaic consists of 149 pointings, centered on $05^{\mathrm{h}}41^{\mathrm{m}}40.5^{\mathrm{s}}$ $-01^\circ54'16.25''$. Over the course of the observations, the full set of 149 pointings was observed on 8 separate occasions, spread out over 7 nights. Atmospheric conditions were mostly stable during and between integrations of the full mosaic. All observations used the same calibrators: amplitude and bandpass calibration were carried out on J0432-0120; phase calibration was performed on J0541-0211.

The spectral setup of the observations covers the mm-continuum with two spectral windows, at 230 GHz and 219 GHz; the effective rest frequency of the combined observations is 225 GHz. Additionally, three spectral widows cover the $J = 2 - 1$ transitions of ^{12}CO, ^{13}CO, and C^{18}O, with a 122 kHz channel width. However, due to the dense interstellar environment towards NGC 2024, in most pointings emission from the cloud contaminates the science targets severely, or becomes optically thick and resolves out. Therefore, we focus here on the results from the continuum observations; the observations presented here have been made after flagging out the channels with strong line emission.

Images of the data were made in CASA 5.4.0, using the *tclean* task. In all instances (except where explicitly noted), we used Briggs weighting, with a robust parameter of 1.0, for the best image S/N and a compact beam shape. The data span baselines from $10 - 1700$ kλ. The chosen observing schedule led to the shortest baselines being sampled with very little field rotation. In order to suppress the resulting partially resolved-out emission from the dense molecular ridge, and to detect the (compact) disks more clearly, another image was generated where only baselines > 150 kλ were included. The effective beam shape is $0.26'' \times 0.18''$ (FWHM) for the full baseline image. For the long-baseline image, the effective beam shape is $0.22'' \times 0.15''$.

The data were self-calibrated to improve S/N. Each integration of the mosaic was separately self-calibrated for phase only, down to the integration interval. The first full integration was affected by slightly higher noise levels and contains an extremely bright outburst from a variable object (see 5.3.3). For this reason, the data from this first integration were not used for creating the images from which we derive the dust masses of disks; this does not significantly affect the noise level. Due to overlapping fields of slightly different depths, the full synthesized image has spatially variable noise. In the deepest part of the image, the rms noise is 0.052 mJy beam^{-1}. After restricting the baseline coverage to baselines $> 150\,\mathrm{k}\lambda$, this increased to 0.058 mJy beam^{-1}. The spatial variability in the noise level was taken into account during source extraction by weighting the noise (estimated in an empty part of the image) with the primary-beam coverage, as calculated by *tclean*. This is a small effect ($< 5\%$) everywhere but on the edges of the primary beam of the outermost pointing.

5.3 Results

In this section we present the results of our millimeter continuum survey of protoplanetary disks in NGC2024. For the detected sources, we derive dust masses and the disks' dust mass distribution. Several sources in the image are particularly interesting and discussed separately.

5.3.1 A 1.3 mm catalog of disks in NGC 2024

To study the demographics of NGC 2024 disks with ALMA, it is essential to have a properly defined sample to study. In this work, we used the catalog of infrared-excess objects from Meyer (1996), which were identified based on their JHK colors. This catalog is the largest in the field covered by the ALMA observations, ensuring an excellent sample size of 179 objects. Drawing the sample from this catalog means the selection criteria for sources are uniform. The excess emission at NIR wavelengths is due to hot, optically thick dust, and therefore should be a good tracer of disk presence without being biased to the mass of millimeter-sized grains in the cold midplane regions that ALMA is sensitive to. Only the extreme North of the field (18″ in declination) is not covered in the catalog, leading to the exclusion of one bright, somewhat resolved source.

A significant limitation of the catalog used here is that, with only JHK-band photometry, it is possible some objects may be incorrectly included. In particular, outflow cavities of younger sources may be mistaken for disks. While the SEDs of many sources are not well-sampled, we cross-referenced the Meyer (1996) catalog with the HOPS catalog of protostars in Orion (Furlan et al. 2016). This led us to exclude HOPS 384 (IRC 227 / 229) as a Class 0 source, but no other sources were rejected from the catalog for this reason. We also established that an embedded YSO which is associated with NGC 2024 FIR 3 in our ALMA observations is not detected in the Meyer (1996) catalog, suggesting that the misclassification of younger sources as disks should be rare. Finally, we note with Mann et al. (2015) that JHK colors of the catalog members are generally not very red, indicating that most of them are dominated by disks and therefore representative of Class II disks.

For all sources in the base catalog, we performed aperture photometry on the brightest point source with emission $> 3\sigma$ in the long-baseline image that was found within 1″ of the catalog position, in order to account for uncertainties in catalog; if no source was found, the flux was measured in a 0.25″ beam on the catalog position. Detected source positions show no significant offset from the catalog positions on average. The resulting millimeter catalog

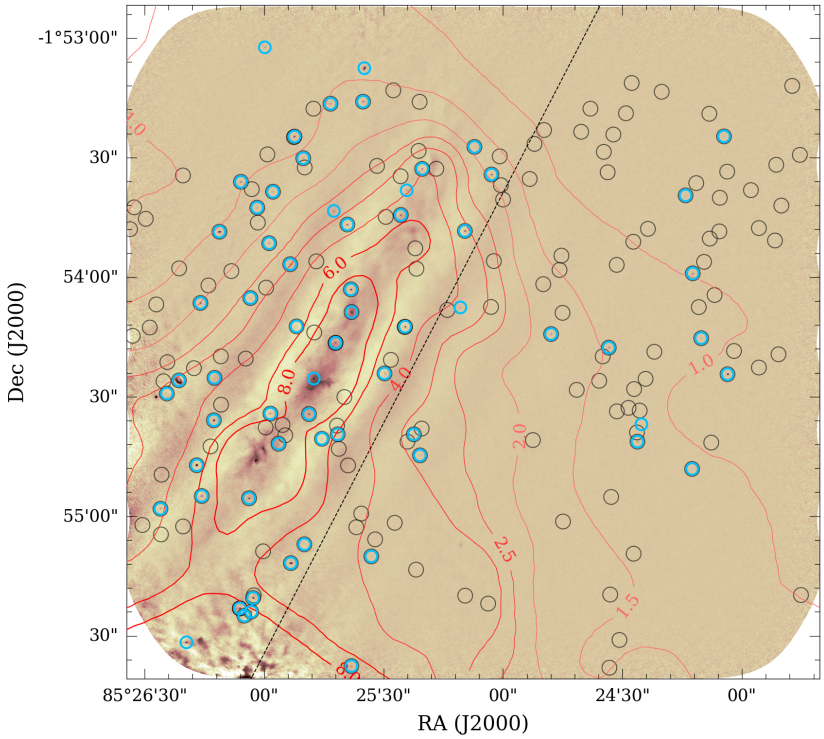

Figure 5.1: ALMA Band 6 mosaic of the NGC 2024 core region, in the background. Detected disks are indicated with blue circles; thin black circles show positions of disks in Meyer (1996). Red and pink contours show the *Herschel* PACS 160 μm data (in Jy pixel^{-1}) from Stutz et al. (2013), revealing the location of the dense molecular ridge. The eastern and western populations (Section 5.4.1) are separated by the thin black dashed line.

was checked manually, and tested for the presence of extended emission in the full-baseline image. This last step was only necessary for the most radially-extended disk in the field after IRS-2b. One source (IRC 115) was found to be a binary object, and has been split into IRC 115 A and IRC 115 B.

Of the 179 objects in the sample, 57 are detected, for an overall detection rate of 32 ± 4%. The brightest source in the field, IRC 101, has a flux of 204 ± 1.1 mJy; the median flux for detected sources is 2.5 mJy, while the faintest object has a flux of only 0.48 ± 0.13 mJy. These errors do not include the standard (absolute) flux calibration accuracy of 10%. Zoomed-in cutouts of the detected sources are shown in Appendix 5.A, in Figure 5.A.1 and 5.A.2. The fluxes of the detected sources are listed in Table 5.1; the upper limits can be found in Table 5.B.1 in Appendix 5.B. Sources are detected throughout the field, as Figure 5.1 shows, even in regions with significant contamination from partly resolved-out cloud emission in the full-baseline image.

Table 5.1: Continuum fluxes and masses for the detected disks

Name	RA	Dec	Flux mJy	Mass $M_\oplus$
IRC101	5:41:45.43	-1:54:25.9	204.8 ± 1.15	1055.2 ± 5.94
IRC067	5:41:45.13	-1:54:47.2	37.1 ± 0.18	190.9 ± 0.91
IRC086	5:41:44.84	-1:54:35.9	27.0 ± 0.39	139.4 ± 2.02
IRC044	5:41:43.55	-1:55:11.8	18.5 ± 0.13	95.3 ± 0.69
IRC153	5:41:44.75	-1:53:48.6	15.3 ± 0.39	78.9 ± 2.00
IRC215	5:41:36.24	-1:54:24.4	13.0 ± 0.15	67.2 ± 0.77
IRC036	5:41:44.18	-1:55:20.5	12.2 ± 0.38	63.0 ± 1.96
IRC133	5:41:42.55	-1:54:03.1	10.9 ± 0.14	56.3 ± 0.72
IRC128	5:41:45.07	-1:54:06.5	10.5 ± 0.17	54.1 ± 0.90
IRC033	5:41:44.41	-1:55:23.1	10.0 ± 0.43	51.5 ± 2.23
IRC058	5:41:44.25	-1:54:55.5	8.7 ± 0.13	45.1 ± 0.69
IRC124	5:41:42.54	-1:54:08.8	8.2 ± 0.35	42.5 ± 1.79
IRC123	5:41:41.64	-1:54:12.4	7.8 ± 0.14	40.4 ± 0.71
IRC158	5:41:40.64	-1:53:48.4	6.9 ± 0.14	35.7 ± 0.73
IRC197	5:41:43.49	-1:53:24.7	6.8 ± 0.14	35.3 ± 0.74
IRC090	5:41:43.25	-1:54:34.4	5.9 ± 0.14	30.2 ± 0.70
IRC180	5:41:40.19	-1:53:34.2	5.7 ± 0.15	29.1 ± 0.75
IRC115	5:41:42.80	-1:54:16.5	5.5 ± 0.14	28.2 ± 0.70
IRC160	5:41:42.61	-1:53:46.8	5.3 ± 0.14	27.4 ± 0.73
IRC059	5:41:45.04	-1:54:54.9	5.2 ± 0.17	26.8 ± 0.87
IRC165	5:41:41.71	-1:53:44.4	4.6 ± 0.14	23.5 ± 0.73
IRC208	5:41:42.34	-1:53:16.0	3.8 ± 0.15	19.7 ± 0.78
IRC175	5:41:44.39	-1:53:36.1	3.0 ± 0.15	15.4 ± 0.75
IRC150	5:41:43.92	-1:53:51.5	2.9 ± 0.14	15.0 ± 0.73
IRC116	5:41:38.23	-1:54:17.7	2.8 ± 0.14	14.6 ± 0.72
IRC144	5:41:36.82	-1:53:59.0	2.8 ± 0.14	14.5 ± 0.73
IRC057	5:41:45.73	-1:54:58.1	2.7 ± 0.50	13.8 ± 2.56
IRC184	5:41:41.35	-1:53:32.8	2.6 ± 0.14	13.4 ± 0.74
IRC120	5:41:39.20	-1:54:14.3	2.6 ± 0.14	13.2 ± 0.72
IRC236	5:41:44.21	-1:55:24.0	2.5 ± 0.18	12.9 ± 0.91
IRC143	5:41:43.56	-1:53:56.8	2.2 ± 0.14	11.3 ± 0.72

Table 5.1: continued.

Name	RA	Dec	Flux mJy	Mass $M_\oplus$
IRC206	5:41:42.89	-1:53:16.5	2.1 ± 0.15	11.0 ± 0.77
IRC089	5:41:43.89	-1:54:34.2	1.9 ± 0.34	9.8 ± 1.77
IRC081	5:41:37.75	-1:54:41.3	1.9 ± 0.13	9.8 ± 0.69
IRC103	5:41:41.98	-1:54:24.2	1.7 ± 0.14	9.0 ± 0.70
IRC119	5:41:36.68	-1:54:15.3	1.3 ± 0.14	6.7 ± 0.73
IRC168	5:41:44.12	-1:53:42.6	1.3 ± 0.14	6.5 ± 0.74
IRC170	5:41:43.85	-1:53:38.6	1.2 ± 0.14	6.3 ± 0.74
IRC032	5:41:44.33	-1:55:25.0	1.2 ± 0.19	6.2 ± 0.98
IRC093	5:41:45.63	-1:54:29.2	1.2 ± 0.36	6.0 ± 1.86
IRC080	5:41:42.77	-1:54:39.4	1.1 ± 0.13	5.7 ± 0.70
IRC077	5:41:43.03	-1:54:40.6	1.1 ± 0.14	5.5 ± 0.70
IRC121	5:41:43.46	-1:54:12.4	1.0 ± 0.14	5.1 ± 0.71
IRC131	5:41:44.23	-1:54:05.2	1.0 ± 0.14	5.1 ± 0.72
IRC199	5:41:36.30	-1:53:24.7	0.9 ± 0.15	4.8 ± 0.80
IRC115B	5:41:42.80	-1:54:16.5	0.8 ± 0.14	4.3 ± 0.71
IRC025	5:41:42.54	-1:55:37.6	0.8 ± 0.13	4.2 ± 0.65
IRC187	5:41:43.34	-1:53:30.2	0.8 ± 0.14	4.1 ± 0.74
IRC083	5:41:41.49	-1:54:39.4	0.7 ± 0.13	3.5 ± 0.69
IRC074	5:41:43.76	-1:54:41.8	0.7 ± 0.13	3.4 ± 0.70
IRC099	5:41:44.83	-1:54:25.3	0.6 ± 0.15	3.3 ± 0.78
IRC072	5:41:41.39	-1:54:44.7	0.6 ± 0.13	3.1 ± 0.69
IRC194	5:41:40.48	-1:53:27.3	0.6 ± 0.15	3.0 ± 0.77
IRC173	5:41:36.94	-1:53:39.5	0.6 ± 0.15	2.9 ± 0.75
IRC070	5:41:36.83	-1:54:48.1	0.6 ± 0.13	2.8 ± 0.69
IRC045	5:41:42.20	-1:55:10.1	0.5 ± 0.14	2.5 ± 0.70
IRC219	5:41:43.33	-1:55:07.0	0.5 ± 0.13	2.5 ± 0.70

5.3.2 Dust masses of NGC 2024 disks

If the continuum emission detected in the sample of protoplanetary disks studied here is optically thin, a simple relation exists between the mass (of millimeter-sized dust grains) of the disk and its flux (Equation 5.1). In Figure 5.2, the Kaplan-Meier estimator is used to infer the disk mass distribution for the full sample, including nondetections.

$$M_{\rm dust} = \frac{d^2 F_{\nu,\,\rm dust}}{\kappa_\nu B_\nu(T_{\rm eff})}. \tag{5.1}$$

In this article, we take the distance d to NGC 2024 to be 414 pc (Menten et al. 2007; Bailer-Jones et al. 2018). In order to facilitate the comparison of this sample of disks to other ALMA surveys of disks in star-forming regions (e.g. Ansdell et al. 2016; van Terwisga et al. 2019b), we use standard assumptions on the values of the other parameters in Eq. 5.1: $T_{\rm eff} = 20$ K (Andrews & Williams 2005), and $\kappa_\nu = \kappa_0\ (\nu/\nu_0)^\beta$ with $\beta = 1$ and $\kappa_{1000\,\rm GHz} = 10\,\rm cm^2\ g^{-1}$ (Beckwith et al. 1990).

The assumption that all disks are optically thin in Band 6 is currently a topic of active debate, and several results have indicated that along disks may be partly optically thick (Tri-

pathi et al. 2017; Andrews et al. 2018; Zhu et al. 2019), while it has also been suggested that the method used here can lead to the dust mass being overestimated (Rosotti et al. 2019). These effects are difficult to quantify even for well-studied disks. Since the primary purpose of these observations is to study how the continuum luminosity of a disk changes as the solids evolve over time, we therefore also show a flux axis (normalized to the distance of NGC 2024) in the disk mass distribution plots shown here, which is free from assumptions on opacities and optical depth.

Our use of the Kaplan-Meier estimator requires that the inclusion of an object in the catalog is not sensitive to its disk mass, that the sample is drawn from a single population, and that the probability of a nondetection does not depend on the variable studied (here, the disk mass). While the first of these criteria is met, the second does not necessarily hold, and we examine it further in Section 5.4.1. The third requirement is not met, and means these results should be interpreted carefully at the lower end of the mass range, where completeness begins to drop (Mohanty et al. 2013).

Impact of free-free emission

By using this equation, we implicitly assume no free-free emission contaminates our observations. In strongly irradiated star-forming environments, this assumption does not necessarily hold. Proplyds in the Trapezium cluster, for instance, have non-negligible contamination from free-free emission even in Band 6 based on observations at centimeter wavelengths (Mann et al. 2014; Eisner et al. 2018). However, this does not seem to be a significant concern in NGC 2024: Mann et al. (2015) found free-free emission to contribute only weakly to the flux of the majority of sources at 338.2 GHz. The contribution from free-free emission is 10% for the most contaminated object, IRC 065, which is out of the field covered here, and $< 1\%$ for the most contaminated sources that are also covered by this survey (IRC 101 and IRC 071). For these sources, any free-free emission should still be negligible in our observations also, assuming spectral indices of 2.3 for the dust and -0.1 for the free-free emission. While VLA data only exist for part of the field we observed with ALMA (roughly, the southeastern quarter), this is the part of the image with sources closest to IRS-2b.

Impact of midplane temperature variations

The use of a 20 K effective temperature for the disk midplane is also worth considering, even apart from the issue of optical depths. This value is an average effective midplane temperature originally found by fitting SEDs with disks models with 100 AU radii (Andrews & Williams 2005). As a result it may not be appropriate in regions where disks are compact due to external photoevaporation: such truncated disks tend to be better described by higher effective temperatures, as shown in (Eisner et al. 2018). Additionally, the ambient radiation field may have an impact on the disk temperature. These effects are difficult to constrain in these observations, but would both lead to an overestimate of the dust mass. The size of this effect is shown in Figure 5.2 for a 40 K effective midplane temperature, which is found to be an appropriate value for low-mass compact disks with a characteristic radius R_c of 25 AU in a grid of models in (Eisner et al. 2018).

Point sources without NIR counterparts

Twelve sources are clearly detected ($> 4.8\sigma$) but do not correspond to Class-II YSOs identified previously; we present a table of their positions and fluxes as Table 5.2. Cutouts of these

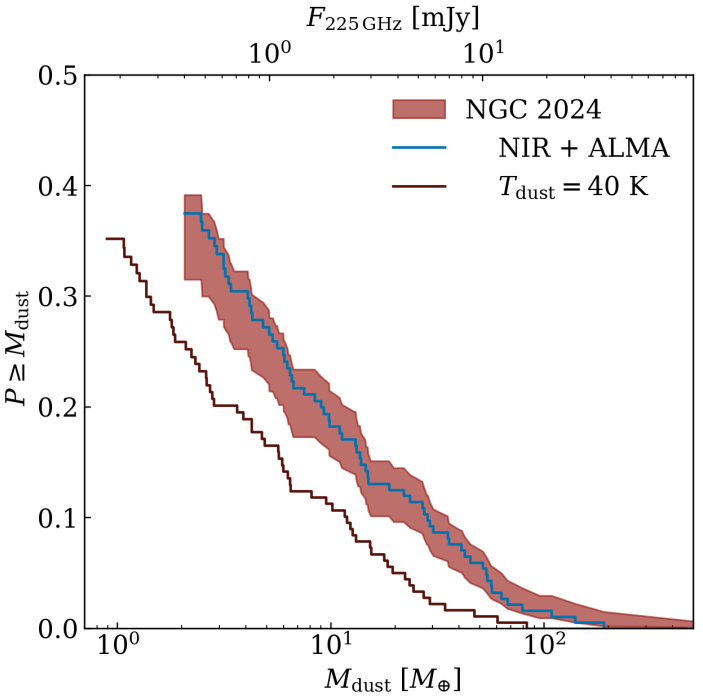

Figure 5.2: Inferred disk mass distribution for the NGC 2024 disk population (dark red). The effect of adding sources observed with ALMA but not detected in previous observations of NGC 2024, overlapping the Meyer (1996) catalog, and consistent with being Class II sources is shown in blue; the dark red line shows the effect of assuming a 40 K temperature for the sample.

sources can be found in Appendix 5.A, in Figure 5.A.3 The significance cut used here was chosen such that we expect less than one false positive given the number of independent beams in the full image (0.6 on average). These otherwise unidentified sources are marked in the overview map in Figure 5.1 with triangles. Of these sources, 10 overlap with the Meyer (1996) UKIRT survey. The remaining two sources (U12 and U13) are located in the northeast of the map, just above the dense molecular ridge hosting the FIR 1 - 4 sources.

Without an SED, determining the nature of these sources is difficult. Only one source, U13, corresponds to a MYSTiX catalog member (Povich et al. 2013). Several of the other sources not in the catalogue show interesting properties; they are discussed in more detail (along with the extraordinary IRC 101 transition disk) in Section 5.3.3. Some of these objects are clearly not Class-II sources; we have conservatively assumed that the rest of these objects are disks. By including those disks that fall in the original Meyer (1996) field in the sample, the detection rate is biased, but in an informative way: since it is unknown how many sources are missing in the catalog that are nondetections in ALMA, this is the highest possible value for the 'true' detection rate of disks in this area. If we As Figure 5.2 shows, this effect is small. The low number of new detections also implies that there is no large population of disks more massive than 3.6 $M_\oplus$ in the sample.

Table 5.2: Continuum fluxes for objects not included in the base catalog

Name	RA	Dec	Flux mJy	D
U1	0:22:47.02	-1:55:31.6	10.3 ± 0.80	Y
U2	0:22:47.01	-1:55:30.9	100.5 ± 1.65	N
U3	0:22:46.71	-1:55:07.3	8.4 ± 0.40	N
U4	0:22:46.51	-1:54:37.0	0.6 ± 0.13	Y
U5	0:22:46.87	-1:54:26.4	242.1 ± 0.41	N
U6	0:22:46.88	-1:54:25.4	11.0 ± 0.34	Y
U7	0:22:46.71	-1:54:07.6	1.4 ± 0.13	Y
U8	0:22:46.86	-1:53:43.5	1.6 ± 0.14	Y
U9	0:22:46.77	-1:53:38.2	1.8 ± 0.14	Y
U10	0:22:46.76	-1:53:32.8	3.8 ± 0.14	N
U11[a]	0:22:46.82	-1:53:07.6	41.3 ± 0.62	Y
U12[b]	0:22:46.93	-1:53:02.3	1.7 ± 0.33	Y

Notes. [(a)] Source not in the area covered by Meyer (1996)

Stacking analysis of nondetections

In total, 122 catalog objects across the image were not detected. By stacking all these sources, in theory, a S/N improvement of more than a factor of 10 can be achieved. The stacking analysis was performed by masking out the apertures containing detected sources in the full image, and taking the average (weighted by the local noise) of all positions not associated with a millimeter continuum source. The resulting image, shown in Figure 5.3 has a noise level of 6.66 μJy beam^{-1}. No source is detected in this stacked image. The resulting 3σ mass limit of the nondetected sources is 20 μJy, or $< 0.96\,M_{\rm Mars}$, implying that on average these disks will not be able to form even a single Mars-sized planet embryo from millimeter-sized grains currently present in the disk. However, this does not exclude the possibility that such bodies have already formed. This low upper limit is consistent with the disk mass distribution inferred in the region.

5.3.3 Comments on individual objects

Several objects in the observed field are of particular interest. Here, we discuss the continuum properties of the largest resolved disk in the sample. Several younger (Class 0) sources are also present in this sample and observed at higher resolutions that previously available. Finally, two compact sources of non-thermal emission are identified.

IRC 101: a 300 AU-radius dust ring around a YSO

Eisner & Carpenter (2003) and Mann et al. (2015) already identified this object as an extraordinarily bright YSO as millimeter wavelengths, and suggested that since the peak flux did not match the infrared catalogue positions precisely, its emission might originate from the envelope around a Class 0 protostar. Thanks to the excellent resolution of these ALMA observations, the source is revealed to have a morphology similar to that of 'classical' transition disks, with a well-defined inner cavity (Figure 5.4). Its size, however, remains extraordinary: assuming a 414 pc distance to NGC 2024 implies that the ring's peak intensity is at a radius

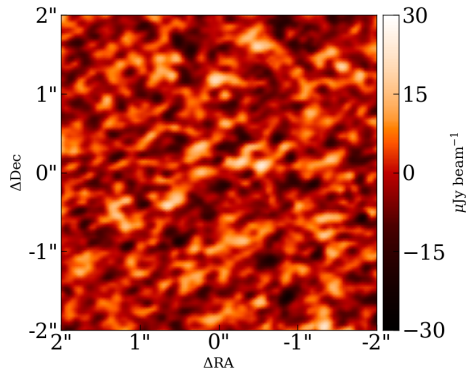

Figure 5.3: Noise-weighted stacked image of nondetections in the ALMA observations.

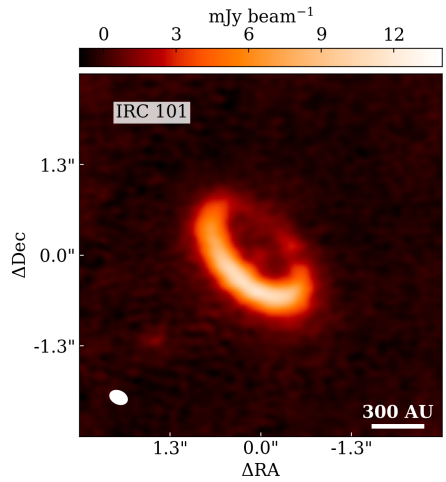

Figure 5.4: Zoomed-in panel from the full-baseline ALMA map of NGC 2024 showing an apparently asymmetric dust ring around IRC 101, resolved for the first time in these observations.

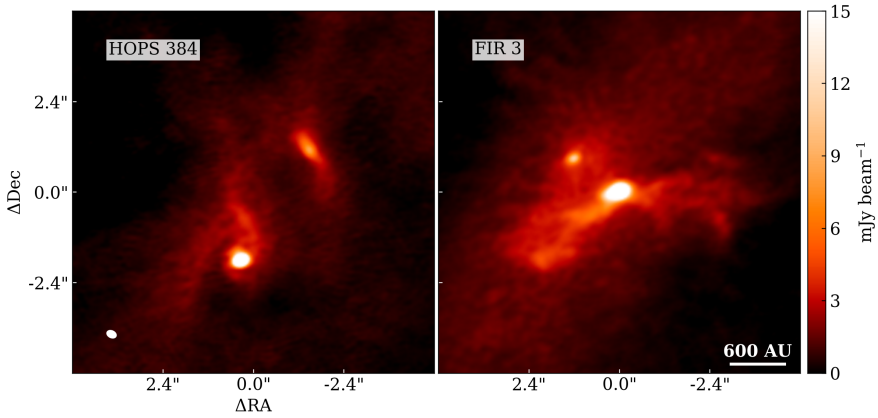

Figure 5.5: Zoomed-in panels from the full-baseline ALMA map of NGC 2024 showing two resolved, embedded objects with particularly interesting features. HOPS 384 (*left*) is a Class 0 protostar, here resolved as two, possibly interacting, YSOs. FIR 3 (*right*) is resolved for the first time in these observations, and shows two outflow cavity walls in 225 GHz continuum observations, as well as two compact continuum sources.

of ∼ 300 AU, making it the largest such object identified so far. An inner disk may be present, but is faint and unresolved. Give the size and depth of the cavity, which is well-resolved in these observations, IRC 101's disk is likely to host a multiple star system, rather than being carved by a planetary-mass companion. Additional evidence for this comes from the apparent asymmetry in the ring, which is noticeably brighter in the south than in the north. GG Tau A has circumternary dust ring with a peak radius 229 AU, and shows strikingly similar asymmetric continuum emission (Tang et al. 2016).

Unfortunately, the SED of this fascinating object is not well-sampled, due to the high optical extinction and its proximity on the sky to IRS 2b. However, the disk is detected in several channels in ^{13}CO (van Terwisga et al., in prep.) confirming that its proper motions are consistent with membership of NGC 2024 and excluding the possibility that this is a more compact foreground object.

NGC 2024 FIR 3

These observations also resolve for the first time a deeply embedded YSO, coincident with the location of NGC 2024 FIR 3, as well as a second continuum source nearby (Figure 5.5, bottom). Clearly, these sources (which lack counterparts in NIR observations) are young. The brightest source shows two approximately symmetric continuum structures which we here interpret as outflow cavity walls, extending over more than 1000 AU to either side and showing irregular, clumpy substructures. Interestingly, the continuum emission around this YSO seems to be somewhat resolved, and slightly elongated to the west. Previously, Ren & Li (2016) have suggested NGC 2024 FIR 3 may be a First Hydrostatic Core (FHSC). These observations are inconsistent with that hypothesis, given the resolved nature of the outflow cavity walls and central source (Young et al. 2019).

The HOPS-384 system

HOPS-384, shown in the top panel of Figure 5.5 is a known Class 0 protostar (Furlan et al. 2016). In these observations, we resolve it as two objects, both associated with significant extended continuum emission. The brightest source is in the south, and seems to be associated with two asymmetric, spiral-arm like curved arcs of dust. The fainter northern component has an elongated, s-like shape, and seems to coincide with an extended ridge of continuum emission, although the poor short baseline coverage of our observations prevents us from making this association more explicit. The northern source seems to be associated with more compact structures than the southern source. It is not clear if a physical link between the sources exist: certainly, the arcs seen in both sources are curved in the same direction.

IRS 2

IRS 2 is, like IRC 101, a prominent source at millimeter wavelengths. It is bright enough at Band 6 to test if it is emitting non-thermal radiation by calculating an intra-band spectral index. Using CASA's *clean* algorithm, α is found to be $\sim$ 0.3 for this source, indicative of free-free emission dominating the flux at these wavelengths. The uncertainty in this value is difficult to quantify, as it depends on the quality of the flux calibration in each spectral window. However, it should be internally consistent. Comparison to the IRC 101 ring, which has a spectral index of $\sim$ 2, shows that the relative spectral index of this object is certainly much lower than for a pure dust disk. The spectral index of $\sim$ 1.9 found in Mann et al. (2015) for IRS 2 indicates that our value of α may be too low, but it is also possible that contamination from extended dust emission in the (larger) SMA beam has led to an increase in the spectral index in that article. In any case, the free-free emission constitutes makes up a significant part of the disk emission even in the most pessimistic case. To be cautious, therefore, we do not include this source in the disk catalog.

A bright flaring object at 1.2 mm

Because of the observation schedule used, the full ALMA field was observed on multiple nights, allowing us to test if any objects showed signs of variability. This was indeed the case. J054141.3-015332, U10 in this catalog, shows signs of extreme variability on short ($\leq$ 24-hour) timescales. It is the brightest continuum source in the field on the first day of observing with a total flux of 176.9 $\pm$ 0.5 mJy, then fades by a factor 26 to 6.8 $\pm$ 0.36 mJy, and shows lower-amplitude flickering in the subsequent integrations, falling below the detection limit in the 5th and 8th full integrations, as shown in Table 5.3. Figure 5.6 shows the flux of the flaring source and the adjacent IRC 184, normalized to the second full integration. On the first full integration, the source is bright enough to attempt to determine its intra-band spectral index. At $\alpha \sim -0.7$, the emission is clearly non-thermal, although we reiterate the caveat that the flux calibration between spectral windows may not be accurate. However, the timescales on which the source shows variability are certainly inconsistent with the variability being dominated by blackbody emission, since they require emission from a very compact area. The finding of millimeter-variability for this source agrees with earlier observations finding that in X-rays, this source is also among the brightest X-ray-emitters in the region and may be variable (Skinner et al. 2003). The SED of the emitting source, however, is uncertain: due to the close proximity on the sky to IRC 184, it is not clear if the infrared excess is present in both sources, or in only IRC 184 or U11.

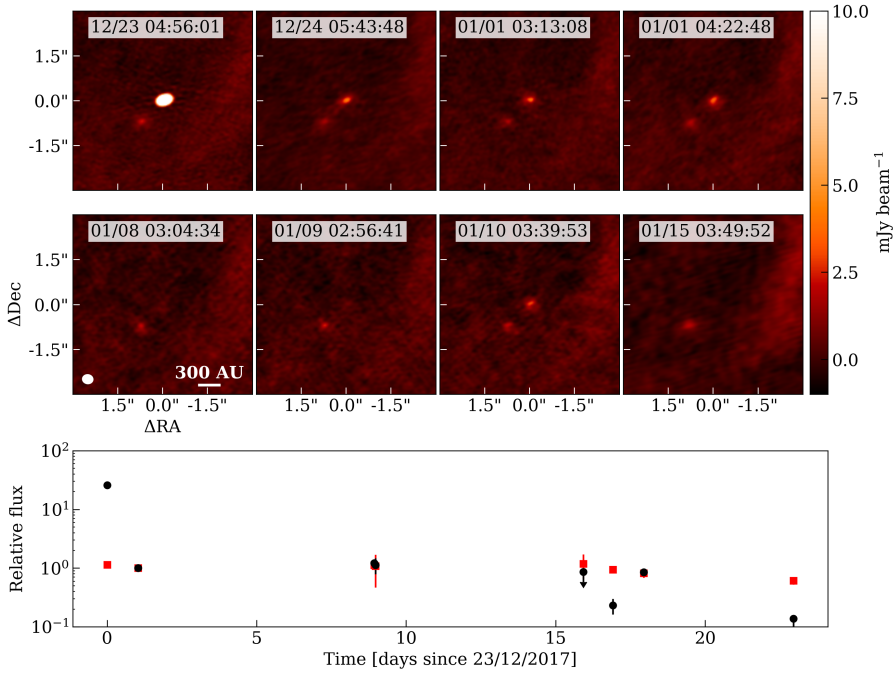

Figure 5.6: Time-resolved observations of a flaring YSO. *Top*: zoomed-in panels of the U11 source from individual integrations of the ALMA continuum show the source variability relative to IRC 184. *Bottom*: fluxes of both IRC 184 (red) and U11 (black), normalized to these objects' fluxes on the second full integration of the mosaic.

Table 5.3: Flux over time for J054141.3-015332, starting 12/23/2017

Day	Time	$F_{225\,GHz}$ mJy
12/23	04:56:01	176.9 ± 0.5
12/24	05:43:48	6.8 ± 0.4
01/01	03:13:08	8.3 ± 0.4
01/01	04:22:48	7.7 ± 2.31
01/08	03:04:34	< 5.9
01/09	02:56:41	1.6 ± 0.5
01/10	03:39:53	5.8 ± 0.5
01/15	03:49:52	< 0.9

5.4 Discussion

The primary goal of these observations was to improve our understanding of how disk properties vary across NGC 2024, and how they compare to those in other star-forming regions of different ages and with different (F)UV fields. In Section 5.4.1, we therefore define two subsamples and interpret their disk mass distributions in terms of the physical properties of NGC 2024.

5.4.1 Two disk populations across the NGC 2024 core region

The disk mass distribution in Figure 5.2 implicitly assumes a single population of disks is observed in this field. However, this assumption is not necessarily true, given the complex environment covered in these observations. IRS 2b's radiation field is important throughout the region, even in the vicinity of IRS 1 (Burgh et al. 2012), although the presence of large amounts of foreground extinction makes it less easy to observe than the Trapezium. Projected distances of YSOs in the catalog to IRS 2b range from 0.0057 pc to 0.36 pc. In the Trapezium cluster (O'Dell 2001; Abel et al. 2019), disk masses vary strongly across this distance range due to external photoionization. There, disks nearest to the ionizing source (θ^1 Ori C) have significantly lower masses (Mann et al. 2014; Eisner et al. 2018). A second reason that disk properties may vary across the ALMA image is an unequal distribution of interstellar material, which may attenuate ionizing radiation from the massive young stars (if sufficiently dense) or host very young populations. The area covered in this survey is dominated on the western side by the dense molecular ridge hosting the FIR sources (Watanabe & Mitchell 2008), while the eastern part seems to lack dense interstellar material. Finally, there is evidence of a core-halo age gradient in NGC 2024, with the youngest stars located in the cluster's core, but a rapid increase in age (from 0.2 to 1.1 Myr) in the inner 0.5 pc (Haisch et al. 2000; Getman et al. 2014). All these factors may influence disk masses over space within the observations presented here.

In Figure 5.1, where detections and nondetections are shown against both the ALMA data and Herschel PACS 160 μm contours (Stutz et al. 2013), the hypothesis that two distinct populations of disks are indeed present in this survey immediately suggests itself: targets located in the east, along the direction of the dense molecular ridge, seem to have a much higher detection rate than those in the west. This region also contains all known Class I and Class 0 sources in the field. The dividing line between these populations seems to lie on a mildly inclined north-south axis. To formally test this hypothesis, the sample was divided into two subsamples in a simple way. For both subsamples, the disk mass distribution was calculated separately in the manner described in 5.3.2. Using a log-rank test, we then tested if it is possible to reject the null hypothesis that there is no difference in disk masses between the samples. The subsamples are divided by a line between 5:41:44.189 -1°55'39.94" and 5:41:38.665 -1°53'00.27". The eastern subsample has $N = 97$; the southern $N = 82$. In observational terms, the dividing line is drawn along the 4 Jy pixel^{-1} contour in the 160 μm data, just to the south of the densest part of the ridge. The physical motivation for this division is that it should be tangent to the densest part of the molecular ridge containing the FIR 1–5 sources, and ensure all these sources are in one subsample. While this is to a certain extent arbitrary, we have tested that the final results are not sensitive to its position, and hold so long as the dividing line lies within 10° of the angle between these points, and less than 0.5′ to the west.

In Figure 5.7, the disk mass distributions of the resulting cut are shown. The log-rank

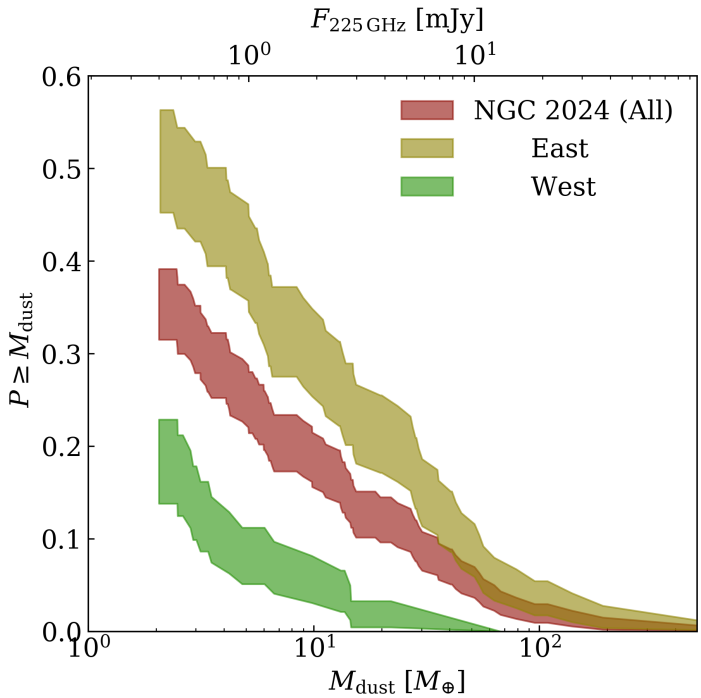

Figure 5.7: Inferred disk mass distribution for the NGC 2024 disk population (dark red) and the hypothesized western and eastern subpopulations, in tan and green respectively. The dividing line between these populations runs from 5:41:44.189 -1°55'39.94" and 5:41:38.665 -1°53'00.27", tangent to the southern part of the dense molecular ridge.

test indicates that these distributions are extremely unlikely to be drawn from the same population ($p = 2.0 \times 10^{-6}$). This is a striking result: the eastern population has the smallest projected distances to IRS 2b, but has significantly higher masses, and a detection rate of $45 \pm 7\%$. In contrast, only $15 \pm 4\%$ of disks in the western part of the image are detected. This is at odds with a view where only external photoevaporation determines disk mass in this region. Mann et al. (2015), who observed the eastern disk population with the SMA, similarly did not see evidence of external photoevaporation in that part of the nebula. It is therefore important to interpret this result in the context of previous observations of NGC 2024, in order to arrive at a more detailed view of the structure and history of this star-forming region.

Here, we propose that two effects contribute to the observed properties of the sample. To the east, we look towards a very young disk population, still mostly embedded in a dense molecular ridge, and quite distant from IRS 2b. To the west, the observed disks are not only older, but much more exposed to radiation from the ionizing source(s) and IRS 1, resulting in lower disk masses. This scenario is shown in Figure 5.8. This view builds on previous studies of NGC 2024's molecular environment using a blister model of expanding HII regions. In the current view, an optical dust bar is placed in front of the main ionizing sources along the line-of-sight. The massive stars in the cluster core excavate an expanding HII blister, impacting a dense ridge of cold molecular gas behind it (Giannini et al. 2000; Emprechtinger et al. 2009).

Our proposed young, eastern population would be located in and shielded by the dense ridge. Several YSOs in this region show clear signs of youth: FIR 3 has no NIR counterpart and visible outflow walls in millimeter-continuum observations, and HOPS-384 has been found to be a Class 0 source from previous SED fitting (Furlan et al. 2016). The ages of the stars with disks are also low in the cluster's core (Getman et al. 2014). In the Integral-Shaped Filament (ISF), the youngest sources are found to be clustered along the filament, while stars with disks are not (Kainulainen et al. 2017); but this region is likely to be somewhat older, and the dispersal of Class II disks takes time. We therefore suggest that these objects are young and still at least somewhat shielded by the dense molecular ridge in which they formed. This is also in agreement with the higher extinction values towards this region.

In the western population, the extinction along the line-of-sight is much lower. This population has both higher stellar ages (Getman et al. 2014) and a lower disk fraction (Haisch et al. 2000), which is in line with the expectation for a sample of stars that have been exposed to intense ionizing radiation fields for ~ 1 Myr. These observations reveal that disk masses in this part of the cluster are lower, too. It is interesting to note that while one or more stars near the position of IRS 2b still dominate the total FUV radiation budget in the nebula, the somewhat cooler B0.5 star IRS 1 contributes a significant amount of flux even at 1200 (Burgh et al. 2012). This may help increase the efficiency of external photoevaporation, if it is driven mainly by FUV irradiation of the disks in this part of the nebula. There is a degeneracy between the effects of region age and photoevaporation, as Figure 5.9 shows. Thus, the low disk masses in this region could also be explained by age alone. However, despite the large uncertainties inherent in YSO age estimates, the western population's disk masses most closely resemble the 6−−10 Myr-old Upper Sco disks (Barenfeld et al. 2016) (see Section 5.4.2), making it more likely that it is age together with external photoevaporation that causes the low observed disk masses.

The stark difference in disk masses between the two populations identified here indicates a complex star formation history. In particular, it is possible that the younger population is the result of a moving region of star formation as the HII bubble is carved out and compresses the gas behind it. The western population might then be the product of an earlier period of

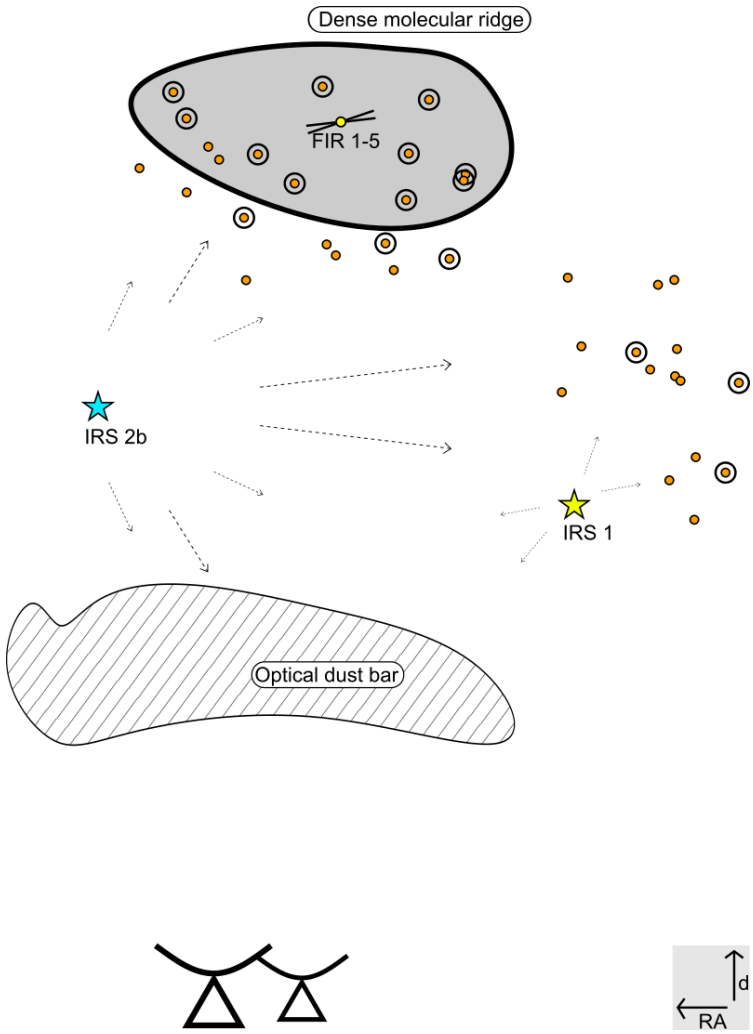

Figure 5.8: Schematic view of the young stellar populations in NGC 2024. Orange points are Class II stars; circles indicate mm-detections. The eastern population (left) is young and located near the dense molecular ridge hosting the FIR 1–5 Class 0 sources, which partly shields its from the intense radiation field driven by the ionizing source(s), such as IRS 2b. The western population is older, and more exposed to the ionizing radiation of the primary ionizing source(s) and the cooler IRS 1.

star formation. To formally test this, deep spectroscopic observations of the YSOs in the eastern sample, or covering a wider sample of NGC 2024 disks with ALMA are necessary.

The impact of uncertain stellar masses

The interpretation of the different disk masses in the eastern and western populations identified here is based on the assumption that there are no significant differences in the masses and multiplicities of the stars observed here. However, the higher extinction to the east would make it more difficult to detect lower-mass stars, in effect artificially biasing the stellar population to a higher average mass in the east. This is important: a clear correlation between disk mass (or luminosity) and stellar mass of the form $L_{\rm mm} \propto M_\star^{1.3--2.0}$ has been demonstrated in many nearby star-forming regions (Andrews et al. 2013; Pascucci et al. 2016). However, this relation may not hold in a region with significant photoevaporation. If NGC 2024 as a whole is like the ONC, we might not expect a strong dependence of $M_{\rm disk}$ with $M_\star$, or none at all (Eisner et al. 2018). However, it is not clear how well this result generalizes to other regions.

The catalog used to define this sample (Meyer 1996) is very deep (it samples stellar masses down to $0.1 M_\oplus$ viewed through $A_V = 19$), which helps minimize the problem of variable stellar masses, but not completely. More importantly, the scatter in $M_{\rm disk}$ vs $M_\oplus$ is generally very large, more than 1.5 dex, in nearby SFRs (Pascucci et al. 2016), which implies that we should detect at least some of the disks around even the lowest-mass stars. As discussed in Section 5.3.2, several objects that are consistent with being disks around stars missing from the catalog are in fact detected. However, there are only 6 such objects in the full map, and there does not seem to be a significant excess of these sources in the eastern part of the image, although this is difficult to say with such a low number of detections.

By adding a number of undetected sources to the eastern sample, and using the same statistical tests as before, we can try to constrain how many sources would need to be missing in the catalog in the eastern population only for the two populations to be identical in terms of disk masses. If we assume the eastern population is missing 70 detections (more than 30 nondetections for each detection without a counterpart in that part of the map), the samples still differ significantly ($p < 0.05$); and this ratio is far more than what is expected for disks drawn from a Lupus-like population of $0.1 M_\oplus$ stars (Ansdell et al. 2016; Pascucci et al. 2016). This suggests that any variations in stellar mass bias in the catalogue between the eastern and western populations are not likely to dominate the difference in these two populations; however, it does not mean that they are not present, and is an important caveat in the following.

5.4.2 Comparison to other star-forming regions

In Figure 5.9, the disk mass distributions of the two subpopulations are compared to those of other SFRs. The left panel shows three well-studied, nearby, low-mass regions, where external photoevaporation is not expected to be a major factor in disk evolution. In contrast, the panel on the right shows Class II disk masses in different environments in Orion A and B: the Trapezium and σ Orionis, where external photoevaporation has been shown to affect disk masses (Mann et al. 2014; Ansdell et al. 2017; Eisner et al. 2018), and the OMC-2 region, which is to the north of the Trapezium and where no evidence for external photoevaporation has been found (van Terwisga et al. 2019b). In this comparison, we cannot take into account possible differences in stellar masses, even though these may be significant, as discussed in Section 5.4.1, which is an important limitation. Similarly, the binarity fraction is important

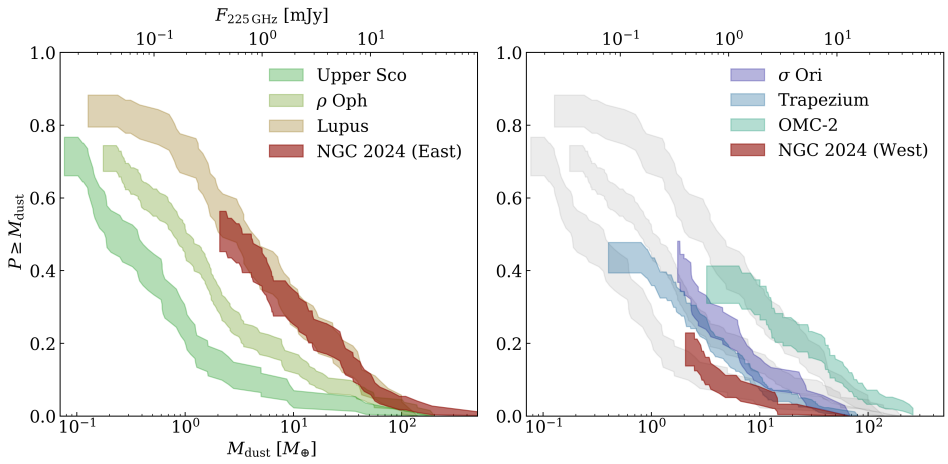

Figure 5.9: Disk mass distributions in NGC 2024 East (dark red) *(left)* and West (dark red) *(right)* compared to disk masses in other SFRs. Data for the low-mass regions was taken from Barenfeld et al. (2016) for Upper Sco, Pascucci et al. (2016) for Cham I, Ansdell et al. (2016) for Lupus. Disk masses across Orion are taken from Eisner et al. (2018) for the Trapezium, Ansdell et al. (2017) for σ Ori, and van Terwisga et al. (2019b) for OMC-2. Silhouettes in the right panel show the low-mass regions again, for comparison.

for disk masses: binary systems have lower total disk masses in Taurus (Akeson et al. 2019). However, for many regions including NGC 2024 the number of binary YSOs is not well-known, leading to additional uncertainty in the comparison of disk luminosities and masses.

NGC 2024 East

It is surprising how closely the disk mass distributions of Lupus and NGC 2024 East resemble each other; a log-rank test cannot distinguish between these populations. This is also true for the disks in Taurus and Chamaeleon I (Andrews et al. 2013; Pascucci et al. 2016). Within Orion, too, NGC 2024 East's disk mass distribution is indistinguishable from that in the OMC-2 cloud. All of these regions, are typically given ages of 1–3 Myr, older than NGC 2024. In contrast, the approximately $\sim$ 2 Myr-old ρ Oph star-forming region hosts a disk population that is markedly lower in mass than that of NGC 2024 East (Cieza et al. 2019; Williams et al. 2019). ρ Oph, however, may also host two populations of YSOs of different ages, although this older population should be small ($<$ 20% of the full stellar population) (Wilking et al. 2005).

The disk masses of NGC 2024 East lie significantly below those of Class I and Class 0 objects in Perseus and Orion (Tychoniec et al. 2018, Tobin et al., in prep). This is in line with the view that the evolution of disk masses does not proceed at a constant rate, and that Class 0 and Class I disks rapidly lose (millimeter-sized grain) luminosity, but do so only slowly once the Class II phase has been reached. In that case, the majority of solids evolution and planet formation occurs during the embedded phases of star formation, as suggested by the rich structures seen in HL Tau (ALMA Partnership et al. 2015), GY 91 (Sheehan & Eisner 2018), and other disks (van der Marel et al. 2019). This can be tested by further observations: in this scenario, other disk properties, such as their continuum radii and gas fluxes, should

also be similar in NGC 2024 and older regions.

NGC 2024 West

The low mass of the western sub-population of disks in this survey is remarkable, not just in contrast with the disks along the dense molecular ridge in the same region, but also when compared to ALMA observations of disk masses in other regions where external photoevaporation is important. Figure 5.9 shows NGC 2024 West next to three other star-forming regions in Orion, with different radiation fields. In van Terwisga et al. (2019b) it was shown that the OMC-2 population is apparently unaffected by external photoevaporation, due to its large distance from the Trapezium cluster. σ Ori is the oldest of the regions in this panel, at 3–5 Myr; while the signature of external photoevaporation is not as obvious, the ionizing star is cooler than those in NGC 2024 and the Trapezium, with a spectral type of O9. Of the lower-mass regions, NGC 2024 is most similar to the 6–10 Myr-old Upper Sco sample (Barenfeld et al. 2016). However, this age is at odds with existing age measurements towards the regions even when taking into account the uncertainties in stellar age determinations (Getman et al. 2014).

The Trapezium disks and those in NGC 2024 West cannot be distinguished by a log-rank test. NGC 2024 may in fact be less massive on average, but this would require deeper observations (or a larger sample) to test conclusively. This result is in line with the expectation that stars outside the cluster core are older than those in the inner region (which make up our NGC 2024 East sample), and have similar ages to the disks in the core of the Trapezium (Getman et al. 2014) within the uncertainties and scatter in stellar age estimates. However, NGC 2024 West disks are on average at least 0.25 pc from IRS 2b. In the Trapezium photoevaporation is much less important at this distance to θ^1 Ori C, the primary source of ionizing radiation (Mann et al. 2014; Eisner et al. 2018). As we suggested previously, this may be explained by the contribution of IRS 1 to the external photoevaporation. Alternatively, it is possible that disks in this population always had intrinsically lower masses than disks in the Trapezium, in a similar way to what has been proposed for disks in ρ Oph and R Corona Australis (Williams et al. 2019; Cazzoletti et al. 2019). The older population extends over a larger area than the part observed here (Getman et al. 2014). Thus, millimeter observations of disks in this part of the cluster may allow us to test this hypothesis.

5.5 Conclusions

In this article, we presented observations of a large field towards the center of NGC 2024, containing 179 protoplanetary disks, as well as several YSOs at earlier stages of evolution. The purpose of these observations was to characterize the disk masses in a young, massive star-forming region, and to use these to study how disk evolution is affected by the strong radiation fields and high stellar densities in such environments by comparing NGC 2024 to other regions. This comparison depends sensitively on our knowledge of the stellar populations of NGC 2024. By comparing CO velocity measurements with multi-wavelength surveys of YSOs and stellar ages, we can interpret the disk masses of the distinct populations in our field in a coherent way. This allows us to locate the Class II objects of NGC 2024 in the interstellar environment in much greater detail. In the future, a JWST GTO program towards this region (ID 1190, PI: M. Meyer) will allow us to constrain the properties of the stellar and substellar populations in greater detail, and to confirm the results shown here.

- 179 disks in NGC 2024 were observed with ALMA in Band 6, of which 31.84% are detected. Several other YSOs are detected, one of which is an X-ray source from which we detect a bright synchrotron flare.
- We identify two distinct populations of disks in NGC 2024: one in the eastern half of our field, centered on the dense molecular ridge hosting the FIR 1–5 sources, and one in the western half of the field.
- The eastern population is consistent with a 0.5 Myr age, has a significantly higher disk detection rate (45.3%), and contains the most massive object in the sample, the IRC 101 transition disk. In terms of disk mass distributions, it resembles both the Lupus and the OMC-2 disk populations.
- The western population in contrast has much fainter disks, with a detection rate of 15.9%. This population is likely older ($\sim$ 1 Myr) and exposed to external FUV irradiation from IRS 2b and IRS 1, leading to rapid external photoevaporation.

Appendix

5.A Cutouts of detected sources

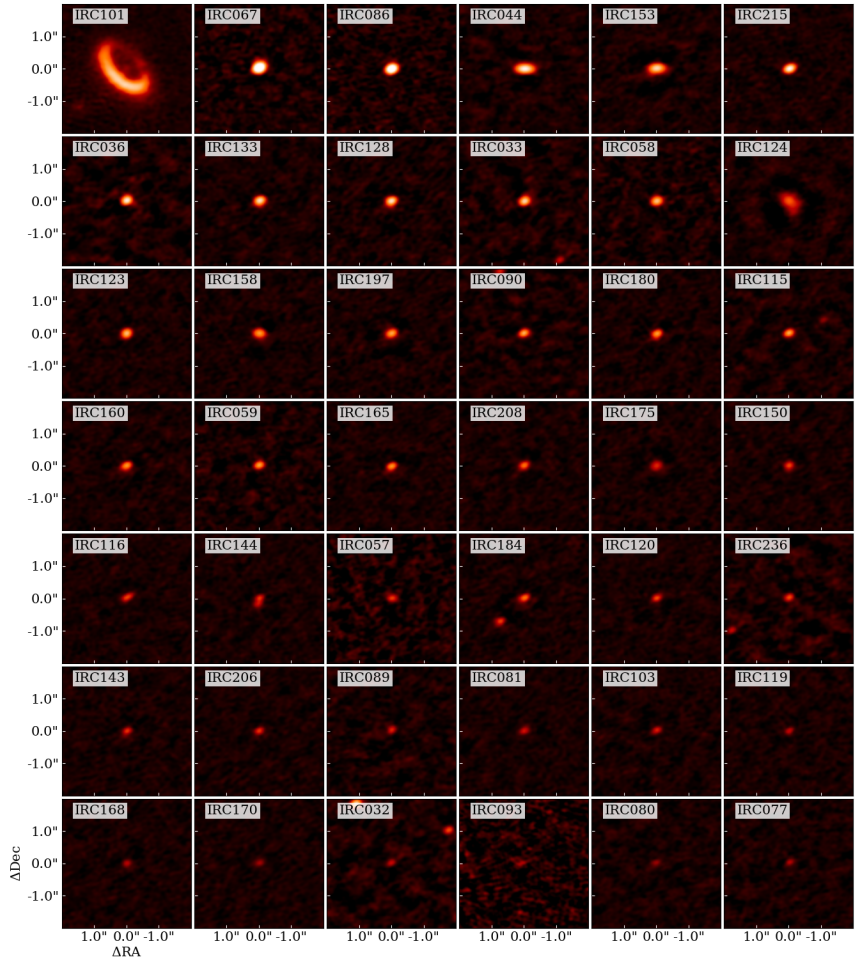

Figure 5.A.1: Cutouts of the disks in the Meyer (1996) catalog detected in this study, sorted by integrated flux.

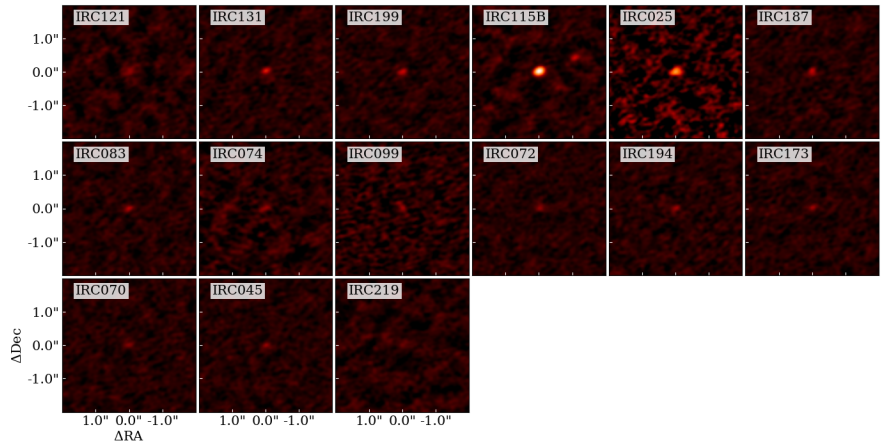

Figure 5.A.2: Cutouts of the disks in the Meyer (1996) catalog detected in this study, sorted by integrated flux, continued from Figure 5.A.1.

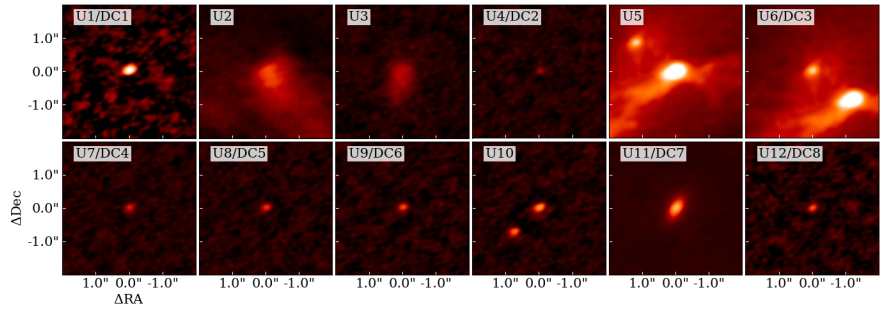

Figure 5.A.3: Cutouts of detected sources without counterparts in the Meyer (1996) catalog detected in this study, sorted by integrated flux. Sources considered disk candidates are marked as DC 1–8.

5.B Flux and mass upper limits for undetected disks

Table 5.B.1: 3σ continuum flux and mass upper limits for the nondetected disks

Name	RA	Dec	Flux mJy	Mass $M_\oplus$
IRC156	5:41:46.24	-1:53:48.0	< 21.1	< 108.5
IRC114	5:41:46.20	-1:54:14.7	< 7.9	< 40.9
IRC167	5:41:46.18	-1:53:42.5	< 5.5	< 28.4
IRC027	5:41:38.22	-1:55:38.0	< 4.3	< 21.9
IRC053	5:41:46.04	-1:55:02.2	< 3.9	< 20.0
IRC042	5:41:35.01	-1:55:19.8	< 3.6	< 18.7
IRC115A	5:41:35.03	-1:53:29.3	< 3.2	< 16.6
IRC106	5:41:45.62	-1:54:21.3	< 2.9	< 14.9
IRC161	5:41:45.98	-1:53:45.4	< 2.9	< 14.7
IRC212	5:41:35.16	-1:53:12.0	< 2.7	< 13.7
IRC122	5:41:45.91	-1:54:12.6	< 2.5	< 13.0
IRC127	5:41:45.80	-1:54:06.8	< 1.6	< 8.4
IRC102	5:41:45.17	-1:54:22.8	< 1.5	< 7.5
IRC050	5:41:45.73	-1:55:04.6	< 1.4	< 7.5
IRC063	5:41:45.72	-1:54:49.6	< 1.2	< 6.4
IRC098	5:41:45.68	-1:54:26.1	< 1.2	< 6.2
IRC113	5:41:35.39	-1:54:19.4	< 1.2	< 6.0
IRC169	5:41:35.34	-1:53:42.0	< 1.2	< 6.0
IRC190	5:41:35.43	-1:53:31.8	< 1.1	< 5.9
IRC205	5:41:36.55	-1:53:19.0	< 1.1	< 5.8
IRC188	5:41:43.94	-1:53:29.2	< 1.1	< 5.6
IRC147	5:41:40.15	-1:53:56.0	< 1.1	< 5.5
IRC155	5:41:35.45	-1:53:50.8	< 1.0	< 5.3
IRC029	5:41:38.05	-1:55:31.0	< 1.0	< 5.3
IRC139	5:41:45.42	-1:53:57.8	< 0.8	< 4.3
IRC047	5:41:44.02	-1:55:08.8	< 0.8	< 4.1
IRC176	5:41:45.36	-1:53:34.5	< 0.8	< 4.1
IRC052	5:41:45.36	-1:55:02.6	< 0.7	< 3.8
IRC162	5:41:35.72	-1:53:47.7	< 0.7	< 3.4
IRC110	5:41:35.72	-1:54:22.7	< 0.7	< 3.4
IRC073	5:41:44.90	-1:54:42.5	< 0.6	< 3.1
IRC034	5:41:44.41	-1:55:23.1	< 0.6	< 3.1
IRC177	5:41:35.85	-1:53:38.2	< 0.6	< 3.0
IRC193	5:41:43.50	-1:53:24.9	< 0.5	< 2.7
IRC040	5:41:44.17	-1:55:19.8	< 0.5	< 2.7
IRC213	5:41:37.85	-1:53:11.3	< 0.5	< 2.6
IRC117	5:41:43.16	-1:54:13.9	< 0.5	< 2.6
IRC118	5:41:41.65	-1:54:12.5	< 0.5	< 2.6
IRC092	5:41:42.66	-1:54:30.1	< 0.5	< 2.5
IRC134	5:41:44.93	-1:54:02.1	< 0.5	< 2.5
IRC209	5:41:41.84	-1:53:13.1	< 0.5	< 2.5

Table 5.B.1: (continued.)

Name	RA	Dec	Flux mJy	Mass $M_\oplus$
IRC112	5:41:36.13	-1:54:18.5	< 0.5	< 2.5
IRC225	5:41:36.25	-1:53:33.5	< 0.5	< 2.5
IRC035	5:41:40.25	-1:55:21.9	< 0.5	< 2.4
IRC210	5:41:37.34	-1:53:13.5	< 0.5	< 2.4
IRC207	5:41:41.40	-1:53:16.0	< 0.5	< 2.4
IRC204	5:41:38.54	-1:53:17.7	< 0.4	< 2.3
IRC174	5:41:36.37	-1:53:40.1	< 0.4	< 2.3
IRC186	5:41:38.25	-1:53:33.7	< 0.4	< 2.3
IRC202	5:41:43.17	-1:53:17.7	< 0.4	< 2.3
IRC107	5:41:44.72	-1:54:19.9	< 0.4	< 2.3
IRC041	5:41:40.63	-1:55:19.9	< 0.4	< 2.3
IRC189	5:41:40.05	-1:53:29.7	< 0.4	< 2.3
IRC192	5:41:38.31	-1:53:28.6	< 0.4	< 2.3
IRC164	5:41:36.38	-1:53:48.5	< 0.4	< 2.3
IRC203	5:41:37.94	-1:53:18.9	< 0.4	< 2.3
IRC195	5:41:39.47	-1:53:26.6	< 0.4	< 2.3
IRC201	5:41:39.31	-1:53:23.1	< 0.4	< 2.3
IRC198	5:41:38.15	-1:53:24.2	< 0.4	< 2.3
IRC231	5:41:44.72	-1:54:32.0	< 0.4	< 2.3
IRC200	5:41:38.69	-1:53:23.5	< 0.4	< 2.3
IRC224	5:41:36.76	-1:53:36.4	< 0.4	< 2.3
IRC039	5:41:38.21	-1:55:19.6	< 0.4	< 2.3
IRC163	5:41:37.57	-1:53:47.9	< 0.4	< 2.2
IRC183	5:41:39.55	-1:53:35.4	< 0.4	< 2.2
IRC138	5:41:44.55	-1:53:58.5	< 0.4	< 2.2
IRC152	5:41:37.82	-1:53:51.1	< 0.4	< 2.2
IRC178	5:41:40.04	-1:53:36.9	< 0.4	< 2.2
IRC191	5:41:41.41	-1:53:28.3	< 0.4	< 2.2
IRC159	5:41:36.54	-1:53:50.3	< 0.4	< 2.2
IRC182	5:41:41.12	-1:53:32.8	< 0.4	< 2.2
IRC172	5:41:44.21	-1:53:37.9	< 0.4	< 2.2
IRC146	5:41:38.10	-1:53:56.9	< 0.4	< 2.2
IRC171	5:41:40.00	-1:53:40.5	< 0.4	< 2.2
IRC148	5:41:39.02	-1:53:54.6	< 0.4	< 2.2
IRC149	5:41:36.63	-1:53:56.2	< 0.4	< 2.2
IRC181	5:41:43.32	-1:53:32.5	< 0.4	< 2.2
IRC157	5:41:44.10	-1:53:46.3	< 0.4	< 2.2
IRC145	5:41:39.05	-1:53:58.2	< 0.4	< 2.2
IRC135	5:41:36.46	-1:54:04.5	< 0.4	< 2.2
IRC185	5:41:42.11	-1:53:32.1	< 0.4	< 2.2
IRC151	5:41:41.47	-1:53:52.8	< 0.4	< 2.2
IRC179	5:41:41.71	-1:53:34.7	< 0.4	< 2.2
IRC166	5:41:41.96	-1:53:44.9	< 0.4	< 2.2
IRC141	5:41:41.45	-1:53:57.9	< 0.4	< 2.2

Table 5.B.1: (continued.)

Name	RA	Dec	Flux mJy	Mass $M_\oplus$
IRC136	5:41:39.33	-1:54:01.8	< 0.4	< 2.2
IRC130	5:41:36.72	-1:54:07.5	< 0.4	< 2.2
IRC126	5:41:39.00	-1:54:09.0	< 0.4	< 2.2
IRC132	5:41:43.97	-1:54:02.6	< 0.4	< 2.2
IRC140	5:41:43.13	-1:53:56.0	< 0.4	< 2.2
IRC111	5:41:37.47	-1:54:18.7	< 0.4	< 2.1
IRC129	5:41:40.20	-1:54:07.5	< 0.4	< 2.1
IRC223	5:41:38.33	-1:54:19.9	< 0.4	< 2.1
IRC125	5:41:40.93	-1:54:08.2	< 0.4	< 2.1
IRC108	5:41:44.31	-1:54:20.4	< 0.4	< 2.1
IRC082	5:41:36.51	-1:54:41.5	< 0.4	< 2.1
IRC104	5:41:38.39	-1:54:26.0	< 0.4	< 2.1
IRC222	5:41:41.88	-1:54:20.8	< 0.4	< 2.1
IRC097	5:41:38.77	-1:54:28.3	< 0.4	< 2.1
IRC226	5:41:37.61	-1:54:25.5	< 0.4	< 2.1
IRC054	5:41:42.46	-1:55:02.8	< 0.4	< 2.1
IRC043	5:41:41.46	-1:55:13.4	< 0.4	< 2.1
IRC051	5:41:42.14	-1:55:05.8	< 0.4	< 2.1
IRC230	5:41:42.37	-1:54:59.3	< 0.4	< 2.1
IRC069	5:41:42.59	-1:54:47.2	< 0.4	< 2.1
IRC100	5:41:37.81	-1:54:28.1	< 0.4	< 2.1
IRC055	5:41:41.81	-1:55:01.6	< 0.4	< 2.1
IRC087	5:41:43.97	-1:54:37.7	< 0.4	< 2.1
IRC216	5:41:43.69	-1:54:37.1	< 0.4	< 2.1
IRC075	5:41:42.75	-1:54:43.1	< 0.4	< 2.1
IRC076	5:41:43.65	-1:54:39.7	< 0.4	< 2.1
IRC084	5:41:41.36	-1:54:38.0	< 0.4	< 2.1
IRC088	5:41:42.78	-1:54:37.2	< 0.4	< 2.1
IRC091	5:41:38.09	-1:54:33.7	< 0.4	< 2.1
IRC094	5:41:37.90	-1:54:32.8	< 0.4	< 2.1
IRC079	5:41:41.60	-1:54:41.3	< 0.4	< 2.1
IRC214	5:41:37.71	-1:54:33.5	< 0.4	< 2.1
IRC048	5:41:37.81	-1:55:09.4	< 0.4	< 2.1
IRC061	5:41:38.19	-1:54:55.2	< 0.4	< 2.1
IRC078	5:41:39.50	-1:54:40.9	< 0.4	< 2.1
IRC233	5:41:37.76	-1:54:39.0	< 0.4	< 2.1
IRC056	5:41:39.00	-1:55:01.3	< 0.4	< 2.1

Bibliography

Abel, N. P., Ferland, G. J., & O'Dell, C. R. 2019, arXiv e-prints, arXiv:1906.07779

Adams, F. C. 2010, ARA&A, 48, 47

Adams, F. C., Lada, C. J., & Shu, F. H. 1987, ApJ, 312, 788

Adams, F. C. & Shu, F. H. 1986, ApJ, 308, 836

Aikawa, Y., Furuya, K., Nomura, H., & Qi, C. 2015, ApJ, 807, 120

Akeson, R. L., Jensen, E. L. N., Carpenter, J., et al. 2019, ApJ, 872, 158

Alcalá, J. M., Manara, C. F., Natta, A., et al. 2017, A&A, 600, A20

Alcalá, J. M., Natta, A., Manara, C. F., et al. 2014, A&A, 561, A2

ALMA Partnership, Asayama, S., Biggs, A., et al. 2017, ALMA Cycle 5 Technical Handbook, 5th edn.

ALMA Partnership, Brogan, C. L., Pérez, L. M., et al. 2015, ApJ, 808, L3

Andre, P., Ward-Thompson, D., & Barsony, M. 1993, ApJ, 406, 122

Andrews, S. M., Huang, J., Pérez, L. M., et al. 2018, ApJ, 869, L41

Andrews, S. M., Rosenfeld, K. A., Kraus, A. L., & Wilner, D. J. 2013, ApJ, 771, 129

Andrews, S. M. & Williams, J. P. 2005, ApJ, 631, 1134

Andrews, S. M., Wilner, D. J., Espaillat, C., et al. 2011, ApJ, 732, 42

Andrews, S. M., Wilner, D. J., Hughes, A. M., Qi, C., & Dullemond, C. P. 2010, ApJ, 723, 1241

Andrews, S. M., Wilner, D. J., Zhu, Z., et al. 2016a, ApJ, 820, L40

Andrews, S. M., Wilner, D. J., Zhu, Z., et al. 2016b, ApJ, 820, L40

Ansdell, M., Williams, J. P., Manara, C. F., et al. 2017, AJ, 153, 240

Ansdell, M., Williams, J. P., Trapman, L., et al. 2018, ApJ, 859, 21

Ansdell, M., Williams, J. P., van der Marel, N., et al. 2016, ApJ, 828, 46

Ardila, D. R., Herczeg, G. J., Gregory, S. G., et al. 2013, The Astrophysical Journal Supplement Series, 207, 1

Arulanantham, N., France, K., Hoadley, K., et al. 2018, ApJ, 855, 98

Avenhaus, H., Quanz, S. P., Garufi, A., et al. 2018, ApJ, 863, 44

Bailer-Jones, C. A. L., Rybizki, J., Fouesneau, M., Mantelet, G., & Andrae, R. 2018, AJ, 156, 58

Banzatti, A., Pinilla, P., Ricci, L., et al. 2015, ApJ, 815, L15

Barenfeld, S. A., Carpenter, J. M., Ricci, L., & Isella, A. 2016, ApJ, 827, 142

Barnard, E. E. 1919, ApJ, 49, 1

Barnard, E. E. 1927, Catalogue of 349 dark objects in the sky (University of Chicago Press)

Baruteau, C., Crida, A., Paardekooper, S. J., et al. 2014, in Protostars and Planets VI, ed. H. Beuther, R. S. Klessen, C. P. Dullemond, & T. Henning, 667

Beckwith, S. V. W., Sargent, A. I., Chini, R. S., & Guesten, R. 1990, AJ, 99, 924

Bell, C. P. M., Mamajek, E. E., & Naylor, T. 2015, MNRAS, 454, 593

Benz, W., Ida, S., Alibert, Y., Lin, D., & Mordasini, C. 2014, in Protostars and Planets VI, ed. H. Beuther, R. S. Klessen, C. P. Dullemond, & T. Henning, 691

Bergin, E., Calvet, N., Sitko, M. L., et al. 2004, ApJ, 614, L133

Bergin, E. A., Cleeves, L. I., Gorti, U., et al. 2013, Nature, 493, 644

Bergin, E. A., Du, F., Cleeves, L. I., et al. 2016, ApJ, 831, 101

Bik, A., Lenorzer, A., Kaper, L., et al. 2003, A&A, 404, 249

Birnstiel, T., Ricci, L., Trotta, F., et al. 2010, A&A, 516, L14

Bowler, B. P. 2016, PASP, 128, 102001

Bruderer, S. 2013, A&A, 559, A46

Bruderer, S., van Dishoeck, E. F., Doty, S. D., & Herczeg, G. J. 2012, A&A, 541, A91

Burgh, E. B., France, K., & Snow, T. P. 2012, ApJ, 756, L6

Bustamante, I., Merín, B., Ribas, Á., et al. 2015, A&A, 578, A23

Calvet, N., Briceño, C., Hernández, J., et al. 2005, AJ, 129, 935

Calvet, N., Muzerolle, J., Briceño, C., et al. 2004, AJ, 128, 1294

Carney, M. T., Hogerheijde, M. R., Loomis, R. A., et al. 2017, A&A, 605, A21

Carney, M. T., Yıldız, U. A., Mottram, J. C., et al. 2016, A&A, 586, A44

Carpenter, J. M. 2000, AJ, 120, 3139

Carpenter, J. M., Mamajek, E. E., Hillenbrand, L. A., & Meyer, M. R. 2006, ApJ, 651, L49

Cazzoletti, P., Manara, C. F., Baobab Liu, H., et al. 2019, A&A, 626, A11

Cazzoletti, P., van Dishoeck, E. F., Visser, R., Facchini, S., & Bruderer, S. 2018, A&A, 609, A93

Churchwell, E., Felli, M., Wood, D. O. S., & Massi, M. 1987, ApJ, 321, 516

Cieza, L. A., Casassus, S., Pérez, S., et al. 2017, ApJ, 851, L23

Cieza, L. A., Casassus, S., Tobin, J., et al. 2016, Nature, 535, 258

Cieza, L. A., Ruíz-Rodríguez, D., Hales, A., et al. 2019, MNRAS, 482, 698

Cieza, L. A., Ruíz-Rodríguez, D., Hales, A., et al. 2018, MNRAS, 2538

Cleeves, L. I., Öberg, K. I., Wilner, D. J., et al. 2016, ApJ, 832, 110

Codella, C., Cabrit, S., Gueth, F., et al. 2014, A&A, 568, L5

Comerón, F. 2008a, The Lupus Clouds, Vol. 5 (Astronomical Society of the Pacific Monograph Publications), 295

Comerón, F. 2008b, in Handbook of Star Forming Regions, Volume II: The Southern Sky ASP Monograph Publications, Vol. 5. Edited by Bo Reipurth, p.295, ed. B. Reipurth (The Southern Sky ASP Monograph Publications), 295

Concha-Ramírez, F., Vaher, E., & Portegies Zwart, S. 2019, MNRAS, 482, 732

Cutri, R. M., Skrutskie, M. F., van Dyk, S., et al. 2003, VizieR Online Data Catalog, 2246

Dai, Y., Wilner, D. J., Andrews, S. M., & Ohashi, N. 2010, AJ, 139, 626

Dicker, S. R., Mason, B. S., Korngut, P. M., et al. 2009, ApJ, 705, 226

Dipierro, G., Ricci, L., Pérez, L., et al. 2018, MNRAS[arXiv:1801.05812]

Draine, B. T. 2006, ApJ, 636, 1114

Ducourant, C., Teixeira, R., Galli, P. A. B., et al. 2014, A&A, 563, A121

Dullemond, C. P., Birnstiel, T., Huang, J., et al. 2018, ApJ, 869, L46

Dullemond, C. P. & Dominik, C. 2005, A&A, 434, 971

Dunham, M. M., Allen, L. E., Evans, Neal J., I., et al. 2015, ApJS, 220, 11

Dutrey, A., Guilloteau, S., & Guelin, M. 1997, A&A, 317, L55

Eisner, J. A., Arce, H. G., Ballering, N. P., et al. 2018, ApJ, 860, 77

Eisner, J. A. & Carpenter, J. M. 2003, ApJ, 598, 1341

Eisner, J. A., Plambeck, R. L., Carpenter, J. M., et al. 2008, ApJ, 683, 304

Emprechtinger, M., Wiedner, M. C., Simon, R., et al. 2009, A&A, 496, 731

Espaillat, C., Muzerolle, J., Najita, J., et al. 2014, Protostars and Planets VI, 497

Evans, Neal J., I., Allen, L. E., Blake, G. A., et al. 2003, PASP, 115, 965

Facchini, S., Birnstiel, T., Bruderer, S., & van Dishoeck, E. F. 2017, A&A, 605, A16

Favre, C., Cleeves, L. I., Bergin, E. A., Qi, C., & Blake, G. A. 2013, ApJ, 776, L38

Fedele, D., Carney, M., Hogerheijde, M. R., et al. 2017a, A&A, 600, A72

Fedele, D., Carney, M., Hogerheijde, M. R., et al. 2017b, A&A, 600, A72

Fedele, D., Tazzari, M., Booth, R., et al. 2018, A&A, 610, A24

Felli, M., Churchwell, E., Wilson, T. L., & Taylor, G. B. 1993, A&AS, 98, 137

Flock, M., Ruge, J. P., Dzyurkevich, N., et al. 2015, A&A, 574, A68

France, K., Schindhelm, E., Bergin, E. A., Roueff, E., & Abgrall, H. 2014, ApJ, 784, 127

Friesen, R. K., Pineda, J. E., co-PIs, et al. 2017, ApJ, 843, 63

Furlan, E., Fischer, W. J., Ali, B., et al. 2016, ApJS, 224, 5

Gagné, J., Mamajek, E. E., Malo, L., et al. 2018, ApJ, 856, 23

Gaia Collaboration, Brown, A. G. A., Vallenari, A., et al. 2018, A&A, 616, A1

Getman, K. V., Feigelson, E. D., & Kuhn, M. A. 2014, ApJ, 787, 109

Getman, K. V., Flaccomio, E., Broos, P. S., et al. 2005, ApJS, 160, 319

Giannini, T., Nisini, B., Lorenzetti, D., et al. 2000, A&A, 358, 310

Ginsburg, A., Bally, J., Goddi, C., Plambeck, R., & Wright, M. 2018, ApJ, 860, 119

Großschedl, J. E., Alves, J., Teixeira, P. S., et al. 2019, A&A, 622, A149

Guidi, G., Tazzari, M., Testi, L., et al. 2016, A&A, 588, A112

Guilloteau, S., Di Folco, E., Dutrey, A., et al. 2013, A&A, 549, A92

Guilloteau, S. & Dutrey, A. 1998, A&A, 339, 467

Guilloteau, S., Reboussin, L., Dutrey, A., et al. 2016, A&A, 592, A124

Guilloteau, S., Simon, M., Piétu, V., et al. 2014, A&A, 567, A117

Hacar, A., Tafalla, M., Forbrich, J., et al. 2018, A&A, 610, A77

Haisch, Karl E., J., Lada, E. A., & Lada, C. J. 2000, AJ, 120, 1396

Haisch, Karl E., J., Lada, E. A., & Lada, C. J. 2001, ApJ, 553, L153

Hartmann, L., Calvet, N., Gullbring, E., & D'Alessio, P. 1998, ApJ, 495, 385

Hartmann, L., Herczeg, G., & Calvet, N. 2016, ARA&A, 54, 135

Hartmann, L. & Kenyon, S. J. 1985, ApJ, 299, 462

Harvey, P. M., Huard, T. L., Jørgensen, J. K., et al. 2008, ApJ, 680, 495

Haworth, T. J., Clarke, C. J., Rahman, W., Winter, A. J., & Facchini, S. 2018, MNRAS, 481, 452

Haworth, T. J., Facchini, S., Clarke, C. J., & Cleeves, L. I. 2017, MNRAS, 468, L108

Heays, A. N., Bosman, A. D., & van Dishoeck, E. F. 2017, A&A, 602, A105

Henning, T. & Semenov, D. 2013, Chemical Reviews, 113, 9016

Herczeg, G. J., Walter, F. M., Linsky, J. L., et al. 2005, AJ, 129, 2777

Herczeg, G. J., Wood, B. E., Linsky, J. L., Valenti, J. A., & Johns-Krull, C. M. 2004, ApJ, 607, 369

Hily-Blant, P., Magalhaes, V., Kastner, J., et al. 2017, A&A, 603, L6

Hollenbach, D. J., Yorke, H. W., & Johnstone, D. 2000, in Protostars and Planets IV, ed. V. Mannings, A. P. Boss, & S. S. Russell, 401–428

Huang, J., Andrews, S. M., Pérez, L. M., et al. 2018, ApJ, 869, L43

Huang, J., Öberg, K. I., Qi, C., et al. 2017, ApJ, 835, 231

Isella, A., Guidi, G., Testi, L., et al. 2016, Physical Review Letters, 117, 251101

Isobe, T., Feigelson, E. D., & Nelson, P. I. 1986, ApJ, 306, 490

Joergens, V., Guenther, E., Neuhäuser, R., Fernández, M., & Vijapurkar, J. 2001, A&A, 373, 966

Joy, A. H. 1945, ApJ, 102, 168

Kainulainen, J., Stutz, A. M., Stanke, T., et al. 2017, A&A, 600, A141

Kama, M., Bruderer, S., van Dishoeck, E. F., et al. 2016a, A&A, 592, A83

Kama, M., Bruderer, S., van Dishoeck, E. F., et al. 2016b, A&A, 592, A83

Kandori, R., Tamura, M., Kusakabe, N., et al. 2007, Publications of the Astronomical Society of Japan, 59, 487

Kastner, J. H., Hily-Blant, P., Rodriguez, D. R., Punzi, K., & Forveille, T. 2014, ApJ, 793, 55

Kastner, J. H., Qi, C., Gorti, U., et al. 2015, ApJ, 806, 75

Kenyon, S. J., Gómez, M., & Whitney, B. A. 2008, Low Mass Star Formation in the Taurus-Auriga Clouds, Vol. 4 (Astronomical Society of the Pacific Monograph Publications), 405

Kenyon, S. J. & Hartmann, L. 1987, ApJ, 323, 714

Lada, C. J. 1987, in IAU Symposium, Vol. 115, Star Forming Regions, ed. M. Peimbert & J. Jugaku, 1

Lada, C. J. & Lada, E. A. 2003, ARA&A, 41, 57

Lada, E. A., Strom, K. M., & Myers, P. C. 1993, in Protostars and Planets III, ed. E. H. Levy & J. I. Lunine, 245

Lebouteiller, V., Barry, D. J., Goes, C., et al. 2015, ApJS, 218, 21

Levine, J. L., Steinhauer, A., Elston, R. J., & Lada, E. A. 2006, The Astrophysical Journal, 646, 1215

Lique, F., Spielfiedel, A., Feautrier, N., et al. 2010, J. Chem. Phys., 132, 024303

Liu, Y., Henning, T., Carrasco-González, C., et al. 2017, A&A, 607, A74

Loison, J.-C., Wakelam, V., & Hickson, K. M. 2014, MNRAS, 443, 398

Long, F., Herczeg, G. J., Pascucci, I., et al. 2017, ApJ, 844, 99

Long, F., Pinilla, P., Herczeg, G. J., et al. 2018, ApJ, 869, 17

Loomis, R. A., Öberg, K. I., Andrews, S. M., & MacGregor, M. A. 2017, ApJ, 840, 23

Loomis, R. A., Öberg, K. I., Andrews, S. M., et al. 2018, AJ, 155, 182

Luhman, K. L. 2008, Chamaeleon, Vol. 5 (Astronomical Society of the Pacific Monograph Publications), 169

Lynden-Bell, D. & Pringle, J. E. 1974, MNRAS, 168, 603

MacGregor, M. A., Wilner, D. J., Czekala, I., et al. 2017, ApJ, 835, 17

Mairs, S., Lalchand, B., Bower, G. C., et al. 2019, ApJ, 871, 72

Manara, C. F., Morbidelli, A., & Guillot, T. 2018, A&A, 618, L3

Manara, C. F., Robberto, M., Da Rio, N., et al. 2012, ApJ, 755, 154

Mann, R. K., Andrews, S. M., Eisner, J. A., et al. 2015, ApJ, 802, 77

Mann, R. K., Di Francesco, J., Johnstone, D., et al. 2014, ApJ, 784, 82

Mann, R. K. & Williams, J. P. 2010, ApJ, 725, 430

Mathews, G. S., Klaassen, P. D., Juhász, A., et al. 2013, A&A, 557, A132

McClure, M. K., Bergin, E. A., Cleeves, L. I., et al. 2016, ApJ, 831, 167

Megeath, S. T., Gutermuth, R., Muzerolle, J., et al. 2012, AJ, 144, 192

Megeath, S. T., Gutermuth, R., Muzerolle, J., et al. 2016, AJ, 151, 5

Meingast, S., Alves, J., Mardones, D., et al. 2016, A&A, 587, A153

Menten, K. M., Reid, M. J., Forbrich, J., & Brunthaler, A. 2007, A&A, 474, 515

Merín, B., Brown, J. M., Oliveira, I., et al. 2010, ApJ, 718, 1200

Meyer, M. R. 1996, PhD thesis, Max-Planck-Institut für Astronomie, Königstuhl 17, D-69117 Heidelberg, Germany

Meyer, M. R., Flaherty, K., Levine, J. L., et al. 2008, Star Formation in NGC 2023, NGC 2024, and Southern L1630, Vol. 4 (Astronomical Society of the Pacific Monograph Publications), 662

Miotello, A., Bruderer, S., & van Dishoeck, E. F. 2014, A&A, 572, A96

Miotello, A., van Dishoeck, E. F., Kama, M., & Bruderer, S. 2016, A&A, 594, A85

Miotello, A., van Dishoeck, E. F., Williams, J. P., et al. 2017, A&A, 599, A113

Mohanty, S., Greaves, J., Mortlock, D., et al. 2013, ApJ, 773, 168

Murillo, N. M., Lai, S.-P., Bruderer, S., Harsono, D., & van Dishoeck, E. F. 2013, A&A, 560, A103

Muzerolle, J., Hillenbrand, L., Calvet, N., Briceño, C., & Hartmann, L. 2003, ApJ, 592, 266

Natta, A., Testi, L., Neri, R., Shepherd, D. S., & Wilner, D. J. 2004, A&A, 416, 179

Natta, A., Testi, L., & Randich, S. 2006, A&A, 452, 245

Nuernberger, D., Chini, R., & Zinnecker, H. 1997, A&A, 324, 1036

Öberg, K. I., Furuya, K., Loomis, R., et al. 2015, ApJ, 810, 112

Öberg, K. I., Qi, C., Fogel, J. K. J., et al. 2011, ApJ, 734, 98

Öberg, K. I., van Broekhuizen, F., Fraser, H. J., et al. 2005a, ApJ, 621, L33

Öberg, K. I., van Broekhuizen, F., Fraser, H. J., et al. 2005b, ApJ, 621, L33

O'Dell, C. R. 1998, AJ, 115, 263

O'Dell, C. R. 2001, ARA&A, 39, 99

O'Dell, C. R. & Wen, Z. 1994, ApJ, 436, 194

O'Dell, C. R., Wen, Z., & Hu, X. 1993, ApJ, 410, 696

O'dell, C. R. & Wong, K. 1996, AJ, 111, 846

Okuzumi, S., Momose, M., Sirono, S.-i., Kobayashi, H., & Tanaka, H. 2016, ApJ, 821, 82

Oliveira, J. M., Jeffries, R. D., Kenyon, M. J., Thompson, S. A., & Naylor, T. 2002, A&A, 382, L22

Oliveira, J. M., Jeffries, R. D., & van Loon, J. T. 2004, MNRAS, 347, 1327

Panić, O., Holland, W. S., Wyatt, M. C., et al. 2013, MNRAS, 435, 1037

Papaloizou, J. & Lin, D. N. C. 1984, ApJ, 285, 818

Pascucci, I., Testi, L., Herczeg, G. J., et al. 2016, ApJ, 831, 125

Pecaut, M. J., Mamajek, E. E., & Bubar, E. J. 2012, ApJ, 746, 154

Peterson, D. E. & Megeath, S. T. 2008, The Orion Molecular Cloud 2/3 and NGC 1977 Regions (Astronomical Society of the Pacific Monograph Publications), 590

Pinilla, P., Benisty, M., & Birnstiel, T. 2012, A&A, 545, A81

Pinilla, P., van der Marel, N., Pérez, L. M., et al. 2015, A&A, 584, A16

Pinte, C., Dent, W. R. F., Ménard, F., et al. 2016, ApJ, 816, 25

Porras, A., Christopher, M., Allen, L., et al. 2003, AJ, 126, 1916

Povich, M. S., Kuhn, M. A., Getman, K. V., et al. 2013, ApJS, 209, 31

Preibisch, T., Brown, A. G. A., Bridges, T., Guenther, E., & Zinnecker, H. 2002, AJ, 124, 404

Qi, C., Öberg, K. I., Andrews, S. M., et al. 2015, ApJ, 813, 128

Qi, C., Öberg, K. I., Wilner, D. J., et al. 2013, Science, 341, 630

Rapson, V. A., Kastner, J. H., Millar-Blanchaer, M. A., & Dong, R. 2015, ApJ, 815, L26

Reboussin, L., Guilloteau, S., Simon, M., et al. 2015, A&A, 578, A31

Reipurth, B., Pedrosa, A., & Lago, M. T. V. T. 1996, A&AS, 120, 229

Ren, Z. & Li, D. 2016, ApJ, 824, 52

Ribas, Á., Bouy, H., & Merín, B. 2015, A&A, 576, A52

Ribas, Á., Merín, B., Bouy, H., & Maud, L. T. 2014, A&A, 561, A54

Ricci, L., Robberto, M., & Soderblom, D. R. 2008, AJ, 136, 2136

Ricci, L., Trotta, F., Testi, L., et al. 2012, A&A, 540, A6

Rosotti, G. P., Booth, R. A., Tazzari, M., et al. 2019, MNRAS, 486, L63

Ruíz-Rodríguez, D., Cieza, L. A., Williams, J. P., et al. 2018, MNRAS, 478, 3674

Salinas, V. N., Hogerheijde, M. R., Mathews, G. S., et al. 2017, A&A, 606, A125

Salter, D. M., Hogerheijde, M. R., van der Burg, R. F. J., Kristensen, L. E., & Brinch, C. 2011, A&A, 536, A80

Scally, A. & Clarke, C. 2001, MNRAS, 325, 449

Schwarz, G. 1978, Ann. Statist., 6, 461

Sheehan, P. D. & Eisner, J. A. 2018, ApJ, 857, 18

Siess, L., Dufour, E., & Forestini, M. 2000, A&A, 358, 593

Simón-Díaz, S., Herrero, A., Esteban, C., & Najarro, F. 2006, A&A, 448, 351

Skinner, S., Gagné, M., & Belzer, E. 2003, ApJ, 598, 375

Sokal, K. R., Deen, C. P., Mace, G. N., et al. 2018, ApJ, 853, 120

Stammler, S. M., Drazkowska, J., Birnstiel, T., et al. 2019, arXiv e-prints, arXiv:1909.04674

Strom, K. M., Strom, S. E., Edwards, S., Cabrit, S., & Skrutskie, M. F. 1989, AJ, 97, 1451

Stutz, A. M., Tobin, J. J., Stanke, T., et al. 2013, ApJ, 767, 36

Takahashi, S. Z. & Inutsuka, S.-i. 2014, ApJ, 794, 55

Tang, Y.-W., Dutrey, A., Guilloteau, S., et al. 2016, ApJ, 820, 19

Tazzari, M., Testi, L., Natta, A., et al. 2017, A&A, 606, A88

Teague, R., Guilloteau, S., Semenov, D., et al. 2016, A&A, 592, A49

Teague, R., Semenov, D., Gorti, U., et al. 2017, ApJ, 835, 228

Testi, L., Birnstiel, T., Ricci, L., et al. 2014, in Protostars and Planets VI, ed. H. Beuther, R. S. Klessen, C. P. Dullemond, & T. Henning, 339

Thi, W.-F., van Zadelhoff, G.-J., & van Dishoeck, E. F. 2004, A&A, 425, 955

Tobin, J. J., Hartmann, L., Chiang, H.-F., et al. 2012, Nature, 492, 83

Tobin, J. J., Kratter, K. M., Persson, M. V., et al. 2016, Nature, 538, 483

Trapman, L., Facchini, S., Hogerheijde, M. R., van Dishoeck, E. F., & Bruderer, S. 2019, A&A, 629, A79

Tripathi, A., Andrews, S. M., Birnstiel, T., & Wilner, D. J. 2017, ApJ, 845, 44

Tsukagoshi, T., Saito, M., Kitamura, Y., et al. 2011, ApJ, 726, 45

Tychoniec, Ł., Tobin, J. J., Karska, A., et al. 2018, ApJS, 238, 19

Uyama, T., Hashimoto, J., Kuzuhara, M., et al. 2017, AJ, 153, 106

van der Marel, N., Dong, R., di Francesco, J., Williams, J. P., & Tobin, J. 2019, ApJ, 872, 112

van der Marel, N., van Dishoeck, E. F., Bruderer, S., et al. 2016a, A&A, 585, A58

van der Marel, N., van Dishoeck, E. F., Bruderer, S., et al. 2016b, A&A, 585, A58

van der Marel, N., van Dishoeck, E. F., Bruderer, S., et al. 2013, Science, 340, 1199

van der Marel, N., Verhaar, B. W., van Terwisga, S., et al. 2016c, A&A, 592, A126

van der Marel, N., Verhaar, B. W., van Terwisga, S., et al. 2016d, A&A, 592, A126

van der Marel, N., Verhaar, B. W., van Terwisga, S., et al. 2016e, A&A, 592, A126

van der Marel, N., Williams, J. P., & Bruderer, S. 2018a, ApJ, 867, L14

van der Marel, N., Williams, J. P., & Bruderer, S. 2018b, ApJ, 867, L14

van der Plas, G., Wright, C. M., Ménard, F., et al. 2017, A&A, 597, A32

van Kempen, T. A., van Dishoeck, E. F., Brinch, C., & Hogerheijde, M. R. 2007, A&A, 461, 983

van 't Hoff, M. L. R., Walsh, C., Kama, M., Facchini, S., & van Dishoeck, E. F. 2017a, A&A, 599, A101

van 't Hoff, M. L. R., Walsh, C., Kama, M., Facchini, S., & van Dishoeck, E. F. 2017b, A&A, 599, A101

van Terwisga, S. E., Hacar, A., & van Dishoeck, E. F. 2019a, arXiv e-prints, arXiv:1905.09804

van Terwisga, S. E., Hacar, A., & van Dishoeck, E. F. 2019b, arXiv e-prints, arXiv:1905.09804

van Terwisga, S. E., van Dishoeck, E. F., Ansdell, M., et al. 2018a, A&A, 616, A88

van Terwisga, S. E., van Dishoeck, E. F., Ansdell, M., et al. 2018b, A&A, 616, A88

van Terwisga, S. E., van Dishoeck, E. F., Cazzoletti, P., et al. 2019c, A&A, 623, A150

Visser, R., Bruderer, S., Cazzoletti, P., et al. 2018, A&A, 615, A75

Walsh, C., Juhász, A., Meeus, G., et al. 2016, ApJ, 831, 200

Walsh, C., Juhász, A., Pinilla, P., et al. 2014, ApJ, 791, L6

Watanabe, T. & Mitchell, G. F. 2008, AJ, 136, 1947

Weingartner, J. C. & Draine, B. T. 2001, ApJ, 548, 296

Wichmann, R., Krautter, J., Covino, E., et al. 1997, A&A, 320, 185

Wijnen, T. P. G., Pols, O. R., Pelupessy, F. I., & Portegies Zwart, S. 2017, A&A, 604, A91

Wilking, B. A., Gagné, M., & Allen, L. E. 2008, Star Formation in the ρ Ophiuchi Molecular Cloud, Vol. 5 (Astronomical Society of the Pacific Monograph Publications), 351

Wilking, B. A., Meyer, M. R., Robinson, J. G., & Greene, T. P. 2005, AJ, 130, 1733

Williams, J. P. & Best, W. M. J. 2014, ApJ, 788, 59

Williams, J. P., Cieza, L., Hales, A., et al. 2019, ApJ, 875, L9

Williams, J. P. & Gaidos, E. 2007, ApJ, 663, L33

Winter, A. J., Clarke, C. J., Rosotti, G. P., Hacar, A., & Alexander, R. 2019, MNRAS, 2191

Woitke, P., Min, M., Thi, W. F., et al. 2018, ArXiv e-prints, arXiv:1807.05784

Young, A. K., Bate, M. R., Harries, T. J., & Acreman, D. M. 2019, MNRAS, 487, 2853

Zhang, K., Bergin, E. A., Blake, G. A., et al. 2016, ApJ, 818, L16

Zhang, K., Blake, G. A., & Bergin, E. A. 2015, ApJ, 806, L7

Zhang, S., Zhu, Z., Huang, J., et al. 2018, ApJ, 869, L47

Zhu, Z., Zhang, S., Jiang, Y.-F., et al. 2019, ApJ, 877, L18

Nederlandse samenvatting

Hoe ontstaat een planeet als de Aarde? Of, iets algemener, hoe ontstaat een zonnestelsel als het onze – en hoe kunnen we de uiteindelijke architectuur van een planetenstelsel verbinden met de eigenschappen van het materiaal dat rondom jonge sterren wordt waargenomen? Dit is, in de breedste zin, de vraag die aan de basis ligt van het onderzoek naar protoplanetaire schijven en dus ook aan dit proefschrift.

Dit soort vragen zijn heel oud: ze komen terug in scheppingsmythen over de hele wereld. Het is dus ook niet zo verwonderlijk dat ook de astronomen van de zeventiende eeuw, zoals Christiaan Huygens, zich bezighielden met "den oorsprong der Hairstarren [kometen] als mede van de Dwaalstarren, en van de Wereld". Wat Huygens' behandeling van deze vragen interessant maakt is zijn conclusie dat er met de middelen van zijn tijd geen goed antwoord op te geven was. Vanuit de huidige wetenschap moeten we hem daar gelijk in geven. Maar de sterrenkunde is bij uitstek een vakgebied dat door waarnemingen wordt gedreven. Het ontwikkelen en verfijnen van telescopen en lenzen om met het blote oog door te kijken was in Huygens' tijd revolutionair; in de 21ste eeuw heeft de ontwikkeling van infrarood- en submillimeter-telescopen gezorgd voor een enorme sprong in het vermogen van astronomie om onderzoek te doen naar de koude, donkere omgevingen waarin planetenstelsels ontstaan. Wat echter ook niet onderschat moet worden, is het verschil in wereldbeeld tussen de moderne astronomie en dat in Huygens' tijd. Zijn heelal was – een enkele komeet of nova daargelaten – nogal statisch, en het ontstaan van planeten was letterlijk buiten bereik. Tegenwoordig weten we dat het ontstaan van sterren en van planeten om die sterren een proces is dat nog steeds gaande is.

De vraag die hierboven gesteld werd is natuurlijk te breed om in een korte samenvatting te beantwoorden. Dit proefschrift gaat daarom uit van een specifiekere vraag: wat kunnen we leren over de evolutie van protoplanetaire schijven, en in het bijzonder van hun massa en structuur, door te kijken vanuit het perspectief van populaties? Om deze vraag te beantwoorden, is het eerst handig om kort te kijken naar de structuur van een protoplanetaire schijf in het algemeen en naar de manier waarop sterren vormen in de Melkweg. Het blijkt namelijk zo te zijn dat we, met de juiste telescoop, daadwerkelijk kunnen beginnen aan een demografische aanpak als deze.

Protoplanetaire schijven

Wat ís een protoplanetaire schijf eigenlijk – en waarom een schijf en geen bol, of iets dergelijks? Het ontstaan van een ster begint als een wolk stof en gas onder zijn eigen zwaartekracht samentrekt en, van binnen naar buiten, ineenstort. In het midden van de wolk ontstaat een protoster. Maar niet al het materiaal in de wolk kan naar het zwaartepunt vallen: de wolk draait gemiddeld een klein beetje rond, en die draaiing gaat moeilijk weg. Formeel gezegd blijft het hoekmoment van de wolk behouden. Het gevolg is dat er een schijf ontstaat van

om de ster draaiend gas en stof: een protoplanetaire schijf. De rest van de wolk verdwijnt, in de loop van ongeveer een half miljoen jaar, in de schijf en ster of in de interstellaire ruimte. Daarna is echter de protoplanetaire schijf nog een paar miljoen jaar zichtbaar om de ster, totdat ook de schijf verdwijnt en er alleen een planetenstelsel, kometen en wat overgebleven stof om de ster over zijn.

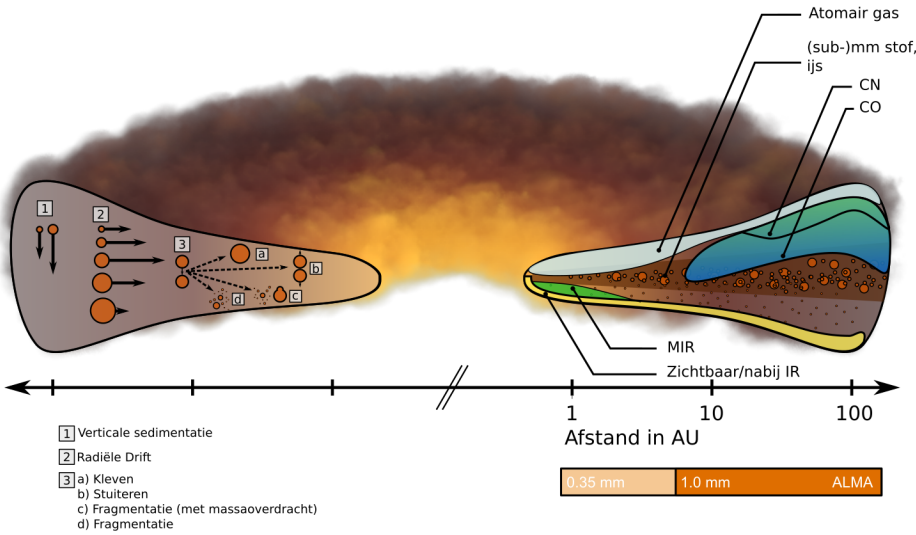

Figuur 1: Schematisch overzicht van de evolutie van stofdeeltjes *(links)* in een protoplanetaire schijf, en van de delen van de schijf die met verschillende golflengtes kunnen worden waargenomen *(rechts)*. Figuur aangepast uit Testi et al. (2014)

De naam 'schijf' doet de complexe structuur van deze objecten niet veel eer aan. Zoals te zien is in Figuur 1 is een protoplanetaire schijf niet vlak, maar wordt hij hoger verder van de ster. Naar binnen en boven toe is de schijf warmer. Bovendien neemt de dichtheid naar buiten toe af. Het is geen verrassing dat het gas in de schijf dus ook niet overal dezelfde samenstelling heeft. Moleculair waterstof, H_2, domineert de totale massa van de schijf, maar is moeilijk waar te nemen. Koolmonoxide, CO, is met ALMA wél goed waarneembaar, maar bevriest in het midden van de schijf, waar het donker en koud genoeg (minder dan 20 K) is. Te hoog in de schijf kan de felle ultraviolette (UV) straling van de jonge ster door het ijlere stof en gas dringen en wordt CO vernietigd; maar diezelfde UV-straling zorgt ook indirect voor de productie van andere moleculen, zoals het cyanide-radicaal (CN), dat zich in vergelijking met CO wat hoger in de schijf bevindt. Door te begrijpen hoe een molecuul wordt geproduceerd en afgebroken, en door modellen van een protoplanetaire schijf te vergelijken met waarnemingen, is het dus mogelijk om uitspraken te doen over de structuur van de schijf.

Het stof in de schijf zit ook niet stil: vergeleken met de interstellaire ruimte en zelfs de wolk waaruit de schijf ontstond zijn de dichtheden hoger. Stofdeeltjes groeien en bewegen ten opzichte van het gas. Er spelen allerlei processen tegelijkertijd een rol, maar het nettoeffect is dat kleine stofdeeltjes (ongeveer een micrometer in diameter) door de hele schijf te vinden zijn. Stofdeeltjes die door botsingen zijn gegroeid tot groottes van ongeveer een

millimeter of meer zakken naar het midden (als we de schijf van opzij bekijken, zoals in Figuur 1) en vormen in vergelijking met het kleine stof en het gas een veel plattere schijf. Dit zijn de stofdeeltjes die we met de ALMA-telescoop waarnemen.

De protoplanetaire schijf in Figuur 1 is vrij glad. Eén van de belangrijkste ontdekkingen van de laatste jaren is echter dat, in het stof maar ook in het gas, allerlei structuur zichtbaar is. In plaats van een vlakke verdeling van stof zien we ringen stof om de jonge ster, en zelfs asymmetrische structuren. Op dit moment lijkt de invloed van de zwaartekracht van een verder niet zichtbare planeet in de ruimtes tussen de ringen de beste verklaring, een onderwerp dat ook wordt behandeld in Hoofdstuk 2 van dit proefschrift.

Van individu naar populatie

Stervorming in de nabije Melkweg

Wie demografisch onderzoek wil doen, moet goed nadenken over het soort populatie dat wordt bekeken. Hoe selecteer je leden van een vergelijkbare groep, in termen van de omgeving waarin ze leven en leeftijd? In dit geval gaat het natuurlijk niet om mensen maar om jonge sterren. Gelukkig blijkt de natuur ons hier te helpen: sterren ontstaan niet alleen, maar in groepen uit reusachtige moleculaire wolken. Deze wolken produceren genoeg sterren dat we er statistische methodes op kunnen loslaten. Bovendien zijn alle jonge sterren die uit zo'n wolk ontstaan van ongeveer dezelfde leeftijd. Zulke stervormingsgebieden worden genoemd naar het sterrenbeeld waarin ze te vinden zijn. In de nabije Melkweg zijn lang niet alle gebieden waarin jonge sterren ontstaan hetzelfde: sommige zijn ouder, sommige jonger. Dit betekent dat het mogelijk is om de eigenschappen van protoplanetaire schijven in zulke gebieden te vergelijken, om hun evolutie te bestuderen.

Een ander belangrijk punt waarop stervormingsgebieden van elkaar kunnen verschillen, is de aanwezigheid van massieve sterren. Sterren met een massa vanaf ongeveer acht keer die van de zon produceren enorme hoeveelheden ultraviolette straling die een dramatisch effect op hun directe omgeving hebben: ze verlichten (en vernietigen) de wolken moleculair gas waaruit ze zijn ontstaan en kunnen ook het gas en stof aan de buitenranden van protoplanetaire schijven om sterren in de buurt verhitten, tot de schijf als het ware verdampt. Maar zulke sterren zijn zeldzaam: in de buurt van de Zon vinden we ze alleen in Orion, in het zogenaamde Trapezium in de Orionnevel, en in de Vlamnevel (NGC 2024). Ze zijn daarom extra interessant vanuit het perspectief van de evolutie van protoplanetaire schijven, zeker omdat NGC 2024 één van de jongste stervormingsgebieden is, met een leeftijd van minder dan een miljoen jaar, terwijl de sterren rond het Trapezium ongeveer één tot drie miljoen jaar oud zijn (zie Hoofdstuk 4 en 5).

Het stervormingsgebied in Lupus is, daarbij vergeleken, vrij kalm: er is een populatie van ongeveer honderd schijven van één tot drie miljoen jaar oud. Deze populatie is goed vergelijkbaar met een aantal andere minder massieve stervormingsgebieden in de buurt van de zon, en heeft het voordeel dat zowel het stof, CO en CN, en de eigenschappen van de sterren goed bekend zijn. In dit proefschrift wordt eerst gekeken naar de eigenschappen van de protoplanetaire schijven in Lupus, om daarna de blik te verleggen naar de populaties jonge sterren met schijven in OMC-2 (een moleculaire wolk net ten noorden van het Trapezium) en NGC 2024.

Demografie van protoplanetaire schijven

Zoals we hebben gezien is het dus mogelijk om populaties van protoplanetaire schijven te vinden van verschillende leeftijden op verschillende plekken in de – relatieve – buurt van de zon. Een belangrijke eerste vraag om te stellen is dan hoeveel sterren met een protoplanetaire schijf in een stervormingsgebied te vinden zijn, als fractie van de leeftijd van zo'n gebied. De conclusie van dit onderzoek, dat werd gedaan op infrarode golflengtes, is dat protoplanetaire schijven inderdaad zeldzamer zijn in oudere gebieden, zoals we zouden verwachten op basis van de theorieën van stervorming die hierboven zijn beschreven.

Figuur 2: In deze foto (gedeeld door de Joint ALMA Observatory) is een groot deel van de primaire ALMA-antennes te zien. Het werk dat in dit proefschrift wordt behandeld is gebaseerd op waarnemingen met deze telescoop – zie de verschillende Hoofdstukken 2 – 5 voor voorbeelden. Door de signalen van alle antennes aan elkaar te verbinden is het mogelijk om een extreem hoge resolutie en gevoeligheid te bereiken.

In de afgelopen jaren is de bijdrage van ALMA (Figuur 2) aan dit soort onderzoek van groot belang geweest. ALMA – de Atacama Large Millimeter/submillimeter Array – is in staat om zowel het moleculaire gas als stofdeeltjes ter grootte van een millimeter in een protoplanetaire schijf waar te nemen. Dankzij ALMA's indrukwekkende gevoeligheid is het mogelijk om met waarneemtijden van een minuut per object alsnog een flink percentage van de populatie te detecteren, en zelfs om stof- en gasstructuren waar te nemen.

Eén van de belangrijkste resultaten van ALMA, en van de Submillimeter Array (SMA), een andere telescoop die op vergelijkbare golflengtes waarneemt, is dat niet alleen de fractie protoplanetaire schijven afhangt van de leeftijd van een stervormingsgebied, maar dat er ook een trend lijkt te zijn in de hoeveelheid stof die we waarnemen om jonge schijven als functie van de ouderdom van een stervormingsgebied. Op dezelfde manier is duidelijk geworden dat de hoeveelheid UV-straling in een gebied een sterk effect kan hebben op de evolutie van protoplanetaire schijven.

Dit proefschrift

Het werk dat in dit proefschrift wordt behandeld is gebaseerd op ALMA-surveys van protoplanetaire schijven in drie stervormingsgebieden: Lupus, OMC-2, en NGC 2024 – de laatste allebei in Orion. Elk van deze gebieden biedt nieuwe informatie vanuit het perspectief van demografische analyse. Lupus (Hoofdstuk 2 en 3) kan gezien worden als prototype van een stervormingsgebied zonder massieve sterren. De hoofdstukken waarin wordt gekeken naar

Orion gaan juist in op de invloed van die massieve sterren op de evolutie van protoplanetaire schijven.

V1094 Sco – Een zeldzaam grote protoplanetaire schijf met meerdere ringen

In Hoofdstuk Twee wordt gekeken naar de eigenschappen van een onverwachtte protoplanetaire schijf in Lupus. Vergeleken met de andere schijven in de Lupus survey is V1094 Sco op meerdere manieren bijzonder: allereerst, omdat het een bijzonder helder (en dus massief) object is. Ten tweede, omdat er twee stofringen in de schijf te zien zijn. Hoewel er meerdere 'transition disks' in Lupus zijn, waarin de stofring een enkel diep gat laat zien, zijn dit soort goed gedefinieerde ringen in verhouding zeldzamer. Tenslotte is V1094 Sco interessant vanwege de grootte van de stofschijf: tot 300 AU van de ster, waarbij 1 AU de gemiddelde afstand tussen de Aarde en Zon is, en de gemiddelde schijf in Lupus kleiner is dan 60 AU (in het stof).

Deze laatste eigenschap is interessant omdat het nieuw licht werpt op het ontstaan van planeten. De meest voor de hand liggende verklaring van de ringen van V1094 Sco is dat één of meerdere onzichtbare planeten het stof wegduwen uit hun baan. Dit was, in andere protoplanetaire schijven met vergelijkbare structuren, ambiguër.

De waarde van de survey in Lupus ligt erin dat we deze schijf kunnen vergelijken met andere protoplanetaire schijven in Lupus, zonder dat er grote verschillen in gevoeligheid of resolutie zijn. De conclusie daarvan is dat protoplanetaire schijven als V1094 Sco zeldzaam zijn: IM Lup en V1094 Sco zijn beide $\sim$ 300 AU groot, maar de derde grootste protoplanetaire schijf in Lupus is $\sim$ 160 AU; de totale fractie reuzenschijven is ongeveer 2%.

De ALMA survey van protoplanetaire schijven in Lupus – Bewijs voor compacte gasschijven en moleculaire ringen uit CN-waarnemingen

Het cyanideradicaal CN is een vrij algemeen voorkomend molecuul in protoplanetaire schijven, en goed waar te nemen op millimeter-golflengtes. Uit modellen is bekend dat de hoeveelheid CN-emissie afhangt van in het bijzonder de grootte van de gasschijf, en – zoals gezegd – van de hoeveelheid UV-straling. Op basis van modellen verwachten we bovendien dat emissie het helderste is in een ring om de ster.

In dit hoofdstuk wordt gebruik gemaakt van de CN-waarnemingen die zijn gedaan als onderdeel van de survey van protoplanetaire schijven in Lupus geleid door Jonathan Williams en Megan Ansdell (Univ. Hawaii). Een opvallende waarneming is dat een aantal protoplanetaire schijven zowel in continuum- als in CN-emissie erg zwak is. Door de CN- en continuum-flux tegen elkaar uit te zetten, en te vergelijken met de gesimuleerde data van een grid van modellen van protoplanetaire schijven (ontwikkeld door Paolo Cazzoletti) is het mogelijk om te bepalen welke eigenschap van de schijven hiervoor zorgt. Het blijkt dat alleen modellen met een compacte gasschijf ($\leq$ 15 AU) deze waarnemingen reproduceren. Dit is een belangrijke conclusie omdat op basis van stofemissie alleen het lastig is om te zeggen of een protoplanetaire schijf compact is.

Tenslotte wordt in dit hoofdstuk de in de modellen voorspelde emissie-ring van CN waargenomen in twee protoplanetaire schijven uit het Lupus-sample. Ook wordt bevestigd dat er geen aanpassingen in het dichtheidsprofiel van de schijf nodig zijn om deze ringen te reproduceren, maar dat de sterkte van het UV-stralingsveld van groot belang is. Dit betekent dat,

als de verdere eigenschappen van de protoplanetaire schijf bekend zijn, CN ook kan dienen als tracer van de lastig waar te nemen UV-straling tussen 91.2 en 110 nm.

De massa's van protoplanetaire schijven in de Orion Molecular Cloud-2: het onderscheid tussen tijd en omgeving

Zoals gezegd zijn er meerdere gebieden in Orion waarin jonge massieve sterren een grote invloed hebben op hun omgeving. Het scheiden van de invloed van de felle UV-straling van jonge sterren, waardoor materiaal van de protoplanetaire schijven in de buurt wordt weggeblazen, en van de tijdsevolutie van een schijf, waarbij de totale massa ook afneemt, is echter lastig.

Het is al langer bekend dat protoplanetaire schijven dichter bij de massieve sterren in het Trapezium-cluster in massa afnemen. De massa's van de protoplanetaire schijven op afstanden van meer dan 0.5 pc van deze sterren, maar in dezelfde wolk, zijn dus een belangrijke bron van informatie over hoe een populatie schijven van dezelfde leeftijd eruit ziet zonder het effect van de Trapezium-sterren, maar waren tot nu toe niet goed gekarakteriseerd. In dit hoofdstuk wordt deze vergelijking gemaakt met behulp van een continuum-survey van protoplanetaire schijven in OMC-2.

Het belangrijkste resultaat van dit hoofdstuk is dat de massa's van protoplanetaire schijven in OMC-2 niet te onderscheiden zijn van die in Lupus en een aantal andere nabije stervormingsgebieden van dezelfde leeftijd, maar waarin geen massieve sterren te vinden zijn. Tegelijkertijd is het verschil in massa's tussen het hier onderzochte sample en de eerdere waarnemingen van protoplanetaire schijven in de buurt van het Trapezium consistent met de interpretatie dat de laatste groep hun massa heeft verloren door externe irradiatie met ver-ultraviolette straling. De interpretatie van dit resultaat is dat, mits geïsoleerd van externe invloeden, de evolutie en het ontstaan van een protoplanetaire schijf overal op dezelfde manier kunnen gebeuren.

Massa's van protoplanetaire schijven in NGC 2024: aanwijzingen voor twee populaties

In Hoofdstuk 5 wordt gekeken naar de protoplanetaire schijven in NGC 2024. Vergeleken met het Trapezium en OMC-2 is NGC 2024 een jong stervormingsgebied, en bevat het tenminste één massieve ster, waardoor het een geschikt gebied is om de impact van de omgeving op de vroege evolutie van protoplanetaire schijven te bestuderen. Bovendien is dit gebied onderdeel van gegarandeerde waarneemtijd met de James Webb Space Telescope (JWST).

De waarnemingen die in dit hoofdstuk worden gebruikt beslaan een gebied van ongeveer 3 bij 3 boogminuten, een gebied dat zowel het binnenste deel van het cluster jonge sterren als de buitengebieden beslaat. Opvallend genoeg is het percentage gedetecteerde protoplanetaire schijven in de binnenste (oostelijke) delen van het cluster vergeleken met de buitendelen van het cluster in het westen veel hoger, ook al is juist in het oostelijke deel de geprojecteerde afstand tot de massieve ster(ren) het kleinst, en zouden we daar dus juist een lagere detectiefractie verwachten.

Om dit te verklaren grijpen we terug naar de grotere-schaal eigenschappen van zowel de sterpopulatie als de moleculaire wolken. In het oosten is een zeer jonge ($\sim$ 0.5 Myr) populatie sterren nog gedeeltelijk ingebed in een dichte moleculaire wolk, en daardoor nog niet sterk blootgesteld aan de invloed van de massieve sterren. Deze populatie lijkt, in termen van schijfmassa's, sterk op die van protoplanetaire schijven in Lupus, ook al zijn ze jong. De

westelijke populatie sterren is daarentegen ouder en veel sterker blootgesteld aan het UV-stralingsveld, en de protoplanetaire schijven in dit deel van het veld lijken dus ook sterk op die in de buurt van het Trapezium.

Belangrijkste resultaten

Op een rij gezet zijn de belangrijkste resultaten van dit proefschrift als volgt:

- Protoplanetaire schijven met stof op afstanden van de ster buiten 150 AU zijn zeldzaam, terwijl compacte schijven in een populatie van een miljoen jaar oud veel algemener voorkomen.
- In totaal verschillende moleculaire wolken kunnen protoplanetaire schijven van dezelfde leeftijd er vergelijkbaar uitzien in termen van hun stofemissie, wat suggereert dat hun initiële eigenschappen ook vergelijkbaar zijn.
- Het is belangrijk om in complexe, massieve stervormingsgebieden rekening te houden met de mogelijke aanwezigheid van populaties sterren van verschillende leeftijden, omdat de eigenschappen van hun protoplanetaire schijven ook anders zijn.

Toekomstperspectieven

Een paar van de vervolgstappen in het onderzoek naar protoplanetaire schijven zijn duidelijk. Het aantal gebieden waarin surveys van protoplanetaire schijven met ALMA zijn gedaan, is nog steeds relatief klein. Bovendien lijkt een aantal van deze gebieden relatief vrij sterk op elkaar. Dit geldt zowel voor waarnemingen van het stof in deze schijven als voor het gas, en in het bijzonder voor moleculen anders dan CO. Juist die moleculen kunnen waardevolle inzichten in de chemische processen en structuur van 'gewone' protoplanetaire schijven bieden, buiten onze huidige focus op de meest massieve objecten. De eigenschappen van de sterren zelf blijven ook een belangrijk ingrediënt in ons begrip van de (populaties van) protoplanetaire schijven die worden waargenomen.

Ons begrip van hoe de kometen en planeten ontstaan, en van het ontstaan van de Aarde zelf wordt steeds dieper dankzij de voortdurende nieuwe resultaten van ALMA, het steeds verbeteren van modellen, en in de nabije toekomst de lancering van de James Webb Space Telescope. Hoewel er nog steeds veel grote open vragen zijn, zijn het vragen waarop steeds vaker een steeds beter antwoord te geven is.

List of Publications

First-author publications

V1094 Scorpii: A rare giant multi-ringed disk around a T-Tauri star
van Terwisga, S. E.; van Dishoeck, E. F.; Ansdell, M.; van der Marel, N.; Testi, L.; Williams, J. P.; Facchini, S.; Tazzari, M.; Hogerheijde, M. R.; Trapman, L.; Manara, C. F.; Miotello, A.; Maud, L. T.; Harsono, D., 2018, A&A, 616, 88

The ALMA Lupus protoplanetary disk survey: evidence for compact gas disks and molecular rings from CN
van Terwisga, S. E.; van Dishoeck, E. F.; Cazzoletti, P.; Facchini, S.; Trapman, L.; Williams, J. P.; Manara, C. F.; Miotello, A.; van der Marel, N.; Ansdell, M.; Hogerheijde, M. R.; Tazzari, M.; Testi, L., 2019, A&A, 623, 150

Disk masses in the Orion Molecular Cloud-2: distinguishing time and environment
van Terwisga, S.E.; Hacar, A.; van Dishoeck, E.F., 2019, A&A, 628, 85

Co-authored publications

Bright C_2H emission in protoplanetary discs in Lupus: high volatile C/O > 1 ratios
Miotello, A.; Facchini, S.; van Dishoeck, E. F.; Cazzoletti, P.; Testi, L.; Williams, J. P.; Ansdell, M.; **van Terwisga, S.**; van der Marel, N., 2019, A&A, 631, 69

ALMA Survey of Lupus Protoplanetary Disks. II. Gas Disk Radii
Ansdell, M.; Williams, J. P.; Trapman, L.; **van Terwisga, S. E.**; Facchini, S.; Manara, C. F.; van der Marel, N.; Miotello, A.; Tazzari, M.; Hogerheijde, M.; Guidi, G.; Testi, L.; van Dishoeck, E. F., 2018, ApJ, 859, 21

New Insights into the Nature of Transition Disks from a Complete Disk Survey of the Lupus Star-forming Region
van der Marel, Nienke; Williams, Jonathan P.; Ansdell, M.; Manara, Carlo F.; Miotello, Anna; Tazzari, Marco; Testi, Leonardo; Hogerheijde, Michiel; Bruderer, Simon; **van Terwisga, S. E.**, Ewine F., 2018, ApJ, 854, 177

Searching for reflected light from τ Bootis b with high-resolution ground-based spectroscopy: Approaching the 10^{-5} contrast barrier
Hoeijmakers, H. J.; Snellen, I. A. G.; **van Terwisga, S. E.**, 2018, A&A, 610, 47

Lupus disks with faint CO isotopologues: low gas/dust or high carbon depletion?
Miotello, A.; van Dishoeck, E. F.; Williams, J. P.; Ansdell, M.; Guidi, G.; Hogerheijde, M.; Manara, C. F.; Tazzari, M.; Testi, L.; van der Marel, N.; **van Terwisga, S. E.**, 2017, A&A, 599, A113

ALMA Survey of Lupus Protoplanetary Disks. I. Dust and Gas Masses
Ansdell, M.; Williams, J. P.; van der Marel, N.; Carpenter, J. M.; Guidi, G.; Hogerheijde, M.; Mathews, G. S.; Manara, C. F.; Miotello, A.; Natta, A.; Oliveira, I.; Tazzari, M.; Testi, L.; van Dishoeck, E. F.; **van Terwisga, S. E.**, 2016, ApJ, 828, 46

The (w)hole survey: An unbiased sample study of transition disk candidates based on Spitzer catalogs van der Marel, N.; Verhaar, B. W.; **van Terwisga, S. E.**; Merín, B.; Herczeg, G.; Ligterink, N. F. W.; van Dishoeck, E. F., 2016, A&A, 592, 126

Curriculum Vitae

I was born in Rotterdam, the Netherlands, on 3 April 1992 to Peter and Liesbeth van Terwisga, followed a few years later by a sister (Heleen) and a brother (Friso). Apparently, as a small kid, carried along in a backpack by my dad during the holidays, I was fascinated by the little waterfalls in the Swiss mountains, and by the rocks on an Irish beach. This interest quickly grew into a love of space, and an intense curiosity for the (deep) past and the way the universe works on bigger scales.

I attended the Heijbergschool in Schiebroek from 1996 to 2004. Someone once wrote that the easiest way to discover a nerd is to see if their fantasies are time-symmetric[1], and he may be quite right, at least in this instance: I would still like to see what the solar system looked like in its earliest days. Obviously that fantasy is now grounded in a bit more science, but this was also a question that kept me busy already in primary school. I wrote an essay on the origin of the solar system, and loved going to the Naturalis museum, which plotted the evolution of life in the universe (along with beautiful fossil examples) in a spiral on the ground floor with my granddad. At the same time, I enjoyed reading about the origin of ideas, and about the history of science, as well as basically anything else. Around 2001, I also started learning to play the flute.

It was, in context, not a particularly strange idea for my dad to take me, at approximately this time, to an open night of the old observatory in Leiden during a Science Week, to encourage my fascination with the universe. In fact, it turned out to be a very good one, because it led to an invitation from W. Butler Burton to visit the Sterrewacht and talk in a bit more detail about the picture I had been asking questions about – one showing the scale of the universe, zooming out to the largest structures in the universe. These meetings in turn led to an introduction to Vincent Icke, and multiple return visits with him. It turns out there are *many* questions to ask about the universe and where all this comes from, and most importantly, that we can actually go about answering them, or getting a better idea of in what direction the answer lies. Saying the rest of this CV is a logical consequence of these meetings may be overstating things, but it is certainly true that they have played a major part.

From 2004 to 2010 I attended the Marnix Gymnasium in Rotterdam, where I quickly navigated into a physics, chemistry, and math-heavy curriculum, but also took French and Latin, and graduated with honours. At the same time, I discovered the incredibly rich world of baroque flute music under Kees Alers. In the third-to-last year of school, I was encouraged to sign up to the Pre-University College offered by Leiden University. This program was another look into the world of research, and very multidisciplinary, culminating into a two-person research project in 2009. Together with Hine van Os, I worked on observations of a transiting extrasolar planet, supervised by Ernst de Mooij and Ignas Snellen, and learned that I did not enjoy IDL but loved working on astronomical observations and interpreting

[1] Zach Wienersmith, 20 October 2019

them. This research project won a Jan Kijne prize, and helped solidify my decision to go to Leiden.

In Leiden, I followed the Bachelor's in Astronomy from 2010 to 2013, graduating cum laude. The programme offered several great opportunities to work with astronomical data: the observing practical, in the second year, took us to La Palma to observe with the Isaac Newton Telescope (INT) there, where I participated in observations of a desintegrating exoplanet, together with Arthur Bosman, Bavo Croiset, Alex Pietrov, and Emiel Por. To my continuing surprise, despite the weather and the scheduling of all of the different student projects, it actually worked: we did see two transits of varying depth. Of course, the Sterrewacht had and has more to offer than just planets: together with Arthur Bosman, and supervised by David Sobral and Huub Röttgering, I wrote a BSc thesis on finding Lyman-α-emitting galaxies at high redshifts, using observations from the INT. Huub also found time for Arthur and myself to go to Chile, and observe with the ESO NTT at La Silla – and see the night skies over the Andes. During this time, I also immersed myself in the oldest student's music association of the Netherlands, Sempre Crescendo, where I was introduced to the joys of playing the flute in an orchestra, and singing in small ensembles, although I never did learn to play the oboe very well.

From 2013 to 2015, I followed the Research in Astronomy Master's program in Leiden (graduating cum laude in 2015). The setup of the program, which includes two research projects, was another opportunity to enjoy astronomical research and in particular observational projects, with all the unexpected difficulties and surprises they always bring. Besides this, it gave me an opportunity to encounter a new topic: the study of protoplanetary disks. Together with Nienke van der Marel, I did a minor MSc thesis on fitting the spectral energy distributions of protoplanetary disks with evidence of inner gaps, with added information on their structure from Herschel and APEX observations. This research, which looked at the very origins of planetary systems, and was being revolutionized by the first ALMA observations, quickly grabbed me, and I decided I would really like to do more of this, if at all possible. To continue in the line of planets and planet formation, I was given the opportunity to write Master's thesis, supervised by Ignas Snellen and Jens Hoeijmakers, where we tried to extract the reflection of the host star from a hot Jupiter orbiting it. Although this was unsuccessful, the image it evoked of this giant dark planet, orbiting so close to its star, glowing sullenly with reprocessed heat, is still rather a nice one.

In 2015 I started as a PhD student in the group of Ewine van Dishoeck. Looking back at the supervision plan that was made back then, I see my topic was supposed to be the "combined observational and model studies of transitional disks" – in particular, ones with compact inner gaps. There was one problem: the proposal for ALMA observing time had not been accepted that year. What happened instead was that Ewine, a week and a half into my contract, suggested I join a meeting with the Lupus disk survey collaboration – Jonathan Williams, Megan Ansdell, John Carpenter, Carlo Manara, Michiel Hogerheijde, Marco Tazzari, Leonardo Testi, and others. This was an incredibly fruitful research project that proved that one minute of ALMA time per disk is already enough for amazing science, especially in a large and well-defined sample. The two Lupus-related articles included in this thesis are only a small fraction of the scientific output from this project.

The Lupus work drove the direction of this thesis work into a study of large samples of disks, and of what the population-level view can tell us of their evolution. This was encouraged greatly by Alvaro Hacar's arrival to the group. His Orion data may not have been intended for observations of protoplanetary disks – that did not mean that there weren't many of them in there. From Orion A, I then looked at Orion B, and the NGC 2024 star-forming

region, together with another group of new collaborators, including James di Francesco, Rita Mann, Michael Meyer, Sean Andrews, John Eisner, and several familiar faces from previous articles.

At the moment, I am a postdoctoral fellow at the Max-Planck Institute for Astronomy in Heidelberg, where I hope to continue on this line of research, expanding the sample of protoplanetary disk populations studied, and getting a deeper view of their properties and evolution.

Acknowledgements

In a memorable interview the Nobel-prize winning physicist Richard Feynman explains that if you ask 'why' something happens, you can go on forever asking deeper why's, and never get very far – an observation that also, I am afraid, extends to writing the acknowledgements of a thesis, because so many people have in so many ways affected it and me that this short chapter cannot possibly do them justice. In a spirit of pragmatism, here is at least a small and somewhat haphazard selection.

First of all, I want to thank my promotores: for giving me the opportunity to write this thesis, for their scientific input, and their advice, and the example you set.

Working in science is a privilege to begin with; but I feel very grateful at how welcoming, friendly, and open I have found this community. That is true in general, and in particular for the many people who have been involved with the articles and observing proposals that form the scientific part of this thesis. Jonathan and Megan, it has been a joy to work with you; that meeting of the Lupus project group in the first week of my PhD has determined the course of it all. Carlo, without you the Lupus completion survey would not have happened, but more than that, you taught me how to write an ALMA proposal and not despair. Leonardo, even apart from all your other input, thank you for pushing for the inclusion of the Band 7 data of V1094 Sco – it was an adventure in calibration and definitely the better for it. All those others who have, in some way, contributed to the Lupus surveys: this was a wonderful way to dive into the world of international astronomical cooperations (and telecons at odd times). While I have only joined at a distance, the work on NGC 2024 was similarly international. Thank you, in particular, James and Rita, for welcoming me to the project and for your work on the data, and I am looking forward to seeing what will come next. Alvaro, while the Orion disks collaboration may have been a bit smaller, your drive and creativity have made it a great experience. I can still barely believe that that crazy idea from the Cycle 5 supplemental call has now become a project that is actually going to get observed, and I hope we will discover many more nice results, expected and unexpected. I would also like to thank all those of you who made the CN survey possible. I have never thought chemical modelling was particularly easy and this project proved to me that it is more difficult even than that. Until we looked at your model grid, Paolo, what is now this thesis' third chapter never clicked for me. The meetings in Garching with you, and with Stefano, were hugely inspiring and always meant a jump in understanding for me (and usually more work for you). Thanks are also due to Ruud, for his work on the cyanide chemistry, and to Simon, without whom DALI, and so much science, would simply not exist.

There is significant overlap between these people and the past and present members of the Leiden-Garching group, as there should of course be. I have greatly enjoyed the telecons, group retreats, conferences, garden parties, and too few vrijdagmiddagborrels with all of you. Apart from your individual and collective knowledge and insight, I have always felt at ease in the group atmosphere, and that is probably even more important to an occasionally stressful four-year-project like this. Arthur, I will miss your wit, knowledge, and willingness to let

me bother you with questionable questions as much as having a colleague with a Banks-collection. Łukasz, you have made the only two coffees I have ever actually enjoyed; and I am happy that I can finally talk about outflows now and you are also looking at disks. Merel, thank you for teaching me the importance of the earliest parts of star formation, and for showing how to communicate complex ideas concisely. Daniel, for coming to the rescue of my data so often, and reminding me that ALMA calibration is an art as well as a science. Leon, for your positivity and bravery at using the HL elevators twice as much as we did. Giovanni, thank you for your insight in dust – I hope I will keep feeling more confused after meeting you for a long time to come. Shota, good luck on your quest for water. Maria, thank you for your lessons in running a group meeting without it running away from you. Alex, your humor and Canadianness made the group a nicer place. Nadia, thank you for reminding us of the importance of binarity, and for being such a good listening ear in times of pressing deadlines. Christian, your unique combination of levity and dedication made the group a better place. Anna, thank you for showing the power of hard work and really good planning. John, I hope we will get to keep working on that embedded-to-class-II disk evolution. Thank you also to Catherine, for your deep knowledge and for getting us out of Florence. Benoît – your colorful multi-panel plots at group meetings will be missed. My friends in the lab – Danna, Niels, Michał, Ko-Ju, Vincent, and Jeroen: thank you for forcing me to look beyond the bubble of observational astronomy, as well as for being fun colleagues and officemates in general.

Beyond this there are of course all those other members of the Sterrewacht who have made it a wonderful place to work on science, current and former, students and staff. Vincent, Butler: this all started with those meetings back in the early 2000s. Ignas, your supervision of all those different projects always kept me wanting to come back and do more. Being a TA for the Stars course, first under Huub and then Ignas, was a wonderful way to learn more, and watching a student understand something for the first time was always a great experience. Arthur, Jorryt, and Dilovan: thank you for making the moments in between more fun.

Leiden is bigger than the Sterrewacht, and so I would also like to thank all of the many other people I met there and who enriched my life there. My friends at Sempre, C-Dur, and in the Thunderbyrds: there are too many good memories here to even begin to summarize. From the Concertgebouw to het Paard, from Peter and the Wolf in the Stadsgehoorzaal to the Canary cantata in the Marekerk, in The Hague at Floris' and Mara's house, or just in the Salon at some ungodly hour: your musicality and friendship have been a great source of joy and comfort.

Likewise, all of the past and present inhabitants of the Klikspaanweg 16 who made it a good place to live for all those years, and never dull. From fancy or failed dinners together to shared massive cleaning efforts to catsitting, to your infinite patience when I was practising the Bird solo – it was a good time. I will miss being able to walk into the living room for five minutes in between writing.

Another fixture of my time in Leiden were the Thursday evening dinners on the Brahmslaan. Opa en Oma, ik heb het elke keer ongelofelijk fijn gevonden om even uit te kunnen blazen en bij jullie te zijn, af en toe ergens over in discussie te gaan, of de Trouw-kruiswoordpuzzel op te lossen. Kom snel op bezoek!

Lastly, to my parents, to Heleen, and to Friso: for your encouragement, your interest, your presence, comfort, and love, I cannot possibly thank you enough.